The Dissertation Committee for Jessica Delaney Meixner
certifies that this is the approved version of the following dissertation:

Discontinuous Galerkin Methods for Spectral Wave/Circulation Modeling

Committee:

Clint Dawson, Supervisor

Irene Gamba

Björn Engquist

Leszek Demkowicz

Ben Hodges

Joannes Westerink

Discontinuous Galerkin Methods for Spectral Wave/Circulation Modeling

by

Jessica Delaney Meixner, B.S., M.S.C.A.M.

DISSERTATION

Presented to the Faculty of the Graduate School of

The University of Texas at Austin

in Partial Fulfillment

of the Requirements

for the Degree of

DOCTOR OF PHILOSOPHY

THE UNIVERSITY OF TEXAS AT AUSTIN

August 2013

To my parents.

Acknowledgments

I am a firm believer of the saying "it takes a village." On that note, I would like to thank the many people who have helped me along the way. This dissertation would not be possible without their help.

I would first and foremost like to thank my adviser Clint Dawson. From the very first day I arrived at the University of Texas, he has provided me guidance and reassurance. My graduate program would not have been possible if not for his support, knowledge, encouragement and mentorship throughout my graduate studies.

I would like to thank the Computational and Applied Mathematics Fellowship, the Institute for Computational Engineering and Sciences and the University of Texas at Austin for providing wonderful opportunities and an environment to learn about interdisciplinary research.

I would also like to thank my committee members, Irene Gamba, Björn Engquist, Leszek Demkowicz, Ben Hodges, and Joannes Westerink, for their time, input and participation.

I would also like to acknowledge and thank the Computational Hydraulics Group for their friendship and camaraderie throughout these past years. I would especially like to acknowledge Casey Dietrich, whose contributions and collaborations over the past three years has helped immeasurably.

I would like to thank all of my friends who have made my time in Austin wonderful. Lastly, I would like to thank all of my family: my siblings, brother-in-law and sister-in-law for always being an amazing support system, my father for giving me a love of science and my mother, who always taught me/showed me anything was possible.

Discontinuous Galerkin Methods for Spectral Wave/Circulation Modeling

Jessica Delaney Meixner, Ph.D.
The University of Texas at Austin, 2013

Supervisor: Clint Dawson

Waves and circulation processes interact in daily wind and tide driven flows as well as in more extreme events such as hurricanes. Currents and water levels affect wave propagation and the location of wave-breaking zones, while wave forces induce setup and currents. Despite this interaction, waves and circulation processes are modeled separately using different approaches. Circulation processes are represented by the shallow water equations, which conserve mass and momentum. This approach for wind-generated waves is impractical for large geographic scales due to the fine resolution that would be required. Therefore, wind-waves are instead represented in a spectral sense, governed by the action balance equation, which propagates action density through both geographic and spectral space. Even though wind-waves and circulation are modeled separately, it is important to account for their interactions by coupling their respective models.

In this dissertation we use discontinuous-Galerkin (DG) methods to couple spectral wave and circulation models to model wave-current interactions. We first develop, implement, verify and validate a DG spectral wave model, which allows for the implementation of unstructured meshes in geographic space and the utility of adaptive, higher-order approximations in both geographic and spectral space. We then couple the DG spectral wave model to an existing DG circulation model, which is run on the same geographic mesh and allows for higher order information to be passed between the two models. We verify and validate coupled wave/circulation model as well as analyzing the error of the coupled wave/circulation model.

Table of Contents

List of Tables

List of Figures

Chapter 1

Introduction

1.1 Background and Motivation

Waves, periodic motions of the ocean surface, are a vital part of the dynamics of many coastal applications, in particular the forecasting and hindcasting of hurricanes. Hurricane waves and storm surge can cause extensive property damage and loss of life. Forecasting hurricane waves and surge via computational models can aid in emergency planning and evacuations of coastal regions, and hindcasting hurricanes helps with assessing risk and developing mitigation strategies.

Approaches to computational modeling of waves differ based on the wave period, which can vary from fractions of seconds to months. Long waves, including tides, sieches, tsunamis, and surges, have periods that range from minutes to months, while wind-generated waves are shorter waves and have periods that range from 0.5-25 s. In addition to having well-defined, separate ranges of periods, long and short waves are well-separated in the energy spectrum. Therefore, long and short waves are modeled using distinct methods and approaches. Computational models of long waves employ conservation laws of mass and momentum to describe circulation processes such as tsunamis,

storm surge, and tides. This approach is called phase-resolving and is impractical to implement for short waves on basin wide scales, which are of interest in many coastal applications; and therefore, phase-averaging or spectral approaches are employed. The spectral approach describes waves in a statistical sense via the action density spectrum and conserves the action density via the action balance equation to model wind-generated waves and swell.

Despite the fact that circulation and wind-waves are well-separated in the energy spectrum and are modeled separately using the distinct approaches for long and short waves, wind-waves and circulation can interact. Currents and water levels affect wave propagation and the location of wave-breaking zones, while wave forces induce setup and currents. Fukashimo (2008) and Dietrich *et al.* (2010) showed that coupling wave and circulation in hindcasts of hurricanes increases water levels by 5%-20% in regions of broad shelf and up to 35% in regions of steep slope [37, 52], which reiterates the need for coupling wave/circulation for hurricane hindcasting.

There are many spectral wave models that utilize different numerical techniques. Spectral wave models are governed by the action balance equation, which describes waves in a statistical, phase-averaging sense. These models account for propagation of waves in both deep and shallow water, frequency shifting due to changes in depth and current, and depth- and current-induced refraction. Through source terms, these models also account for generation of waves via wind; dissipation of waves via white-capping, bottom friction, and wave-breaking; and non-linear wave-wave interactions. Well-known

wave models such as Simulating WAves Nearshore (SWAN) [11], WAve Model (WAM) [132] and WAVEWATCH [127] each employ different finite-difference schemes in both geographic and spectral space. In coastal applications, it is of interest to model waves generated in the deep ocean as they propagate and transform in the near-shore coastal regions due to changes in bathymetry and bottom friction. To resolve these spatial scales, previous models employed nested structured meshes to enhance resolution in desired regions. To circumvent nested meshes while still capturing the required resolution of spatial scales, SWAN has been extended to utilize unstructured meshes within their existing finite-difference framework [140]. Other new models employing unstructured meshes either use finite volume methods in geographic space [111] or the finite element method in geographic space [65] while still using finite difference methods in spectral space. Another model implements discontinuous Galerkin methods with unstructured meshes in geographic space and a Fourier collocation method in spectral space [139].

In contrast, we are implementing a discontinuous Galerkin method for the action balance equation in both geographic and spectral space. This allows the implementation of unstructured meshes in geographic space as well as the utility of adaptive, higher-order approximations in both geographic and spectral space. By employing adaptivity, particularly in spectral space, we will maintain the high-accuracy of the computed solution while decreasing some of the extra degrees of freedom necessary when using discontinuous Galerkin methods.

The discontinuous Galerkin spectral wave model has been coupled with the Discontinuous Galerkin Shallow Water Equation Model (DG-SWEM) [78]. This model uses the shallow water equations discretized by discontinuous Galerkin methods to model circulation processes including tides and storm surge. The continuous Galerkin ADCIRC model has previously been coupled loosely [37] and tightly [41] with spectral wave models to hindcast hurricane waves and surge. A main goal of this dissertation is to use discontinuous-Galerkin methods to couple spectral wave and circulation models to model wave-current interactions. This required the development, implementation, verification and validation of the discontinuous-Galerkin spectral wave model; coupling the discontinuous-Galerkin spectral wave model to DG-SWEM; and validating the coupled model, as well as analyzing the error of the coupled model.

1.2 Literature Review

In this section we provide historical and literature reviews of shallow water models, spectral wave models, coupled wave/circulation models and discontinuous Galerkin methods.

1.2.1 Shallow Water Models

The development of shallow water models can be traced back for centuries through the study of tides. For a complete history of the study of tides see for example [16]; here we only mention the major milestones in the

development of shallow water models. Some of the first theories, although scientifically incorrect, were made in the Copernican Revolution by Galieo, Kepler and Descartes [16]. In 1687 as a consequence of Newton's gravitational theory (between the Earth, Moon, and Sun), the first scientifically valid theories for tides were proposed and Bernoulli's equilibrium theory of tides became conventional theory [16]. A major advancement for shallow water equations was by Laplace in 1775 for his dynamic theory of tides [80] and is known as Laplace's tidal equations, which can be seen as a specialized form of the shallow water equations [131]. Other important advancements in shallow water models include several major advancements in fluid mechanics. In 1755, Euler derived basic laws of fluid motion which are now known as Euler's Equations [49]. Further contributions by Navier (1823) in [101] and Stokes (1845) in [123] led to what we now know as the Navier-Stokes equations for viscous flow. A contribution by Reynolds (1883) lead to the Reynolds-Averaged Navier-Stokes Equations [113]. In 1871, Boussinesq and Saint-Venant independently discovered the connection between the Navier-Stokes and Shallow Water Equations (SWE) [96].

Analytic solutions to the SWE are not known for generalized cases, however numerical solutions to the SWE became possible in the 1940s with the advent of electronic computers. Early numerical work includes atmospheric simulations by Charney *et al.* in 1950 [19] and a coastal sea model by Hansen in 1956 [56]. These early methods, mostly finite difference, were prone to spurious spatial oscillations. By the late 1950s, it was noticed that

the early numerical models (which were typically finite difference methods) were prone to spurious oscillations [96]. Some strategies used to control or suppress oscillations included staggered grids, which were introduced in [56] and also used in [110] and [82], a mixed interpolation [125], viscous coefficients [133], nonphysically large bottom friction [106], and the most common method which is a reformulation of the SWE as a single wave equation known as the generalized wave continuity equation (GWCE) [73, 90]. None of these methods completely solved the oscillation issue, however the reformulation of the SWE to the GWCE was the most successful [1]. In the 1980s finite element methods for solving SWE emerged including FEUDX [102], which utilized the non-conservative form of the primitive SWE and FE2DY [122]. GWCE-based models were developed by Kinnmark and Gray (1984) using an implicit solution procedure [72] and by Luettich and Westerink (1992) who developed the ADvanced CIRCulation model ADCIRC [89]. Recently, DG methods have become popular for SWE (e.g. [2, 32, 51, 76, 78, 83, 118]). Continuous-Galerkin (CG) finite-element methods such as those employed by ADCIRC are limited to linear approximations, have difficulties handling strong advection and are not locally mass conservative [32]. Recent efforts within the ADCIRC development team have focused on the use of DG methods; this DG Shallow Water Equation Model (DG-SWEM) can employ higher-order approximations and can handle advection-dominated flows [78]. In addition, DG models are locally and globally conservative, which can be important when coupling to transport equations [31, 36].

1.2.2 Spectral Wave Models

The literature review presented here is intended to be brief; for a more complete historical review see [68] or [132]. An interesting historical fact is that the operational models for forecasting waves were developed in preparation for the D-Day invasion of Normandy in World War II [130]. Early wave models only considered a single representative wave described by its wave height and period [130]. Since the work of Gelci *et al.* (1957), numerical wave models transport the two-dimensional wave spectrum [53]. The source term structure involves the input of wind S_{in} due to Phillips (1957) [107] and Miles (1957) [95], the nonlinear transfer S_{nl} due to wave-wave interactions, and a dissipation term S_{ds} due to whitecapping and turbulence (Hasselmann 1960, [57]). Wave models are characterized as first, second or third generation models based on their source term formulations.

First-generation models were developed in the 1960s and early 1970s. From the beginning, there was skepticism over the validity of the first-generation formulations' ability to model the waves and it has since been shown that these models were off by an order of magnitude for modeling wind input and nonlinear transfer [68, 132]. Mitsuyasu in 1968 [98] and 1969 [99], Hasselmann *et al.* in 1973 [60], and Snyder *et al.* in 1981 [119] made measurements of wave growth. After these measurements, second-generation models emerged which were characterized by prescribed parametric shapes of the spectrum [68, 132]. A major shortcoming of second-generation models were their inability to properly model waves in the presence of strong, rapidly changing winds like that

of hurricanes. SWAMP (1985) investigated and reported the short-comings of first- and second-generation wave models and suggested the development of third-generation wave models [124].

The first third-generation model, the WAve Model (WAM) [132] was developed by the WAMDI-Wave Model Development and Implementation Group in 1988. This model used the discrete interaction approximation of Hasselman *et al.* (1985) for the nonlinear wave interactions [61]. The wind input and source functions were formulated by Komen *et al.* (1984) to close the energy balance and replicate the observed measurements [74].

Since the development of WAM (1988), several other well-established wave models emerged including WAVEWATCH (1991) by Tolman [127] and SWAN (1999) by Booij *et. al* [11]. All three models employ first- or second-order finite difference schemes. To model waves propagating from the deep ocean to shallow waters, a mesh with multiple scales is required. Nesting of structured meshes is a classical solution to resolve multiple spatial scales, however unstructured meshes provide more flexibility and often a more attractive solution. The semi-Lagrangian model TOMAWAC (1996) by Benoît *et al.* is likely the first spectral wave model to employ unstructured triangular meshes. Sørensen *et al.* (2004) developed MIKE21 SW using an unstructured cell-centered finite volume method in both geographic and spectral space [120]. Roland *et al.* in the Wind Wave Model (WWM) in 2006 also employed finite element methods in geographic space [117]. Several others modified the SWAN framework to use unstructured meshes via other numerical methods. Hsu *et*

al. (2005) modified SWAN to utilize finite element methods in geographic space [65] . Qi *et al.* (2009) implemented finite volume methods in geographic space within the SWAN framework to create the FVCOM-SWAVE model [111]. In 2009, Zijlema updated SWAN to employ unstructured meshes via a modified finite difference scheme [140]. Yildirim and Karniadakis (2012) employ discontinuous Galerkin methods on an unstructured mesh in geographic space and a Fourier-collocation method in spectral space [139]. The collocation method requires the modification of the action balance equation to facilitate absorbing boundary conditions for frequency and requires periodicity at the frequency boundaries for fast convergence of the Fourier-collocation. We employ discontinuous Galerkin methods in both geographic and spectral space, which allows for the utilization of unstructured meshes in geographic space as well as adaptive, higher-order approximations in both geographic and spectral space.

1.2.3 Coupled Wave/Circulation Models

In this section we provide a brief overview of relevant works studying the interactions of waves and circulation. We begin with theoretical works and conclude with the more recent works of coupling numerical waves and circulation models.

Longuet-Higgins and Stewart introduced the concept of radiation stress, "the excess flow of momentum due to the presence of the waves" and examined the role of radiation stress in, for example, the change in mean sea level or mean flow, the interactions of waves with steady currents and the generation of

wave-beats [85–88]. Wave/circulation interaction continues to be a subject of research; for example, Dalrymple and Lozano (1978) studied rip currents [30], Dolata and Rosenthal (1984) studied wave-induced currents and setup [42], and McWilliams and Restrepo (1999, 2004) developed a wave-averaged asymptotic model for the interaction of waves and currents in coastal regions [92, 93].

Several different strategies have been used for coupling numerical wave and circulation models. The numerical wave and circulation models have been developed separately, and the strategies for coupling the models often depend on the numerical techniques and meshes used for the individual models. For instance, to deal with the multiple scales that are present in many applications, structured meshes can be nested to refine a mesh in desired areas. Kim *et al.* (2008) coupled wave and circulation models to hindcast Typhoon Ewiniar on the same nested structured meshes [71]. When unstructured meshes for circulation models (eg. [136]) emerged as an alternative solution to structured nested meshes to provide varying scales of resolution, coupled models employed heterogeneous meshes. A single unstructured mesh was employed for the circulation model and one or several structured meshes were utilized for the wave model. To couple the models, information must be interpolated between the heterogeneous meshes and passed between the two models, often via external files. This coupling has been employed by many including Weaver and Slinn [135], Funakoshi *et al.* [52], Chen *et al.* [20], and Pandoe and Edge *et al.* [105], and by Bunya *et al.* [14] and Dietrich *et al.* [37]. The main disadvantage of this coupling is the required interpolation, especially in a parallel

computing environment where the interpolation requires costly global communication. As unstructured meshes became prevalent in wave models as well, coupling wind/circulation models between two homogeneous meshes without interpolation was possible. These couplings share the same geographic mesh, and therefore, in a parallel computing environment, these couplings do not require global communication as intra-model communication is done through local cache on the same sub-mesh. An example of this type of coupling is the ADCIRC+SWAN model [41].

Generic frameworks are a well-known tool for coupling models. These frameworks manage the intricacies of when and how the models are run and the interpolation between models if necessary. These general frameworks include the Earth System Modeling Framework(ESMF) [29, 63], Open Modeling Interface (OpenMI) Environment [54, 100] the Modeling Coupling Toolkit (MCT) [134]. Although these frameworks ease the implementation of the wave/circulation coupling and allow for future coupling to other models, they do not eliminate the problems with interpolation error if heterogeneous meshes are used.

1.2.4 Discontinuous Galerkin Methods

We provide a brief literature review of the development of discontinuous Galerkin (DG) methods. DG methods were developed in two parallel paths: the DG methods for hyperbolic equations, and interior penalty (IP) methods for elliptic and parabolic equations [5]. A complete, detailed historical review

can be found in [5], where Arnold, Brezzi, Cockburn and Marini discuss a unified analysis of DG methods or [23] where Cockburn, Karniadakis and Shu discuss the developement of DG methods.

Some of the first developments were in 1968 when Lions enforced Dirichlet boundary conditions through penalties when solving elliptic problems [84]. In 1970 Aubin implemented this approach for finite difference approximations of nonlinear problems [6]. Babuška (1973) applied this method for finite element methods and discovered that the order of convergence was suboptimal as a consequence of the inconsistent weak formulation [7]. Nitsche (1971) employed a different approach that applied a penalty parameter but was consistent and had optimal H^1 and L^2 convergence rates [103].

From the idea that Dirichlet boundary conditions could be imposed weakly instead of being built into the finite element space arose the idea of interior penalty (IP) methods, where interelement continuity could be imposed in a similar manner [5]. Babuška and Zlàmal (1973) utilized IP methods to weakly impose C^1 continuity for fourth-order problems [8]. Wheeler (1978) formulated an IP collocation-finite element method [137] based on the procedures of Douglas and Dupont [43], which was a generalization of Nitsche's method to second-order elliptic problems [5]. The generalization of Nitsche's method was analyzed for linear and nonlinear elliptic and parabolic problems [4]. From the early 1980's to the 1990's, interest in IP methods has waned possibly due to the facts that IP method has no proven advantage over the classical FEM and the difficulty in finding optimal penalty parameters [5].

Simultaneously, DG methods for the numerical treatment of nonlinear hyperbolic equations have been developed for the past twenty years. Reed and Hill (1973) developed a finite element method for the neutron transport problem [112], which is the first DG method [5]. Lasaint and Raviart (1974) analyzed this method [81] and gave rise to the name "discontinuous Galerkin" method [96]. Wellford and Oden (1975) used a discontinuous Galerkin finite element method to analyze shock waves in nonlinear elastic materials. They decompose the domain into shock-less regions, where they employ traditional finite element methods, and use discontinuous formulations for the elements with the shock [70]. Cockburn and Shu introduced and analyzed the Runge-Kutta DG methods in a series of papers [22, 24–26, 28]. In 1998, Cockburn and Shu introduced and analyzed the local discontinuous Galerkin (LDG) method for convection-diffusion problems [27]. Cockburn and Dawson (1999) generalized these results to multi-dimensional equations with spatially varying coefficients [21] and Castillo (2002) *et. al.* analyzed the *hp* version [17].

1.3 Summary of Contributions

In this dissertation, we have presented, analyzed and implemented a discontinuous Galerkin coupled wave/circulation model. In particular, we have achieved the following:

- We have developed and implemented a DG spectral wave model (see Chapter 2). This model employs general triangular meshes in geographic space and structured quadrilateral meshes in spectral space. The model

can utilize higher order approximations in both geographic and spectral space. The model is scalable and can utilize adaptivity for increased computational efficiency (see Section 4.4).

- We have verified and validated the DG spectral wave model through the method of manufactured solutions and analytic test cases as well as comparing to SWAN (see Chapter 4).

- The DG spectral wave model has been coupled to DG-SWEM and the resulting coupled wave/circulation model has been verified and validated through comparisons to SWAN coupled with DG-SWEM (see Chapter 5).

- An *a priori* error estimate has been performed for the discontinuous Galerkin couple wave/circulation model. The estimate is performed for the simplified one-dimensional geographic space model; however, all arguments are valid in the full two-dimensions. Although this DG formulation of the shallow water equations had been analyzed in [35], no coupled wave/circulation model had previously been analyzed for any numerical scheme (see Chapter 6).

1.4 Outline

The remainder of this dissertation is laid out as follows. Chapter 2 introduces the concept of spectral modeling along with the governing action balance equation and source term formulations. Chapter 3 explains the DG

method, which is utilized to discretize the action balance equation. Implementation details such as the choice of basis functions, quadrature rules, and fluxes are also included. Chapter 4 is comprised of numerical results of the DG spectral wave model. We verify and validate the DG spectral wave model through the method of manufactured solutions, comparisons to academic test cases, and comparisons to the well-known SWAN model. Chapter 5 introduces the DG circulation model DG-SWEM, couples the DG wave model to DG-SWEM, and presents numerical results to validate the coupled wave/circulation model. Chapter 6 analyzes the error of the coupled wave/circulation model. Chapter 7 provides concluding remarks.

Chapter 2

Spectral Wave Model

2.1 Spectral Description of Waves

In this chapter, we provide an explanation of the spectral description of waves, present the governing action balance equation, and provide expressions for the source term formulations. The following description is an abbreviated version of [64]. Because it is impractical in numerical modeling to resolve the phases of individual waves, we employ a spectral approach by looking at average wave characteristics using the Random Phase/Amplitude Model. In this model, we represent the surface elevation η as the sum of a large number of harmonic waves

$$\underline{\eta}(t) = \sum_{i=1}^{N} \underline{a}_i \cos(2\pi f_i t + \underline{\alpha}_i),$$

with frequencies f_i and where each harmonic wave has a randomly chosen, constant amplitude $\underline{a}_i$ and phase $\underline{\alpha}_i$ in which the underscore indicates that these are random variables. We can define the variance density spectrum $E(f)$ as

$$\text{total variance} = \overline{\underline{\eta}^2} = \int_0^\infty E(f)df,$$

where f is frequency, provided that the surface elevation can be seen as a stationary, Gaussian process. Although it is not always true, generally we may

represent the surface elevation as a stationary Gaussian process. The variance density spectrum gives us a complete description, in the statistical sense, of the surface elevation of ocean waves. For instance, a variance density function that is a delta function represents a harmonic wave, while a variance density function with a wide spectrum represents an irregular wave. By multiplying the variance density by the density of water ρ and gravitational acceleration g, we obtain the energy density spectrum

$$E_{energy}(f) = \rho g E_{variance}(f).$$

To account for waves propagating in (x, y) geographic space in direction θ, relative to the positive x-axis, we expand the Random-Phase/Amplitude Model, so that the surface elevation is seen as the sum of a large number of propagating harmonic waves

$$\underline{\eta}(t) = \sum_{i=1}^{N} \sum_{j=1}^{M} \underline{a}_{i,j} \cos(2\pi f_i t - k_i x \cos\theta_j - k_i y \sin\theta_j + \underline{\alpha}_{i,j}),$$

where k is the wave number. We then obtain the two-dimensional variance density spectrum $E(f, \theta)$, which can be reduced to the one-dimensional frequency spectrum by integrating over all directions θ.

As previously mentioned, the variance density provides a statistical description of waves. These characteristics are defined in terms of the moments of the variance density spectrum,

$$m_n = \int_0^\infty f^n E(f) df \quad \text{for } n = \ldots, -3, -2, -1, 0, 1, 2, 3, \ldots.$$

From these moments, we can determine the mean wave height

$$\overline{H} = \sqrt{2\pi m_0},$$

the significant wave height

$$H_{m_0} \approx 4\sqrt{m_0},$$

which is a quantity related to the average value of the highest one-third waves in a series, and the mean zero-crossing period

$$\overline{T}_0 = T_{m_{02}} = \sqrt{\frac{m_o}{m_2}}.$$

To model waves, we assume the Random-Phase/Amplitude Model and predict how each independent wave component with spectral density $E = E(f, \theta)$ varies in time and space. If a current is present, the energy density spectrum is not conserved, and therefore, waves are described by the action density spectrum $N = E/\sigma$, where σ is the relative frequency [87].

2.2 Action Balance Equation

The action density $N(\sigma, \theta; x, y, t)$ is governed by the action balance equation

$$\frac{\partial}{\partial t} N + \nabla \cdot \mathbf{c} N = \frac{S}{\sigma}. \tag{2.1}$$

where $\nabla = (\frac{\partial}{\partial x}, \frac{\partial}{\partial y}, \frac{\partial}{\partial \sigma}, \frac{\partial}{\partial \theta})$ and $\mathbf{c} = (c_x, c_y, c_\sigma, c_\theta)$ are the propagation velocities. This equation represents the rate of change of action density in time t, propagation of action density through geographic space (x, y) with propagation velocities c_x and c_y, and spectral space (σ, θ) where σ is the relative frequency

(the frequency observed in a frame of reference moving with the current) and θ is the wave direction. The propagation through spectral space represents frequency shifting due to changes in depth and current with propagation velocity c_σ and depth-induced and current induced refraction with propagation velocity c_θ. The source term S represents the effects of generation by wind, dissipation and nonlinear wave interactions and is described in more detail in Section 2.3.

The propagation velocities in geographic space are defined as

$$c_x = c_{g,x} + u, \tag{2.2}$$

$$c_y = c_{g,y} + v, \tag{2.3}$$

where $\mathbf{U} = (u, v)$ is the velocity of the current, $\mathbf{c_g} = n\mathbf{c}_{ph} = (c_{g,x}, c_{g,y}) = (c_g \cos(\theta), c_g \sin(\theta))$ is the group velocity, $\mathbf{c}_{ph} = \frac{\sigma \mathbf{k}}{k^2}$ is the phase speed, $n = \frac{1}{2}\left(1 + \frac{2kH}{\sinh(2kH)}\right)$, H is the total water depth, and $\mathbf{k} = (k\cos(\theta), k\sin(\theta))$ is the wave number. The wave number is related to the frequency by the dispersion relationship

$$\sigma^2 = gk \tanh(kH),$$

where g is gravitational acceleration. The propagation velocities in spectral space are defined as

$$c_\sigma = \frac{\partial \sigma}{\partial H}\left(\frac{\partial H}{\partial t} + \mathbf{U} \cdot \nabla_{\mathbf{x}} H\right) - c_g \mathbf{k} \cdot \frac{\partial \mathbf{U}}{\partial s}, \tag{2.4}$$

$$c_\theta = -\frac{1}{k}\left(\frac{\partial \sigma}{\partial H}\frac{\partial H}{\partial m} + \mathbf{k} \cdot \frac{\partial \mathbf{U}}{\partial m}\right), \tag{2.5}$$

where $\mathbf{U} = (u, v)$ is the velocity of the current and (s,m) are spatial coordinates with s being normal to the wave direction θ and m being perpendicular to the wave direction θ [64, 126]. From the dispersion relationship we get that

$$\frac{\partial \sigma}{\partial H} = \frac{k\sigma}{\sinh(2kH)},$$

and the derivatives in s and m are expressed in derivatives in x and y by the chain rule. Therefore we can rewrite the propagation velocities in spectral space as follows

$$\begin{aligned} c_\sigma &= \frac{k\sigma}{\sinh(2kH)}\left(\frac{\partial H}{\partial t} + u\frac{\partial H}{\partial x} + v\frac{\partial H}{\partial y}\right) \\ &\quad -c_g k\left(\frac{\partial u}{\partial x}\cos^2\theta + \frac{\partial u}{\partial y}\cos\theta\sin\theta + \frac{\partial v}{\partial x}\sin\theta\cos\theta + \frac{\partial v}{\partial y}\sin^2\theta\right), \\ c_\theta &= \frac{\sigma}{\sinh(2kH)}\left(\frac{\partial H}{\partial x}\sin\theta - \frac{\partial H}{\partial y}\cos\theta\right) \\ &\quad +\frac{\partial u}{\partial x}\cos\theta\sin\theta - \frac{\partial u}{\partial y}\cos^2\theta + \frac{\partial v}{\partial x}\sin^2\theta - \frac{\partial v}{\partial y}\cos\theta\sin\theta. \end{aligned}$$

2.3 Source Terms

The general source term formulation for spectral wave models include a wind input term S_{in}, a dissipation term S_{ds} and a nonlinear transfer term S_{nl} due to wave-wave interactions. As knowledge and understanding of these processes grew, the source term functions evolved to third-generation formulations, which are considered to be state of the art. These formulations include an updated wind-input term, dissipation terms accounting for whitecapping, bottom friction, and depth-induced wave breaking, and formulations for nonlinear wave-wave interactions including both quadruplets and triads which are

only relevant in shallow water. We implement the third-generation formulations employed in SWAN [11]. The exact formulations for these source terms follows.

2.3.1 Wind Input

The wind input source term formulation is due to the theory of Miles and Phillip and has the general form

$$S_{in}(\sigma, \theta) = A + B * E(\sigma, \theta). \tag{2.6}$$

The linear portion A is due to Phillips (1957), who postulated that waves are generated by resonance between propagating wind-induced pressure waves and propagating water waves [107]. This term is only used when there are no initial waves and waves must be generated. When initial waves are present, Miles (1957) finds that waves modify the airflow and therefore the wind-induced pressure at the water surface [95]. The waves and wind-induced pressure create a positive-feedback system in which waves then enhance their own growth [64]. This positive-feedback system is formulated as $B * E$ in the wind input formulation.

The third generation formula employed in SWAN is the WAM Cycle 3 ([74, 132]) formulation. These formulations need the input parameter of the wind speed. Typical wind-input information is the wind speed at 10 m above the sea surface which must be converted to the friction velocity U_*, which is

$$U_*^2 = C_D U_{10}^2$$

where C_D is the drag coefficient from Wu [138]:

$$C_D(U_{10}) = \begin{cases} 1.2875 \times 10^{-3}, & \text{for } U_{10} < 7.5m/s \\ (0.8 + 0.065s/m * U_{10}) \times 10^{-3}, & \text{for } U_{10} \geq 7.5m/s \end{cases}$$

The linear growth term by Cavaleri and Malanotte-Rizzoli (1981) is implemented with a filter suggested by Tolman (1992) to cut off growth at frequencies lower than the Pierson-Moskowitz frequency [18, 128]. The linear term is

$$A = \frac{1.5 \times 10^{-3}}{2\pi g^2}(U_* \max[0, cos(\theta - \theta_w)]^4 H,$$
$$H = \exp\{-\left(\frac{\sigma}{\sigma^*_{PM}}\right)\},$$
$$\sigma^*_{PM} = \frac{0.13g}{28U_*}2\pi,$$

where θ_w is the wind direction, H is the filter and σ^*_{PM} is the peak frequency of the Pierson and Moskowitz (1964) fully developed sea state formulated in terms of friction velocity [109].

The exponential wave growth expression is due to Komen *et al.* (1984):

$$B = \max[0, 0.25\frac{\rho_a}{\rho_w}(28\frac{U_*}{c_{ph}}\cos(\theta - \theta_w) - 1]\sigma$$

in which ρ_a and ρ_w are the density of air and water and c_{ph} is the phase speed [74].

2.3.2 Dissipation

The dissipation source term is formulated in three parts representing the dissipative processes of whitecapping, bottom friction and wave breaking.

$$S_{ds} = S_{ds,wc} + S_{ds,bf} + S_{ds,br}$$

2.3.2.1 Whitecapping

Whitecapping is a complicated phenomenon, which is not fully understood theoretically, however, it is reasonable to assume that it is dependent on wave-steepness. The SWAN model employs the Komen *et al.* [74] formulation. This whitecapping formulation is based on the theory of Hasselmann (1974), in which white-caps are treated as a pressure pulse on the sea surface [59].

The WAMDI group (1988) reformulated Hasselmann's whitecapping source formulation, S_{wc}, in terms of the wave number as to account for whitecapping in shallow water as

$$S_{ds,wc}(\sigma,\theta) = -\Gamma\tilde{\sigma}\frac{k}{\tilde{k}}E(\sigma,\theta),$$

where $\tilde{\sigma}$ is the mean frequency, $\tilde{k}$ is the mean wave number and the coefficient Γ depends on the overall wave steepness. Günther *et al.* (1992) [55] adapt the WAMDI group (1988) formulation of the steepness dependent coefficient [132], based on work of Janssen (1991) [67],

$$\Gamma = \Gamma_{KJ} = C_{ds}\left((1-\delta)+\delta\frac{k}{\tilde{k}}\right)\left(\frac{\tilde{s}}{\tilde{s}_{PM}}\right)^{p},$$

where the coefficients C_{ds}, δ and p are tunable, $\tilde{k}$ is the mean wave number, $\tilde{s}$ is the overall wave steepness, and $\tilde{s}_{PM} = \sqrt{3.02\times10^{-3}}$ is the value of $\tilde{s}$ for the Pierson-Moskowitz spectrum [109]. The overall wave steepness $\tilde{s}$, the mean frequency $\tilde{\sigma}$, the mean wave number $\tilde{k}$ and the total energy E_{tot} are defined as is

$$\tilde{s} = \tilde{k}\sqrt{E_{tot}},$$

$$\tilde{\sigma} = \left(E_{tot}^{-1} \int_0^{2\pi} \int_0^{\infty} \frac{1}{\sigma} E(\sigma, \theta) d\sigma d\theta \right)^{-1},$$
$$\tilde{k} = \left(E_{tot}^{-1} \int_0^{2\pi} \int_0^{\infty} \frac{1}{\sqrt{k}} E(\sigma, \theta) d\sigma d\theta \right)^{-2},$$
$$E_{tot} = \int_0^{2\pi} \int_0^{\infty} E(\sigma, \theta) d\sigma d\theta.$$

The tunable coefficients and exponent p are chosen to correspond to the Komen *et al.* (1984) formulation [74]:

$$C_{ds} = 2.36 \times 10^{-5},$$
$$\delta = 0,$$
$$p = 4.$$

2.3.2.2 Bottom Friction

As waves move into shallow water, an interaction occurs between the orbital motion of the water particles and the turbulent boundary layer. The dissipation that occurs depends on the wave field as well as the bottom characteristics. Here bottom friction is modeled by the empirical model of the JOint North Sea WAve Project (JONSWAP) [60]. Formulation for the bottom friction is expressed as:

$$S_{ds,bf} = -C_b \frac{\sigma^2}{g^2 \sinh^2 kH} E(\sigma, \theta),$$

where C_b is a bottom friction coefficient that generally depends on the bottom orbital motion represented by U_{rms}:

$$U_{rms}^2 = \int_0^{2\pi} \int_0^{\infty} \frac{\sigma^2}{\sinh^2 kH} E(\sigma, \theta) d\sigma d\theta.$$

There are several values for the bottom friction coefficient. To agree with the JONSWAP result for swell dissipation, Hasselmann *et al.* (1973) found $C_b = C_{JON} = 0.038 m^2 s^{-3}$ [60]. Bouws and Komen (1983) recommend a value of $C_{JON} = 0.067 m^2 s^{-3}$ after examining the energy balance on the North Sea in depth-limited conditions [12], which is the value we choose.

2.3.2.3 Depth-Induced Wave Breaking

Wave heights are limited in shallow water via the process of wave-breaking. Depth-induced wave breaking is modeled by Battjes and Janssen's (1978) bore-based model [9]. The mean rate of energy dissipation per unit horizontal area due to wave breaking is

$$D_{tot} = -\frac{1}{4} \alpha_{BJ} Q_b \left(\frac{\tilde{\sigma}}{2\pi} \right) H_{max}^2 = -\alpha_{BJ} Q_b \tilde{\sigma} \frac{H_{max}^2}{8\pi},$$

where the coefficient $\alpha_{BJ} = 1$ as it is in SWAN [126], Q_b is the fraction of breaking waves

$$\frac{1 - Q_b}{\ln Q_b} = -8 \frac{E_{tot}}{H_{max}^2},$$

in which $H_{\max}$ is the maximum wave height that can exist at the given depth, the mean frequency is $\tilde{\sigma} = E_{tot}^{-1} \int_0^{2\pi} \int_0^{\infty} \sigma E(\sigma, \theta) d\sigma d\theta$, and the total wave energy is $E_{tot} = \int_0^{2\pi} \int_0^{\infty} E(\sigma, \theta) d\sigma d\theta$. The fraction of depth-induced breakers Q_b

is determined by SWAN [126] as

$$Q_b = \begin{cases} 0, & \text{for } \beta \leq 0.2, \\ Q_0 - \beta^2 \frac{Q_0 - \exp(Q_0 - 1)/\beta^2}{\beta^2 - \exp(Q_0 - 1)/\beta^2}, & \text{for } 0.2 < \beta < 1, \\ 1, & \text{for } \beta \geq 1, \end{cases}$$

where $\beta = \frac{H_{rms}}{H_{max}}$ and $Q_0 = 0$ for $\beta \leq 0.5$ or $Q_0 = (2\beta - 1)^2$ for $0.5 < \beta \leq 1$.

The source term expression for dissipation due to breaking $S_{ds,br}$ is formulated in SWAN [126] by extending the expression of Eldeberky and Battjes (1996) to include the spectral directions [48]

$$S_{ds,br} = \frac{D_{tot}}{E_{tot}} E(\sigma, \theta) = -\frac{\alpha_{BJ} Q_b \tilde{\sigma}}{\beta^2 \pi} E(\sigma, \theta),$$

where the max wave height is calculated by $H_{max} = \gamma H$, in which $\gamma = 0.73$ is the breaker parameter and H is the total water depth.

2.3.3 Nonlinear Wave-Wave Interactions

Waves transfer energy to each other through resonance. These nonlinear wave-wave interactions occur in quadruplets (deep or shallow water) and in triads (only in shallow water). The nonlinear source term is comprised of the formulations for quadruplets and triads

$$S_{nl} = S_{nl4} + S_{nl3}.$$

2.3.3.1 Quadruplets

Energy is passed between four waves, if they meet the resonance condition:

$$f_1 + f_2 = f_3 + f_4,$$

$$\vec{k}_1 + \vec{k}_2 = \vec{k}_3 + \vec{k}_4,$$

where f_i and k_i are the frequency and waves numbers of wave i=1-4. This transfer of energy (referred to as quadruplet wave-wave interactions) can be represented by the expression given by Hasselmann:

$$\begin{aligned} &S_{nl4}(\vec{k}_4) \\ &\quad = \iiiint T_1(\vec{k}_1, \vec{k}_2, \vec{k}_1 + \vec{k}_2 - \vec{k}_4) E(\vec{k}_1) E(\vec{k}_2) E(\vec{k}_1 + \vec{k}_2 - \vec{k}_4) d\vec{k}_1 d\vec{k}_2 \\ &\quad - E(\vec{k}_4) \iiiint T_2(\vec{k}_1, \vec{k}_2, \vec{k}_4) E(\vec{k}_1) E(\vec{k}_2) d\vec{k}_1 d\vec{k}_2, \end{aligned}$$

where $\vec{k}_4$ is the wave number of the wave component considered in the source term, $\vec{k}_1$,$\vec{k}_2$, and $\vec{k}_3 = \vec{k}_1 + \vec{k}_2 - \vec{k}_4$ are the three other wave components involved subject to the resonance condition, and T_1 and T_2 are the transfer coefficients [58]. The exact computation of this integral is too costly for computational wave models, and therefore an approximation of the quadruplet wave-wave interaction is required. Like SWAN, we implement the Discrete Interaction Approximation (DIA) by Hasselmann to approximate the quadruplet nonlinear wave-wave interactions [61]. We implement the DIA approximation as SWAN does [126]. The DIA approximation considers two quadruplets with frequencies

$$\begin{aligned} \sigma_1 &= \sigma_2 = \sigma, \\ \sigma_3 &= \sigma(1 + \lambda) = \sigma^+, \\ \sigma_4 &= \sigma(1 - \lambda) = \sigma^-, \end{aligned}$$

where $\lambda = 0.25$. These quadruplets must satisfy the resonance conditions, so for the first quadruplets, the wave-number vectors with frequency σ_3 and σ_4 lie

at an angle of $\theta_3 = -11.48^\circ$ and $\theta_4 = 33.56^\circ$ to the angle of the wave number vectors with frequencies σ_1 and σ_2. For the second quadruplet, $\theta_3 = 11.48^\circ$ and $\theta_4 = -33.56^\circ$. The DIA source term for quadruplet nonlinear wave-wave interactions is

$$S_{nl4}(\sigma,\theta) = S^{*}_{nl4}(\sigma,\theta) + S^{**}_{nl4}(\sigma,\theta),$$

where $S^{*}_{nl4}(\sigma,\theta)$ refers to the first quadruplet and $S^{**}_{nl4}(\sigma,\theta)$ corresponds to the second quadruplet. The expression for the first quadruplet is

$$S^{*}_{nl4}(\sigma,\theta) = 2\delta S_{nl4}(\alpha_1\sigma,\theta) - \delta S_{nl4}(\alpha_2\sigma,\theta) - \delta S_{nl4}(\alpha_3\sigma,\theta),$$

where

$$\begin{aligned}\delta S_{nl4}(\alpha_i\sigma,\theta) =& C_{nl4}(2\pi)^2 g^{-4}\left(\frac{\sigma}{2\pi}\right)^{11} \\ & \left\{E^2(\alpha_i\sigma,\theta)\left[\frac{E(\alpha_i\sigma^{+},\theta)}{(1+\lambda)^4} + \frac{E(\alpha_i\sigma^{-},\theta)}{(1-\lambda)^4}\right]\right. \\ & \left. -2\frac{E(\alpha_i\sigma,\theta)E(\alpha_i\sigma^{+},\theta)E(\alpha_i\sigma^{,}\theta)}{(1-\lambda^2)^4}\right\}\end{aligned}$$

for $i = 1, 2, 3$, where $\alpha_1 = 1$, $\alpha_2 = (1+\lambda)$, $\alpha_3 = (1-\lambda)$ and $C_{nl4} = 3 \times 10^7$. The expressions for the second quadruplet $S^{**}_{nl4}(\sigma,\theta)$ are the same as for the first quadruplet $S^{*}_{nl4}(\sigma,\theta)$ except for the mirror directions.

The previous expressions are for water with infinite depth, and to obtain the expressions for finite depth, the infinite depth expression is multiplied by a scaling factor as suggested by the WAMDI group [132]

$$S^{\text{finite depth}}_{nl4} = R(k_p H) S^{\text{infinite depth}}_{nl4},$$

where

$$R(k_pH) = 1 + \frac{C_{sh1}}{k_pH}(1 - C_{sh2}k_pH)e^{C_{sh3}k_Hd},$$

in which k_p is the peak wave number with an imposed lower limit of 0.5 and the coefficients are chosen as follows: $C_{sh1} = 5.5$, $C_{sh2} = 5/6$, and $C_{sh3} = -5/4$.

2.3.3.2 Triads

Triad wave-wave interactions only occur in shallow water and are approximated using the Lumped Triad Approximation (LTA) of Eldeberky [46], which is a modified version of the Discrete Triad Approximation (DTA) of Eldeberky and Battjes [47]. In each spectral direction:

$$S_{nl3}(\sigma,\theta) = S^{-}_{nl3}(\sigma,\theta) + S^{+}_{nl3}(\sigma,\theta),$$

where

$$S^{+}_{nl3}(\sigma,\theta) = \max[0, \alpha_{EB}2\pi cc_gJ^2|\sin\beta|\{E^2(\sigma/2,\theta) - 2E(\sigma/2,\theta)E(\sigma,\theta)\}],$$

and

$$S^{-}_{nl3}(\sigma,\theta) = -2S^{+}_{nl3}(2\sigma,\theta),$$

where α_{EB} is a tunable proportionality coefficient. The biphase β is approximated as

$$\beta = -\frac{\pi}{2} + \frac{\pi}{2}\tanh\left(\frac{0.2}{Ur}\right),$$

where Ur is the Ursell number defined as

$$Ur = \frac{g}{8\sqrt{2}\pi^2}\frac{H_sT^2_{m01}}{H^2}.$$

Triad wave-wave interactions are only calculated for $0 \leq Ur \leq 1$. The interaction coefficient J is given by Madsen and Sørensen [91]:

$$J = \frac{k_{\sigma/2}^2(gH + 2c_{\sigma/2}^2)}{k_\sigma H(gH + \frac{2}{15}gH^3k_\sigma^2 - \frac{2}{5}\sigma^2H^2)},$$

where H is the total water depth.

The advancement of the physical description of waves is not a central goal of this work and therefore we have chosen to follow the source term implementation details of the well-validated SWAN model. However, SWAN employs the finite-difference method to propagate the waves while we use discontinuous Galerkin methods. These details will be described in the next chapter.

Chapter 3

Discontinuous Galerkin Methods for Spectral Wave Model

We discretize the action balance equation with discontinuous Galerkin methods in both geographic and spectral space and use explicit, Runge-Kutta methods for time-stepping. DG methods are locally mass conservative and highly parallelizable. DG methods allow for unstructured geographic meshes, which allow for a range of spatial resolutions. In addition, DG methods allow for higher-order approximations in both geographic and spectral spaces, which leads to increased accuracy. Adaptivity can easily be implemented for DG methods to selectively refine or coarsen the order of approximation to increase efficiency while maintaining the higher accuracy of increased order of approximation.

In this chapter, we will begin by introducing the weak formulations used to discretize the action balance equation in geographic and spectral space and the Runge-Kutta methods used to march in time. We then discuss some implementation details such as the numerical flux, elements, basis functions, and quadrature rules.

3.1 Weak Formulations

To obtain the weak form of the action balance equation, we first define the domain. We consider the entire domain Ω to be a tensor product of the geographic domain, $\Xi \in \mathbb{R}^2$, and the spectral domain, $\kappa \in \mathbb{R}^2$, so $\Omega \subset \mathbb{R}^2 \times \mathbb{R}^2$. The geographic domain consists of non-overlapping triangular elements, denoted Ξ_g, and the spectral domain consists of structured quadrilateral elements with constant spacing in directional space and logarithmic spacing in frequency space, so that $\kappa_s = (\sigma_\ell, \sigma_{\ell+1}) \times (\theta_m, \theta_{m+1}) \in \mathbb{R}^2$ where $\sigma_{\ell+1} = \gamma\sigma_\ell$ for a specified γ and $\theta_{m+1} = \theta_m + \Delta\theta$. Logarithmic spacing is used in frequency space so that there are more elements on the lower end of the frequency range, where the peak frequency is typically located and since logarithmic spacing is recommended for the DIA approximation. We define an individual element of the whole domain to be $\Omega_e = \Xi_g \times \kappa_s$, with boundary $\partial\Omega_e$ and $\mathbf{n}$ outward unit normal of $\partial\Omega_e$.

To formulate the DG method, we first obtain the weak form of the action balance equation by multiplying (2.1) by a test function v, integrating over each element Ω_e and integrating the divergence term by parts:

$$\left(\frac{\partial N}{\partial t}, w\right)_{L^2(\Omega_e)} - (\mathbf{c}N, \nabla w)_{L^2(\Omega_e)} + \langle \mathbf{c}N \cdot \mathbf{n}, w\rangle_{L^2(\partial\Omega_e)} = \left(\frac{S}{\sigma}, w\right)_{L^2(\Omega_e)} \quad \forall\Omega_e. \tag{3.1}$$

We then define a function space W_h, which allows for discontinuities between elements:

$$W_h = \{w \in L^2(\Omega) : w|_{\Omega_e} = \phi|_{\Xi_g} * \psi|_{\kappa_s} \in P^p(\Xi_g) * P^q(\kappa_s) \;\; \forall\Omega_e\} \tag{3.2}$$

where P^p is the space of polynomials of degree p defined on the geographic element Ξ_g and P^q is the space of polynomials of degree q defined on the spectral element κ_s. The action density, N, is approximated by $N_h \in W_h$, which satisfies the discrete weak formulation

$$\left(\frac{\partial N_h}{\partial t}, w_h\right)_{L^2(\Omega_e)} - (\mathbf{c}N_h, \nabla w_h)_{L^2(\Omega_e)} + \langle \mathbf{c}\hat{N}_h \cdot \mathbf{n}, w_h \rangle_{L^2(\partial\Omega_e)} = \left(\frac{S}{\sigma}, w_h\right)_{L^2(\Omega_e)} \quad \forall \Omega_e, \forall w_h \in W_h \tag{3.3}$$

where $\hat{N}_h$ is uniquely defined on the boundary by a numerical flux, which is discussed further in a following section.

3.2 Runge-Kutta Time Discretization

We rearrange (3.3) to the form

$$\frac{\partial}{\partial t} N_h = L_h(N_h, t)$$

and employ explicit, strong-stability preserving (SSP) s-stage k^{th}-order Runge-Kutta time-stepping schemes. These schemes have the property that, if the first-order forward Euler time discretization is stable under a given semi-norm and Courant-Friedrichs-Lewy (CFL) condition, then the higher-order scheme remains stable under the same semi-norm but potentially with a different CFL condition [75]. For the test cases in the next chapter, we employ the two stage, 2nd order scheme

$$N_h^{(1)} = N_h^n + \Delta t L_h(N_h^n, t_n)$$

$$N_h^{n+1} = \frac{1}{2}(N_h^n + N_h^{(1)} + \Delta t L_h(N_h^{(1)}, t_{n+1})).$$

In the following sections we continue by discussing the choice of numerical fluxes, elements, basis functions and quadrature rules.

3.3 Numerical flux

Because discontinuities are allowed between elements, N_h is not necessarily uniquely defined on the boundary; therefore we use a single-valued numerical flux, $\hat{N}_h$, on the edge boundaries instead. Numerical fluxes are defined in terms of a function's interior and exterior traces. The interior and exterior traces for any function $w \in W_h$ are as follows

$$w^{int}(\mathbf{x}) = \lim_{\epsilon \to \mathbf{0}^-} \mathbf{w}(\mathbf{x} + \epsilon \mathbf{n})$$

$$w^{ext}(\mathbf{x}) = \lim_{\epsilon \to \mathbf{0}^+} \mathbf{w}(\mathbf{x} + \epsilon \mathbf{n})$$

for any $\mathbf{x} = (x, y, \sigma, \theta) \in \partial\Omega_e$. A typical choice of numerical flux for scalar transport equations is an upwind flux, defined as

$$\hat{N}_h|_{\partial\Omega_e} = \begin{cases} N_h^{int} & \text{if } \mathbf{c} \cdot \mathbf{n}|_{\partial\Omega_e} > 0, \\ N_h^{ext} & \text{if } \mathbf{c} \cdot \mathbf{n}|_{\partial\Omega_e} \leq 0, \end{cases} \tag{3.4}$$

in which the flux depends on the propagation velocities $\mathbf{c}$ and therefore the total water depth and current. The total water depth and current are input parameters for the action balance equation, and in the coupled model, will be determined by DG-SWEM. The total water depth and current, computed by DG-SWEM, are allowed to have discontinuities across the geographic element

boundaries and so the propagation velocity $\mathbf{c}$ may not be uniquely defined in the above upwind flux. Therefore, we employ the Lax-Friedrichs flux

$$\begin{aligned}\mathbf{c}\hat{N}_h|_{\partial\Omega_e} =& \frac{1}{2}(N_h^{int}\mathbf{c}^{int}\cdot\mathbf{n} + N_h^{ext}\mathbf{c}^{ext}\cdot\mathbf{n}) \\ &- \frac{1}{2}\max\left[|\mathbf{c}^{int}\cdot\mathbf{n}|, |\mathbf{c}^{ext}\cdot\mathbf{n}|\right](N_h^{ext} - N_h^{int}),\end{aligned} \tag{3.5}$$

when there are potential discontinuities in the propagation velocities. Note that if the propagation velocities $\mathbf{c}$ are continuous across the element boundaries $\partial\Omega_e$, the Lax-Friedrichs Flux reduces to the upwind flux.

3.4 Boundary Conditions

The boundary conditions are enforced weakly through Dirichlet boundary conditions in both geographic and spectral space. In geographic space, two types of boundaries are considered: an incoming wave boundary or an absorbing boundary. For an incoming wave boundary, we specify the action density at the boundary by setting the exterior value N_h^{ext} in the flux to be the value of the incoming wave's action density. For an absorbing boundary, where there are no incoming waves and out-going waves simply propagate out of the domain, we set the exterior value N_h^{ext} in the flux to be zero. In frequency space, fully absorbing boundaries are used at both ends of the frequency range. In directional space, if the spectral domain is the full circle then periodic boundary conditions are used. If the spectral domain is only a sector, we apply absorbing boundary conditions at both ends of the directional domain.

3.5 Elements

Recall that the domain is composed of the tensor product of the geographic domain and the spectral domain. Because triangular elements are employed in geographic space and structured quadrilaterals in spectral space, we define a triangular master element for geographic space and a square master element for spectral space. After we define the master elements, we define the basis functions on the master elements. Computations on the physical element are then transformed to computations on the master elements for simplicity and efficiency. In geographic space, we choose the same master elements, basis functions and quadrature rules as those implemented in the DG-SWEM Model. Their details can be found in [75] and are repeated here for completeness.

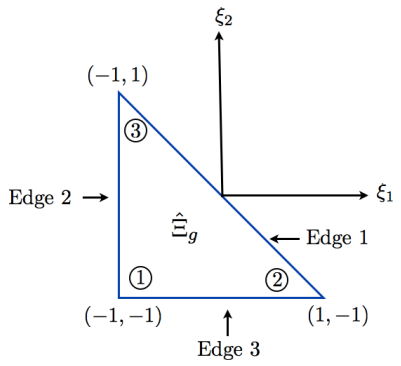

Figure 3.1: The geographic master element.

The geographic master element $\hat{\Xi}_g$, shown in Figure 3.1, is a right triangle with local coordinate system (ξ_1, ξ_2). The three vertices are numbered counter clockwise where edge i is opposite vertex i for $i = 1, 2, 3$. The master

element can be transformed to the physical element Ξ_g with coordinate system (x, y) and vertices (x_1, y_1), (x_2, y_2), and (x_3, y_3) numbered locally counter clockwise via the affine mapping

$$x = -\frac{1}{2}[(\xi_1 + \xi_2)x_1 - (1 + \xi_1)x_2 - (1 + \xi_2)x_3],$$
$$y = -\frac{1}{2}[(\xi_1 + \xi_2)y_1 - (1 + \xi_1)y_2 - (1 + \xi_2)y_3].$$

The inverse of the mapping, transforming a physical element to the master element, is

$$\xi_1 = \frac{1}{A_g}\{(y_3 - y_1)[x - \frac{1}{2}(x_2 + x_3)] + (x_1 - x_3)[y - \frac{1}{2}(y_2 - y_3)]\},$$
$$\xi_2 = \frac{1}{A_g}\{(y_1 - y_2)[x - \frac{1}{2}(x_2 + x_3)] + (x_2 - x_1)[y - \frac{1}{2}(y_2 - y_3)]\},$$

where $A_g = \frac{1}{2}[(x_2y_3 - x_3y_2) + (x_3y_1 - x_1y_3) + (x_1y_2 - x_2y_1)]$ is the area of Ξ_g. These transformations are shown in Figure 3.2.

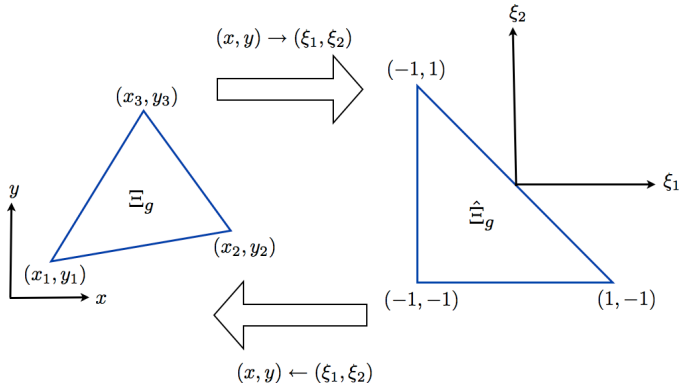

Figure 3.2: The geographic master element.

Derivatives of a function $f(\xi_1, \xi_2)$ defined on the master element $\hat{\Xi}_g$ with respect to the physical coordinates (x, y) can be computed via the chain

rule and the inverse mapping as follows:

$$\frac{\partial f}{\partial x} = \frac{\partial f}{\partial \xi_1}\frac{\partial \xi_1}{\partial x} + \frac{\partial f}{\partial \xi_2}\frac{\partial \xi_2}{\partial x} = \frac{\partial f}{\partial \xi_1}\frac{1}{A_g}(y_3 - y_1) + \frac{\partial f}{\partial \xi_2}\frac{1}{A_g}(y_1 - y_2),$$
$$\frac{\partial f}{\partial y} = \frac{\partial f}{\partial \xi_1}\frac{\partial \xi_1}{\partial y} + \frac{\partial f}{\partial \xi_2}\frac{\partial \xi_2}{\partial y} = \frac{\partial f}{\partial \xi_1}\frac{1}{A_g}(x_1 - x_3) + \frac{\partial f}{\partial \xi_2}\frac{1}{A_g}(x_2 - x_1).$$

Similarly, integration of a function $f(\xi_1, \xi_2)$ defined on the master element over the area of a physical element or its edge, Γ_i, can be transformed to an integration over the master element or its edge:

$$\int_{\Xi_g} f dx dy = \frac{A_g}{2}\left(\int_{\hat{\Xi}_g} f d\xi_1 d\xi_2\right),$$
$$\int_{\Gamma_i} f ds = \frac{l_i}{2}\left(\int_{-1}^{1} f ds\right),$$

where l_i is the length of edge i, Γ_i, of Ξ_g.

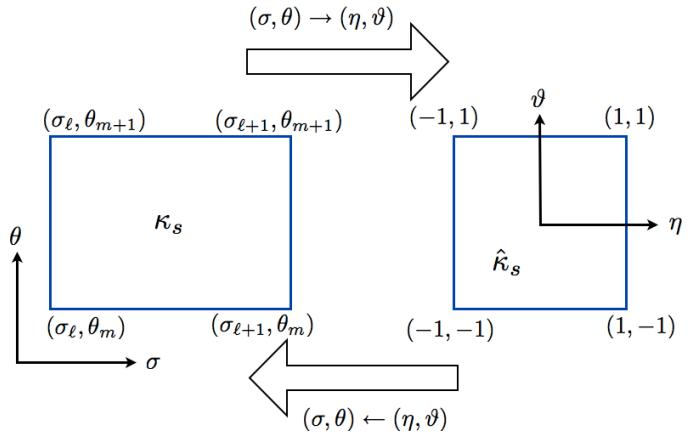

Figure 3.3: The spectral physical to master element.

In spectral space, the master element is defined on the coordinate system (η, ϑ) as

$$\hat{\kappa}_s = (-1, 1) \times (-1, 1).$$

To transform the physical element to the master element in spectral space, as seen in Figure 3.3, we use the mapping

$$\sigma(\eta) = \sigma = \frac{\Delta\sigma_\ell}{2}\eta + \frac{1}{2}(\sigma_\ell + \sigma_{\ell+1}),$$
$$\theta(\vartheta) = \theta = \frac{\Delta\theta}{2}\vartheta + \frac{1}{2}(\theta_m + \theta_{m+1}),$$

where $\Delta\sigma_\ell = \sigma_{\ell+1} - \sigma_\ell$. The inverse mapping to transform the master to the physical element is

$$\eta(\sigma) = \eta = \frac{2}{\Delta\sigma_\ell}(\sigma - \frac{1}{2}(\sigma_\ell + \sigma_{\ell+1})),$$
$$\vartheta(\theta) = \vartheta = \frac{2}{\Delta\theta}(\theta - \frac{1}{2}(\theta_m + \theta_{m+1})).$$

The derivatives of a function $f(\eta, \vartheta)$ defined on the master spectral element with respect to the physical coordinates are computed via the chain rule and inverse mapping

$$\frac{\partial f}{\partial \sigma} = \frac{\partial f}{\partial \eta}\frac{\partial \eta}{\partial \sigma} = \frac{\partial f}{\partial \eta}\frac{2}{\Delta\sigma_\ell},$$
$$\frac{\partial f}{\partial \theta} = \frac{\partial f}{\partial \vartheta}\frac{\partial \vartheta}{\partial \theta} = \frac{\partial f}{\partial \vartheta}\frac{2}{\Delta\theta}.$$

Also, integration of a function $f(\eta, \vartheta)$ defined on the master spectral element over the area of the physical element are transformed to integration over the master element:

$$\int_{\sigma_\ell}^{\sigma_{\ell+1}}\int_{\theta_m}^{\theta_{m+1}} f(\sigma,\theta)d\theta d\sigma = \frac{\Delta\sigma_\ell\Delta\theta}{4}\int_{-1}^{1}\int_{-1}^{1} f(\sigma(\eta),\theta(\vartheta))d\vartheta d\vartheta.$$

3.6 Basis Functions

Now that the master elements have been defined, we define the basis functions. As suggested by the definition of the function space V_h, we chose the basis functions to be products of basis functions defined on the geographic element, ϕ and basis functions defined on the spectral element, ψ. Using these basis functions, we express the approximated action density, N_h, with $(x, y) \in \Xi_g$ and $(\sigma, \theta) \in \kappa_s$ for time t_n, as

$$N_h(x, y, \sigma, \theta, t_n) = \sum_{i=1}^{M_{dof}} \sum_{k=1}^{N_{dof}} \alpha_{gisk}^{n} \phi_{g,i}(x, y) \psi_{s,k}(\sigma, \theta),$$

where $M_{dof} = \frac{1}{2}(p+1)(p+2)$ is the number of geographic degrees of freedom and basis functions with $\{\phi_{g,i}\}_{i=1}^{M_{dof}}$ spanning P^p and $N_{dof} = \frac{1}{2}(q+1)(q+2)$ is the number of spectral degrees of freedom and basis functions with $\{\psi_{s,k}\}_{k=1}^{N_{dof}}$ spanning P^q. We choose the basis functions to be hierarchical and orthogonal in both geographic and spectral space, which simplifies the implementation of p-adaptivity. Also, by choosing orthogonal basis functions, the mass matrix is diagonal and thus can be trivially inverted.

In geographic space, the orthogonal and hierarchical triangular basis of Dubiner [44] is implemented. These basis functions are also implemented in the DG-SWEM. The Dubiner basis is briefly discussed here and a detailed description of the basis can be found in [75]. The basis functions are defined on a square master element where the transformation from the triangular master element to the square master element illustrated in Figure 3.4 is given by

$$\eta_1 = \frac{2(1+\xi_1)}{(1-\xi_2)} - 1,$$

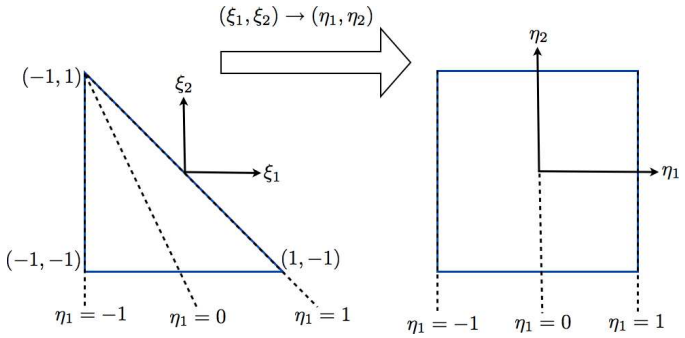

Figure 3.4: The geographic master element to the square master element used for basis functions.

$$\eta_2 = \xi_2.$$

The basis functions are the products of warped tensor product polynomials

$$\begin{aligned}
\Phi_i^{(1)} &= P_i^{0,0}(\eta_1), \\
\Phi_{ij}^{(2)} &= \left(\frac{1-\eta_2}{2}\right)^i P_j^{2i+1,0}(\eta_2),
\end{aligned}$$

where $P_n^{\alpha,\beta}(\cdot)$ is the n-th order Jacobi polynomial with weights α and β. The Dubiner basis functions are then

$$\Phi_{ij}(\xi_1, \xi_2) = \Phi_i^{(1)}(\eta_1)\Phi_{ij}^{(2)}(\eta_2).$$

Explicitly, the first few basis functions on the master geographic element denoted $\hat{\phi}_i$ are

$$\begin{aligned}
\hat{\phi}_1 &= \Phi_{00} = 1, \\
\hat{\phi}_2 &= \Phi_{01} = \frac{3}{2}\xi_2 + \frac{1}{2}, \\
\hat{\phi}_3 &= \Phi_{10} = \xi_1 + \frac{1}{2}\xi_2 + \frac{1}{2},
\end{aligned}$$

$$\hat{\phi}_4 = \Phi_{02} = \frac{5}{2}\xi_2^2 + \xi_2 - \frac{1}{2},$$
$$\hat{\phi}_5 = \Phi_{11} = \frac{5}{4}\xi_2^2 + \frac{5}{2}\xi_1\xi_2 + \frac{3}{2}\xi_1 + 2\xi_2\frac{3}{4},$$
$$\hat{\phi}_6 = \Phi_{20} = \frac{3}{2}\xi_1^2 + \frac{1}{4}\xi_2^2 + \frac{3}{2}\xi_1\xi_2 + \frac{3}{2}\xi_1 + \xi_2\frac{1}{4},$$

where they are organized hierarchically with constants ($i = 1$), linears ($i = 2-3$), and quadratics ($i = 4-6$). These geographic basis functions have the orthogonality property

$$(\hat{\phi}_i, \hat{\phi}_j)_{L^2(\hat{\Xi}_g)} = \int_{-1}^{1}\int_{-1}^{-\xi_2} \hat{\phi}_i\hat{\phi}_j d\xi_1 d\xi_2 = \frac{2}{(2i+1)(j+1)}\delta_{ij}.$$

In spectral space, the basis functions are chosen to be a tensor product of Legendre polynomials such that $\hat{\psi}_k(\eta, \vartheta) = P_i(\eta)P_j(\vartheta)$. The first six basis functions for constants (ψ_1), linears (ψ_{2-3}) and quadratics (ψ_{4-6}) are:

$$\hat{\psi}_1 = P_0(\eta)P_0(\vartheta) = 1,$$
$$\hat{\psi}_2 = P_0(\eta)P_1(\vartheta) = \vartheta,$$
$$\hat{\psi}_3 = P_1(\eta)P_0(\vartheta) = \eta,$$
$$\hat{\psi}_4 = P_0(\eta)P_2(\vartheta) = \frac{1}{2}(3\vartheta^2 - 1),$$
$$\hat{\psi}_5 = P_1(\eta)P_1(\vartheta) = \eta\vartheta,$$
$$\hat{\psi}_6 = P_2(\eta)P_0(\vartheta) = \frac{1}{2}(3\eta^2 - 1).$$

The basis functions have the following orthogonality property:

$$(\hat{\psi}_m(\eta, \vartheta), \hat{\psi}_n(\eta, \vartheta))_{\hat{\kappa}_s} = \int_{-1}^{1} P_{m_i}(\eta), P_{n_i}(\eta) d\eta \int_{-1}^{1} P_{m_j}(\vartheta), P_{n_j}(\vartheta) d\vartheta$$
$$= \frac{2}{2n_i + 1}\frac{2}{2n_j + 1}\delta_{mn}.$$

3.7 Quadrature Rules

Quadrature rules are employed to evaluate the integrals that appear in the discontinuous Galerkin discretization. Integrals over the edge and area of both geographic and spectral elements need to be evaluated. To maintain the accuracy of a discontinuous Galerkin approximation of order p, area integrals should be computed with a quadrature rule that is exact for polynomials of degree $2p$, and boundary integrals should be computed with a quadrature rule that is exact for polynomials of degree $2p + 1$ [22]. In spectral space, we use one-dimensional Gauss-Legendre quadrature rules for the edge integrals and products of Gauss-Legendre quadrature rules for the area integrals. Because an n-point Gauss-Legendre rule integrates a polynomial of degree $2n-1$ exactly, we use $q + 1$ quadrature points for the edge integrals and $(q + 1)^2$ quadrature points for area integrals in spectral space. Likewise, for the edge integrals in geographic space, we also use a $p + 1$ Gauss-Legendre quadrature rule. Products of Gauss-Legendre quadrature rules defined for the geographic square master element could also be used to evaluate integrals over the area of the geographic triangular element. However, to reduce the number of quadrature points and therefore increase the efficiency of the model, an efficient, high-degree symmetric Gaussian quadrature rule specifically for the triangle as defined in [45] (for up to degree $p = 20$) is implemented as it is in DG-SWEM [75]. The reduction in number of quadrature points can be seen, for example, in the degree 4 quadrature rule (required for quadratic polynomials), which requires only 4 quadrature points versus the 9 quadrature points needed

for the product of Gauss-Legendre quadrature rule.

3.8 Computation of Propagation Velocities

Evaluating the integrals via quadrature rules require the propagation velocities $\mathbf{c}$, to be evaluated at the quadrature points. To evaluate the propagation velocities requires the values or computation of values of the total water depth $H(x,t)$, current $u(x,t)$ and $v(x,t)$, the group velocity, c_g, and wave number, k. The depth and current are two input parameters and in the coupled model, will be determined by DG-SWEM. We express the depth and current input parameters, over the entire geographic domain, at time t_n in terms of the geographic basis functions as

$$H(x,t_n) = \sum_e \sum_i H_{n,i}\hat{\phi}_{e,i}(x),$$

$$u(x) = \sum_e \sum_i u_{n,i}\hat{\phi}_{e,i}(x),$$

and

$$v(x) = \sum_e \sum_i v_{n,i}\hat{\phi}_{e,i}(x).$$

We do not require that the depth or current have the same number of degrees of freedom as the action density, N, or each other. These expressions of the depth and current also assist in simplifying parts of the calculations of source terms which require derivatives of depth and the current.

The group velocity, c_g, and wave number, k, are approximated in different ways depending on whether the depth of the water is considered to be

deep, shallow, or somewhere in between. The wave number is related to the frequency via the dispersion relationship

$$\sigma^2 = gk \tanh(kH),$$

and the group velocity is

$$c_g = c_{ph} n$$

where the phase speed c_{ph} is

$$c_{ph} = \sqrt{\frac{g}{k} \tanh(kH)},$$

and

$$n = \frac{1}{2}\left(1 + \frac{2kH}{\sinh(2kH)}\right),$$

via the dispersion relationship [64]. Depending on the depth of the water, whether shallow or deep, we assume that as $kH \to 0$ that $\tanh(kH) \to kH$ or $kH \to \infty$ that $\tanh(kH) \to 1$ and make appropriate simplifications to compute the wave number and group velocity. Following SWAN, to determine if the depth is considered deep or shallow, a dimensionless frequency, $SND = \sigma * \sqrt{H(x_{qp})/g}$, is computed at each quadrature point [126]. SWAN employs Padè-type estimates when the water is neither deep or shallow to compute the parameters. Following SWAN's computations, we compute the group velocity, c_g, and wave number, k, as follows:

$$\left.\begin{array}{l} k = \sigma_\ell^2/g \\ n = \frac{1}{2} \\ c_g = \frac{1}{2} g/\sigma_\ell \end{array}\right\} \text{if deep water } (SND \geq 2.5) \ ,$$

$$\left.\begin{array}{l} k = \sigma_\ell / \sqrt{H(x_{qp}) g} \\ n = 1 \\ c_g = \sqrt{H(x_{qp}) g} \end{array}\right\} \text{if shallow water } (SND \leq 1 * 10^{-6}) \ ,$$

$$\left.\begin{array}{l} c_{ph} = \sqrt{\frac{g * H(x_{qp})}{SND^2 + \frac{1}{1 + 0.666 * SND^2 + 0.445 * (SND^2)^2 - 0.105 * (SND^2)^3 + 0.272 * (SND^2)^4}}} \\ k = \sigma_\ell / c_{ph} \\ n = \frac{1}{2}(1 + \frac{2kH(x_{qp})}{\sinh(2kH(x_{qp}))}) \\ c_g = n c_{ph} \end{array}\right\} \text{otherwise.}$$

Chapter 4

Verification and Validation of Spectral Wave Model

The discontinuous Galerkin spectral wave model is verified and validated using the method of manufactured solutions, comparisons to academic test cases, and comparisons to the well-known SWAN model. The experimental convergence rates are investigated by using a manufactured solution. We continue to verify and validate the model using test cases from the ONR test bed [114] which is a suite of test cases that have both academic and laboratory results. We also compare our results to those of SWAN, because SWAN is a widely used and well-trusted wave model. We also test our model's ability to propagate swell over large distances, to see if it is affected by the "Garden Sprinkler Effect", which is the disintegration of continuous swell into multiple discrete swells. In addition, we examine the parallel scalability of the DG spectral wave model and the benefits of using p-adaptivity to increase the computational efficiency of the model.

In some of the following test cases, we are interested in the steady-state solution. We consider the model to be in a steady state if stopping-criteria are met. The stopping-criteria are based on SWAN's stopping-criteria

for convergence of its iterative solver [126]. We consider three criteria: the absolute error

$$|H_s^i - H_s^{i-1}| \leq \epsilon_A,$$

the relative error

$$\frac{|H_s^i - H_s^{i-1}|}{H_s^{i-1}} \leq \epsilon_R,$$

and curvature error

$$\frac{|H_s^i - (H_s^{i-1} + H_s^{i-2} + H_s^{i-3}|}{H_s^i} \leq \epsilon_C$$

where the significant wave height H_s is determined at one point in each geographic element and i denotes the current time step or iteration. We consider the model to be at a steady state if all three error criteria are met for a percentage of the geographic elements. Typically, we require $\epsilon_A, \epsilon_R, \epsilon_C = 1 \times 10^{-5}$ for 95% of the elements. In addition, in some of the following cases, we are interested in the mean wave direction, which is an integrated quantity of action density and is calculated as follows

$$\overline{\theta} = \arctan\left(\frac{\int \sin\theta N \sigma d\sigma d\theta}{\int \cos\theta N \sigma d\sigma d\theta}\right).$$

4.1 Manufactured Solutions

We first examine individually the wave model with manufactured solutions. To inspect the convergence rates, β, we simplify the action balance equation by setting the propagation velocity to $\mathbf{c} = \mathbf{1}$ and the source term to $S = 0$ and use the manufactured solution

$$N = \sin(x - t) + \cos(y - t) + \sin(\sigma - t) + \cos(\theta - t),$$

where x, y, σ, θ and t are dimensionless. The geographic and spectral domains are $(0, L)\times(0, L)$, $L = 10$, and are discretized with triangles and quadrilaterals, respectively, with element size h. The series of geographic meshes are shown in Figure 4.1. A second order Runge-Kutta scheme is used with a time step of $\Delta t = 0.005$ s, so that errors due to the time discretization are negligible. The errors and convergence rates are shown in Table 4.1 for the initial condition. For $T = 5$ s, the error and convergence rates are recorded in Table 4.2 and the errors are plotted against the step size h and number of degrees of freedom in Figure 4.2. For h small enough, we obtain about $p + 1$ convergence rates.

Restricting to the geographic domain, we use the manufactured solution

$$N = \sin(x - t) + \cos(y - t),$$

to examine the convergence rates of Runge-Kutta methods of different orders. We employ the geographic mesh with $h = L/64$ and quartic approximations. Errors and convergence rates are shown in Table 4.3, which demonstrate the correct orders of approximations for each of the different ordered Runge-Kutta methods.

4.2 Current-Induced Shoaling and Refraction

To verify the wave model, we first test the propagation scheme in the presence of an ambient current (omitting source terms). We will examine four different cases of monochromatic, unidirectional waves, not necessarily normal to the coast, in the presence of different ambient currents, which are standard

	p,q = 0		p,q=1		p,q=2		p,q=3		p,q=4	
h	L2 error	β	L2 error	β	L2 error	β	L2 error	β	L2 error	β
$L/2$	146.6797	–	87.7164	–	40.1412	–	12.5245	–	2.0678	–
$L/4$	88.4044	0.7305	27.4349	1.6768	5.9322	2.7584	0.9200	3.7670	7.2995e-2	4.8242
$L/8$	46.0436	0.9411	7.2291	1.9241	0.7747	2.9369	5.9748e-2	3.9447	2.3583e-3	4.9520
$L/16$	23.2591	0.9852	1.8311	1.9811	9.7896e-2	2.9843	3.7700e-3	3.9863	7.4134e-5	4.9915
$L/32$	11.6595	0.9963	0.4593	1.9952	1.2270e-2	2.9961	2.3619e-4	3.9965	2.2390e-6	5.0492

Table 4.1: Error and convergence rate, β, in the initial condition for the manufactured solution.

	p,q = 0		p,q=1		p,q=2		p,q=3		p,q=4	
h	L2 error	β	L2 error	β	L2 error	β	L2 error	β	L2 error	β
$L/2$	134.5962	–	111.0265	–	53.8817	–	18.1940	–	4.0976	–
$L/4$	115.8146	0.2168	45.6310	1.2828	8.8633	2.6039	1.3717	3.7294	0.1453	4.8177
$L/8$	86.3410	0.4237	12.3717	1.8830	1.1659	2.9264	8.9412e-2	3.9394	4.9555e-3	4.8739
$L/16$	57.8860	0.5768	3.0650	2.0131	0.1479	2.9788	5.9012e-3	3.9214	-	-
$L/32$	35.2341	0.7162	0.7643	2.0037	1.8667e-2	2.9861	–	–	–	–

Table 4.2: Error and convergence rates, β, for the manufactured solution at $T = 5$ s.

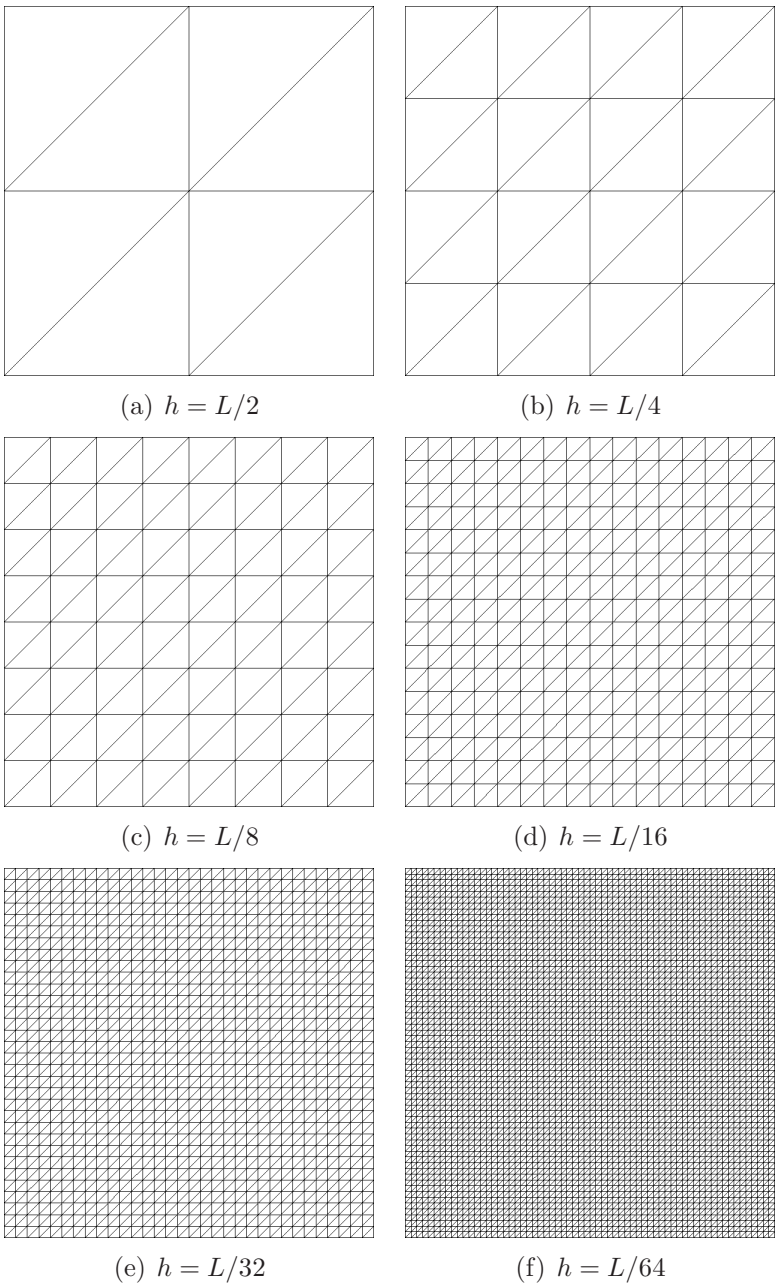

(a) $h = L/2$ (b) $h = L/4$

(c) $h = L/8$ (d) $h = L/16$

(e) $h = L/32$ (f) $h = L/64$

Figure 4.1: The sequence of geographic meshes for the manufactured solutions.

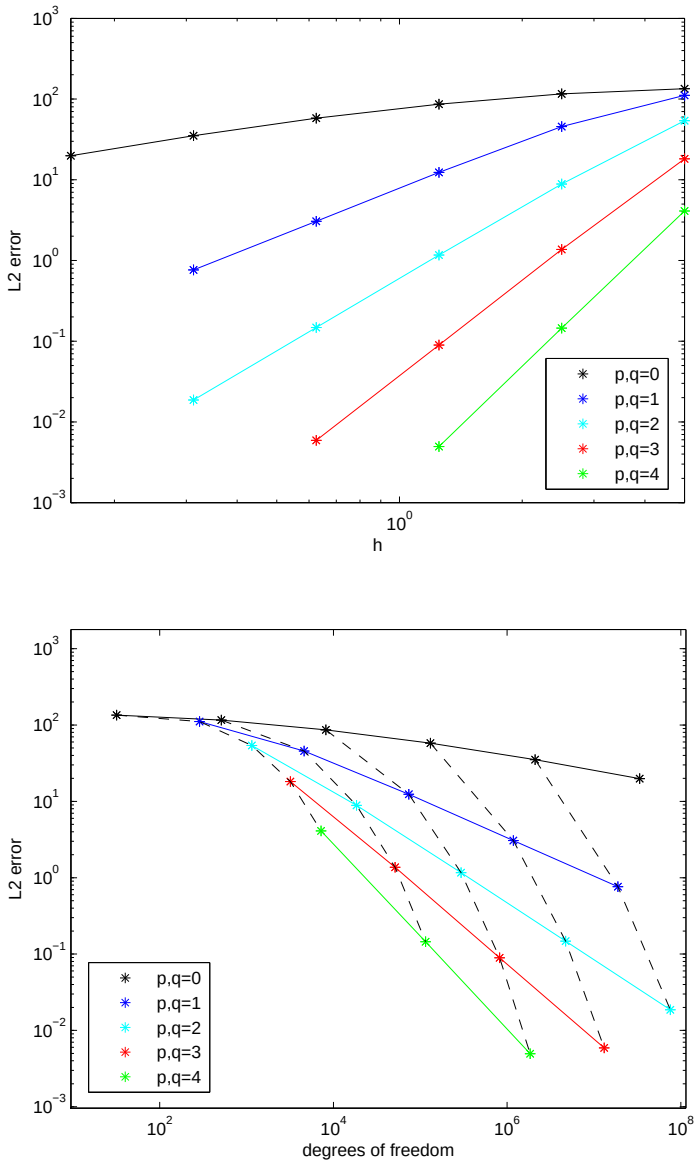

Figure 4.2: Errors of the manufactured solutions at $T = 5$ s.

	nRK=2,2		nRK=3,3		nRK=4,5	
Δt	L2 Error	β	L2 Error	β	L2 Error	β
0.01	2.3971e-5	–	1.2205e-6	–	8.3565e-8	–
0.005	2.3971e-5	0	1.2153e-7	3.3280	4.8452e-9	4.1083
0.0025	5.9911e-6	2.0004	1.3692e-8	3.1500	-	-
0.00125	1.4975e-6	2.0002	-	-	-	-
0.000625	3.7437e-7	2.0001	-	-	-	-

Table 4.3: Errors and convergence rates for different orders of Runge-Kutta methods.

test cases and can be found in the ONR test bed [114]. The first two cases examine an incoming wave traveling a distance from south to north of 4,000 m in deep water (H=10,000 m) in the presence of an opposing current (a) and a following current (b) with a velocity that increases from 0 to 2 m/s from the south to the north. Explicitly the current is

$$(a) \quad \mathbf{u} = \begin{pmatrix} 0 \\ -2/4,000y \end{pmatrix} m/s, \qquad (b) \quad \mathbf{u} = \begin{pmatrix} 0 \\ 2/4,000y \end{pmatrix} m/s.$$

The incoming, monochromatic, long-crested waves are simulated with a Gaussian-shaped frequency spectrum, with peak frequency 0.1 Hz, standard deviation 0.01 Hz, and a $\cos^{500}(\theta)$ directional distribution (i.e., directional spreading is 5° [79]). The waves have a significant wave height of 1 m and a main direction of 90°. The incoming wave boundary is indicated with a blue line on the geographic mesh shown in Figure 4.3. All other boundaries are absorbing. The spectral domain has 40 logarithmically distributed elements in frequency space that range from 0.05-0.25 Hz, which does not include the blocking frequency in the opposing current case, and has constant directional element spacing of

$\Delta\theta = 2°$. The incoming wave boundary conditions are shown in Figure 4.4 (a) and (b) along with the corresponding spectral meshes.

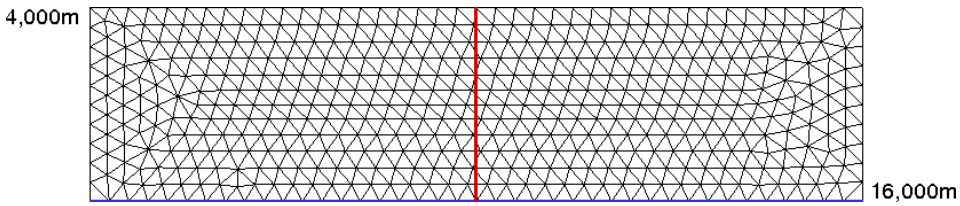

Figure 4.3: The geographic mesh for the ambient current test cases. The blue line indicates the incoming wave boundary and the red line indicates the segment along which the steady state solutions are shown. There are 936 triangular elements, 519 nodes, and $h \approx 400$ m.

We are interested in the steady-state solution along the center of the geographic domain (the red line shown in Figure 4.3). Steady-state solutions are achieved when there is little to no change in consecutive time-steps ($\Delta t = 2$ s) of the significant wave height in each geographic element. The results are shown in Figure 4.5 curves (a) and (b). The DG solution is the black line and employs linears in both geographic and spectral space. We also show SWAN's stationary solution with the same numerical settings and also omitting source terms in blue for comparison because it is a well-trusted and widely-used wave model. The red line is the analytic solution (e.g. [69, 108]), which is

$$\frac{H_s^2}{H_{s,i}^2} = \frac{c_i^2}{c(c+2U)}$$

in which H_s is the wave height and c is the group velocity, where i represents the incident value. The DG solutions closely follow the analytic solutions.

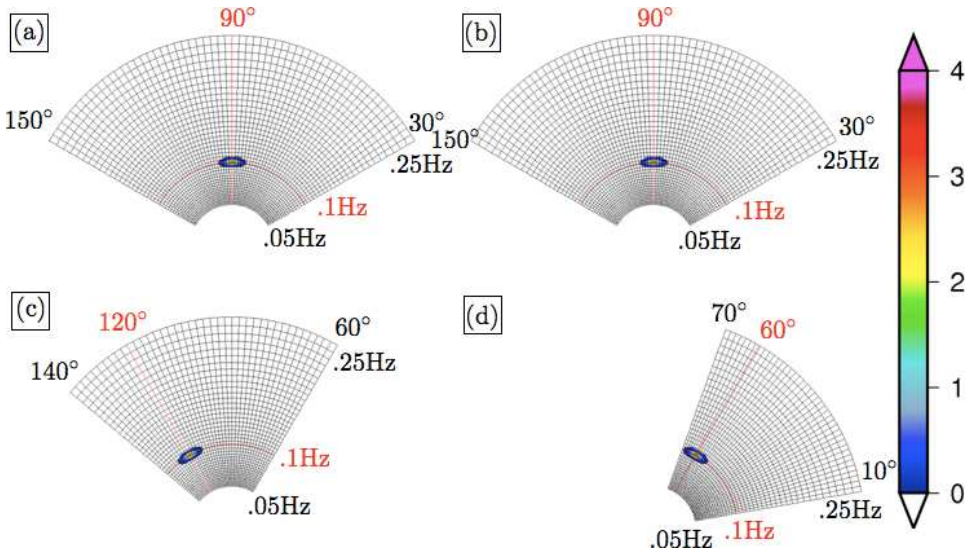

Figure 4.4: The action density in $m^2/Hz/^\circ$ specified at the southern boundary (blue line in Figure 4.3) of the four current test cases are shown on their respective spectral meshes. The main direction and peak period are indicated on the spectral mesh with red lines. Note the spectral mesh is plotted in polar coordinates (σ, θ) to emphasize that θ is a direction, although spectral space is treated as a Cartesian coordinate system in the numerical method.

Note that SWAN produces significant wave heights that are larger than the analytic solution for the opposing current case. SWAN's solution improves slightly when we use $\Delta\theta = 0.2^\circ$ and 160 frequency elements. Higher order approximations can be successfully used in both geographic and spectral space as shown in Figure 4.6 for the opposing current case (a). We notice a significant improvement by increasing the order of approximation from constants to linears in both geographic and spectral space.

The final two ambient current test cases turn the previous incoming waves by $\pm 30^\circ$ (for incoming main wave directions of 120° (c) and 60° (d)) in the presence of a slanted current,

$$\mathbf{u} = \begin{pmatrix} 2/4,000y \\ 0 \end{pmatrix} m/s.$$

The analytic solution (e.g. [62, 69]) is

$$H_s = H_{s,i}\sqrt{\frac{\sin(2\theta_i)}{\sin(2\theta)}}$$
$$\theta = \arccos\left[\frac{gk_i\cos(\theta_i)}{(\omega - Uk_i\cos(\theta_i))^2}\right].$$

Again we use the geographic mesh shown in Figure 4.3. The spectral domain has 40 logarithmically distributed elements in frequency space that range from 0.05-0.25 Hz and has constant directional element spacing of $\Delta\theta = 2^\circ$ (c) or $\Delta\theta = 1.5^\circ$ (d). The incoming wave boundary conditions are shown in Figure 4.4 (c) and (d) along with the corresponding spectral meshes. The steady-state solutions of the significant wave height and main wave direction are shown in Figure 4.5 curves (c) and (d). The DG solutions using linears in

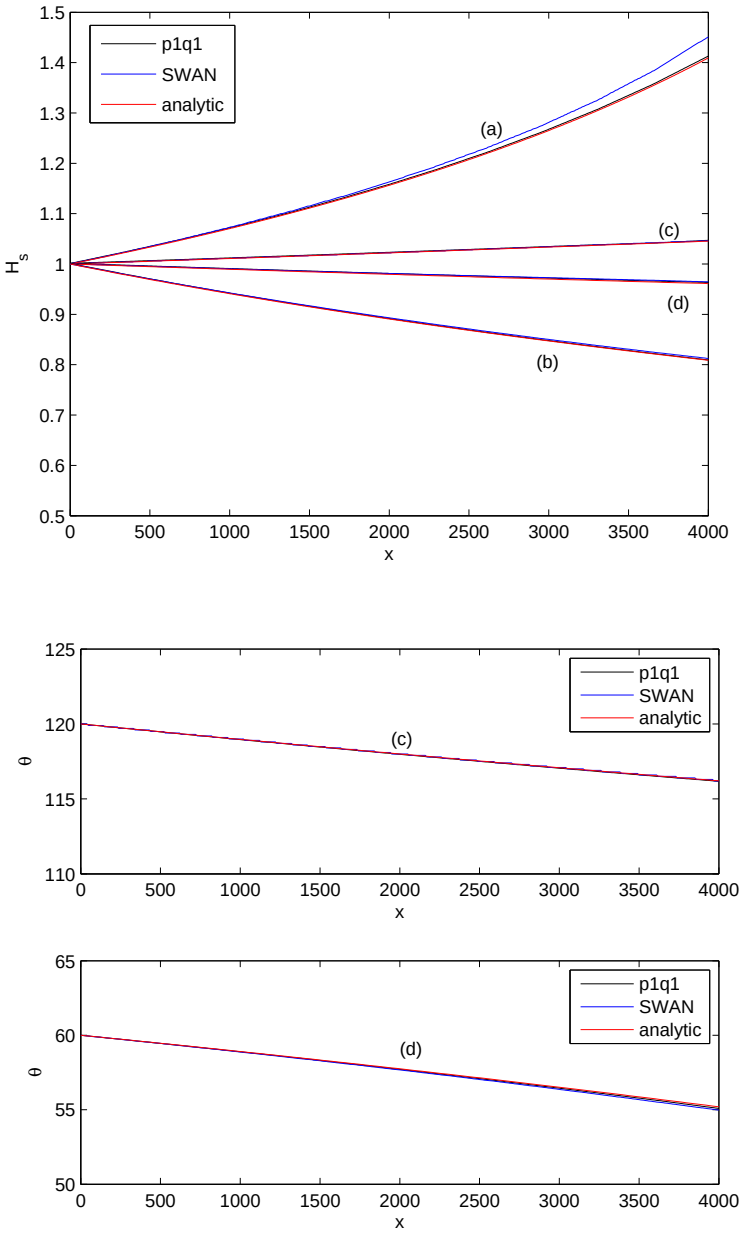

Figure 4.5: Steady state solutions of the significant wave height, H_s, and the main direction, θ, for the ambient current test cases. The DG solution utilizing linears in both geographic and spectral space is compared to SWAN and the analytic solutions.

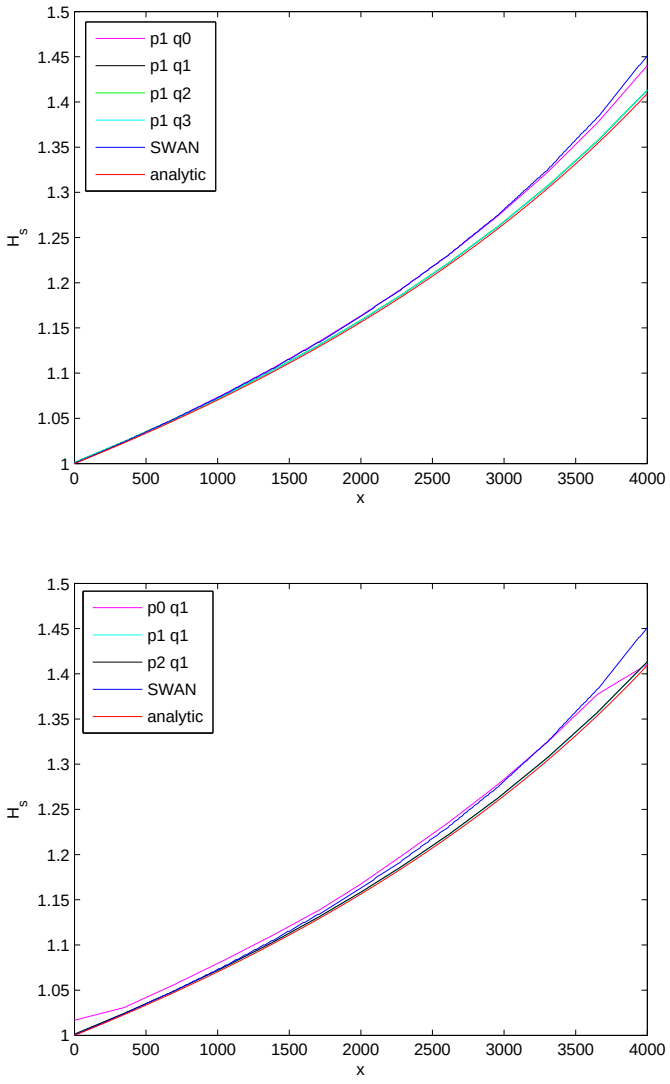

Figure 4.6: Steady state solutions of the significant wave height for the opposing current case (a). The DG solution using higher orders of approximation are compared to SWAN and the analytic solution. On the top, linears are used in geographic space ($p = 1$) and constants, linears, quadratics, and cubics are used in spectral space ($q = 0, 1, 2, 3$). On the bottom, linears are utilized in spectral space ($q = 1$) while constants, linears, and quadratics are used in geographic space ($p = 0, 1, 2$).

geographic and spectral space (shown in black) closely match the analytic solutions (shown in red) for both the significant wave height and the main direction, demonstrating our model's ability to closely model incoming waves in the presence of an ambient current.

Further examining the opposing current case (a), we explore the benefit of using higher order approximations in geographic and spectral space. For this discussion, we consider a coarse and a fine mesh. The coarse geographic mesh, Figure 4.7 (a), has 1/16 of the resolution of the geographic fine mesh, Figure 4.7 (b) and the coarse spectral mesh only has about half the resolution as the fine spectral mesh ($\Delta\theta = 2^\circ$, 40 logarithmically distributed frequency elements). The steady state solutions of the significant wave height are shown in Figure 4.8. Note that the SWAN fine mesh solution (shown in blue) is a significant improvement from its coarse mesh solution (shown in cyan), which does not provide enough resolution. We show two DG solutions that employ either the coarse or fine mesh but have similar numbers of degrees of freedom. The first, shown in green, employs the fine mesh with constant approximations in both geographic and spectral space ($p, q = 0$) and the second, shown in black, employs the coarse mesh but with higher order approximations, linears in geographic space and cubics in spectral space ($p = 1$, $q = 3$). These simulations have 7.68 million and 3.6 million degrees of freedom, respectively. Comparing the SWAN fine mesh and the DG low-order, fine mesh solutions, we observe that SWAN's fine mesh solution is a better match to the analytic solution (shown in red). This is not unexpected, because SWAN is using

a higher order approximation than the constant approximation of the DG solution. Comparing the two DG solutions, we see a significant benefit in using higher orders of approximations on the coarse mesh versus a lower order of approximation on the fine mesh, even though the higher order solution has less than half the number of degrees of freedom. In particular, note that the coarse, higher-order solution matches the analytic solution, shown in red, better than the lower-order, fine mesh DG solution as well as SWAN's fine mesh solution.

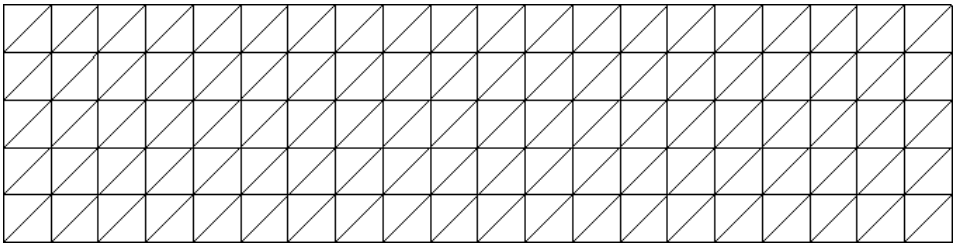

(a) coarse mesh

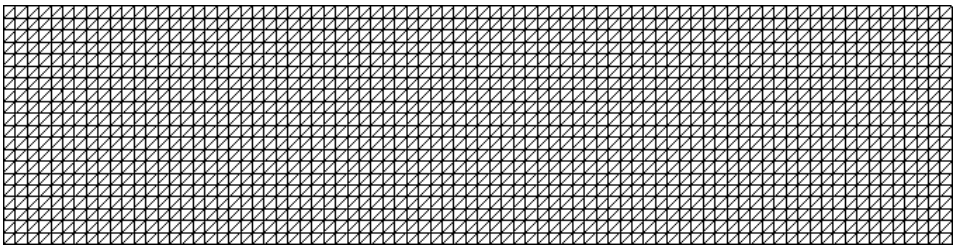

(b) fine mesh

Figure 4.7: The coarse and fine meshes used for the opposing current case in Figure 4.8.

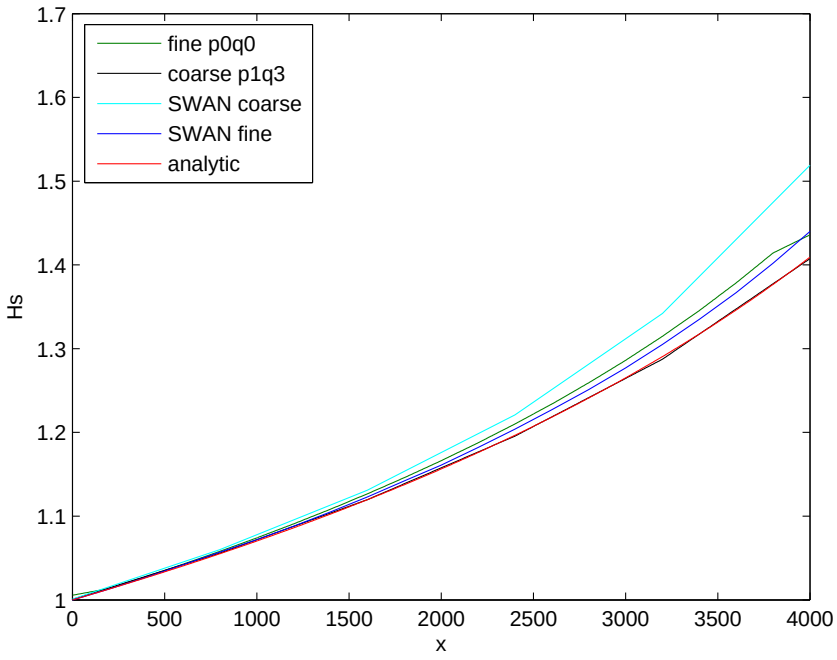

Figure 4.8: The steady-state solutions of the significant wave height for the opposing current case (a) are shown. We compare two DG solutions with similar numbers of degrees of freedom, one on the fine mesh with constants and the second on the coarse mesh with linears in geographic space and cubics in spectral space. SWAN solutions on both the coarse and fine meshes along with the analytic solution are also shown.

4.3 Depth-Induced Shoaling and Refraction

We now test the propagation of monochromatic, long-crested waves in shallow water with varying depth and no current. We consider a wave propagating toward a plane beach over a distance of 4,000 m from a depth of 20 m (slope 1:200). The incoming wave has a significant wave height of 1 m, a Gaussian-shaped frequency spectrum, with peak frequency 0.1 Hz, standard deviation 0.01 Hz, and a $\cos^{500}(\theta)$ directional distribution. To test depth-induced shoaling, we consider the incoming wave to have a main direction of 90° (a), and to test depth-induced refraction, we consider the incoming wave to have a main direction of 120° (b). The analytic solution for both cases is given by (e.g. [94])

$$\frac{H_s^2}{H_{s,i}^2} = \frac{c_i}{c}\frac{\cos(\theta_i)}{\cos(\theta)}$$

and the wave direction is calculated with Snell's law. The geographic mesh is shown in Figure 4.9; the element size h varies from 800 m to 20 m as the depth decreases from 20 m to 0 m ($d = 20 - 1/200y$). The spectral mesh has 40 frequency elements distributed logarithmically from 0.01-0.25 Hz and

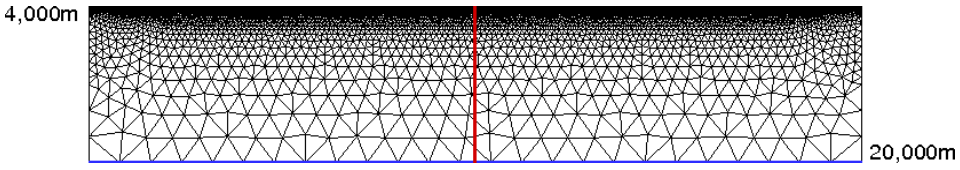

Figure 4.9: The geographic mesh for the depth-induced shoaling and refraction cases. The blue line indicates the incoming wave boundary and the red line indicates the line along which the steady state solutions are considered. There are 13,841 triangular elements, 7,458 nodes, and h varies from 800 to 20 m.

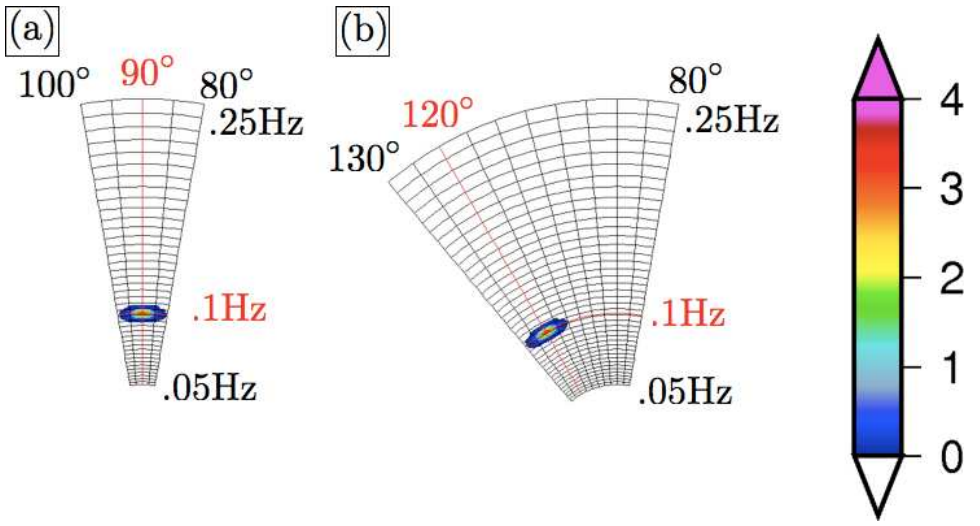

Figure 4.10: The action density in $m^2/Hz/^\circ$ specified at the boundary (blue line in FIgure 4.9) of the depth-induced shoaling and refraction cases. The main direction and peak period are indicated on the spectral mesh with red lines. Note the spectral mesh is plotted in polar coordinates (σ, θ) to emphasize that θ is a direction, although spectral space is treated as a Cartesian coordinate system in the numerical method.

the directional elements have a constant spacing of $\Delta\theta = 5^\circ$ (SWAN solutions use $\Delta\theta = 0.25^\circ$). The spectral meshes (for the DG solutions) are shown in Figure 4.10, along with the boundary conditions used in the two cases. In Figure 4.11, the steady-state solution of the significant wave height and main direction are shown where the x-axis corresponds to the red line indicated on the geographic mesh in Figure 4.9. The DG solution employing linears in geographic and spectral space is shown in black and SWAN is shown in blue (for depths greater than 0.05m). The DG model closely reproduces the analytic solution, shown in red, for the significant wave height and the turning

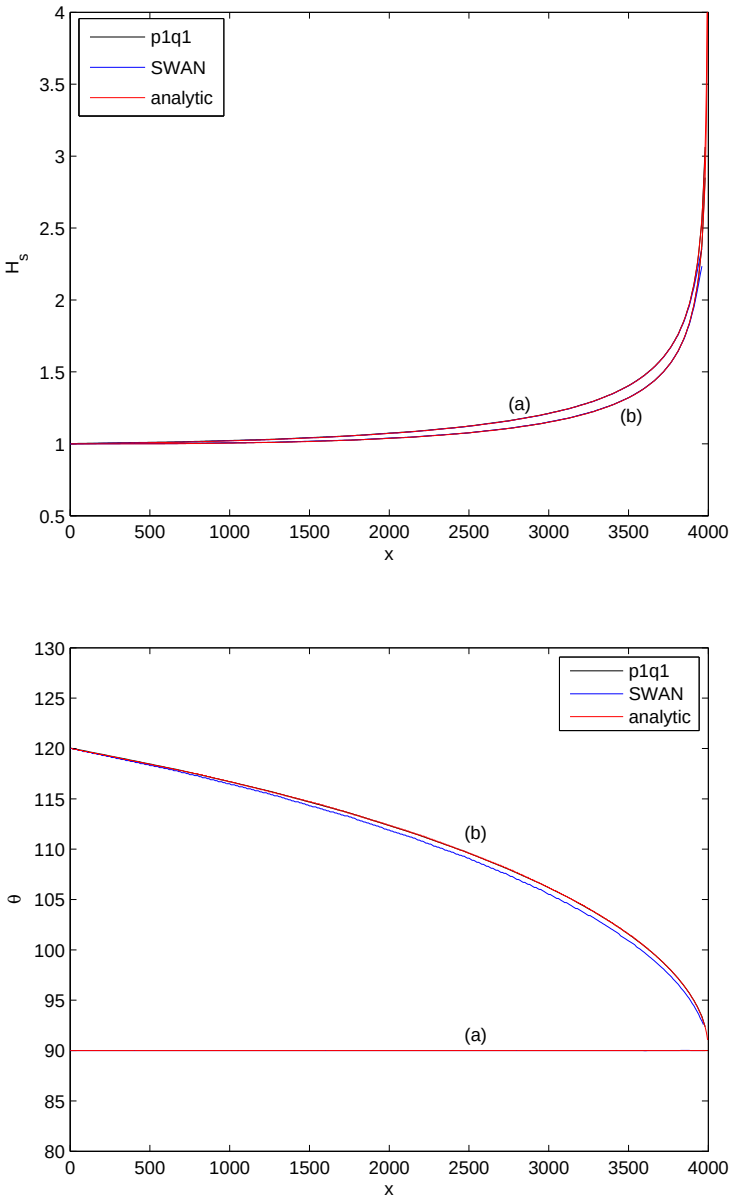

Figure 4.11: Steady state solutions of the significant wave height, H_s, and the main direction, θ, to the depth-induced shoaling and refraction cases. The DG solution utilizing linears in both geographic and spectral space is compared to SWAN and analytic solutions.

of the main direction. Note the improved match to the analytic solution for wave directions, relative to SWAN.

4.4 Garden Sprinkler Effect

As irregular, short-crested waves or wind sea, generated by local wind or storm, propagates out of the generation area, the waves disintegrate through dispersion processes into regular, long-crested waves or swell [64]. This dispersion occurs continuously; however, in numerical models when the energy is represented discretely, the initial irregular wave field disintegrates into multiple wave fields for each discrete direction/frequency. This is known as the "garden sprinkler" effect (GSE) [10, 129]. Numerical models frequently are required to propagate swell over large geographic distances and the GSE can lead to poor prediction of the arrival of swell from distant storms [10]. We investigate if the DG model is affected by the GSE while propagating swell.

An example of the GSE is shown in Figure 4.12. This test case appears in Tolman [129], and we investigate how our DG model propagates waves over large distances. In this test we employ the simplified action balance equation omitting refraction, frequency shifting and source terms (c_θ, c_σ, and $S = 0$). This test case involves an area of 4,000 km $\times$ 3,500 km of deep water ($H = 10$ km). An initial wave field is located 500 km from the lower and left side of the domain with a significant wave height of 2.5 km. The wave field has a main direction of 30° with a $\cos^2(\theta)$ directional distribution, a mean frequency of 0.1 Hz with a Gaussian spread of 0.01 Hz, and a Gaussian spread of 150

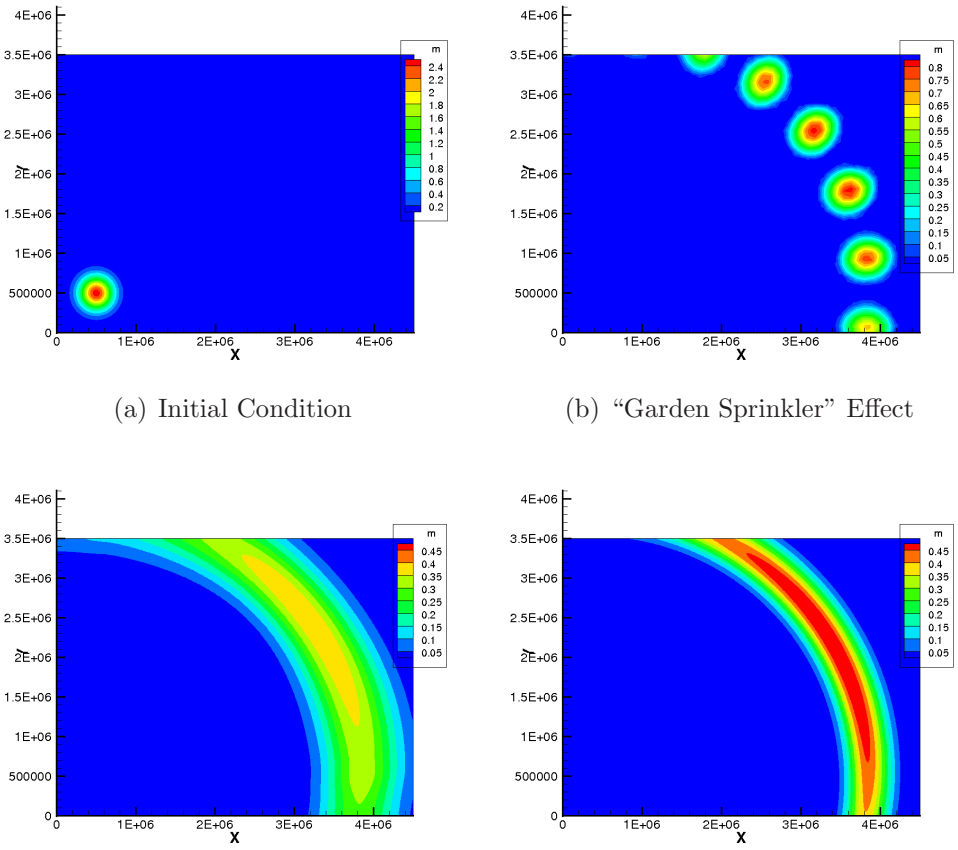

(a) Initial Condition

(b) "Garden Sprinkler" Effect

(c) Fine Scale Solution ($p = 0$, $q = 1$)

(d) Fine Scale Solution ($p = 1$, $q = 1$)

Figure 4.12: The initial condition for the GSE test case is shown in (a). The solution after 5 days with the "Garden Sprinkler" effect is shown in (b) and two fine-scale solutions are shown in (c) and (d), using constants or linears in geographic space and linears in spectral space.

km in geographic space. We investigate what happens to the initial wave field, shown in Figure 4.12(a), after 5 days of computation. In Figure 4.12 (c) and (d), the fine scale solution of the significant wave height is shown after 5 days and in Figure 4.12 (b) the GSE is shown. The results in Figure 4.12 (b), which shows the effect of GSE, were computed by the DG model with linears in geographic space and constants in spectral space ($p = 1$, $q = 0$), $h = 100$ km, $\Delta\theta = 15°$, and $\gamma = 1.041$. The two fine scale solutions use increased geographic resolution of $h = 25$ km and increased spectral resolution of $\Delta\theta = 2.°$, with linears in spectral space and either constants in geographic space (c) or linears in geographic space in (d). In the fine-scale solutions, we notice the constant approximation in spectral space is more diffusive than the linear approximation. There is no analytic solution for this test case, however Tolman's fine-scale "exact" solution [129] is closer to the constant approximation solution in Figure 4.12(c).

As we have seen, the DG model using linears in geographic space and constants in spectral space can suffer from the GSE. We investigate how the DG model preforms on the original, coarse mesh ($h = 100$ km, $\Delta\theta = 15°$, and $\gamma = 1.041$) using different orders of approximations. Figure 4.13 uses constants ($p = 0$) in geographic space, Figure 4.14 uses linears ($p = 1$), Figure 4.15 uses quadradics ($p = 2$), and Figure 4.16 uses cubics ($p = 3$) in geographic space, each with multiple spectral orders of approximation ($q = 0, 1, 2, 3, 4$). For each of the different geographic orders, we see that by increasing the spectral order of approximation the GSE is decreased. We also notice that the

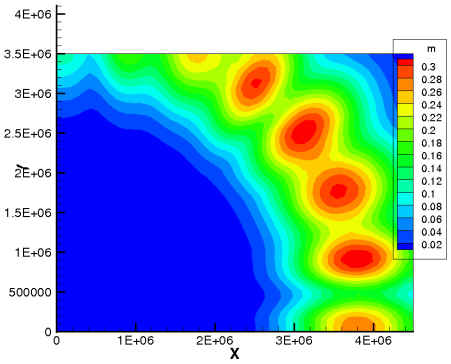

(a) $p = 0$, $q = 0$

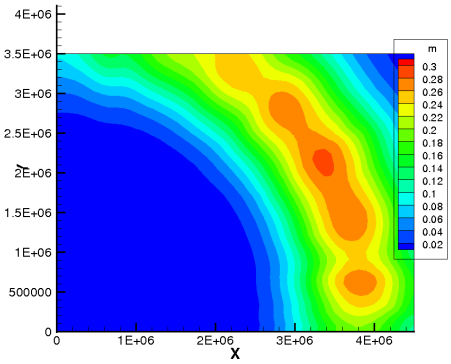

(b) $p = 0$, $q = 1$

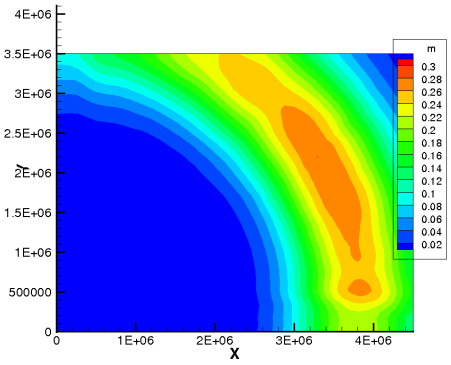

(c) $p = 0$, $q = 2$

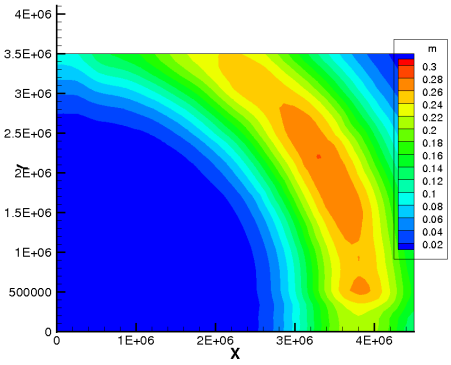

(d) $p = 0$, $q = 3$

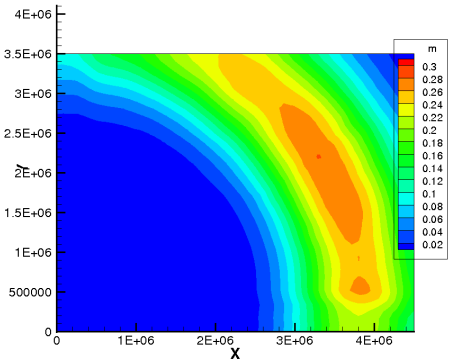

(e) $p = 0$, $q = 4$

Figure 4.13: The significant wave height for the GSE test after 5 days is shown for the DG solutions employing constants in geographic space and constants (a) through quartics (e) in spectral space.

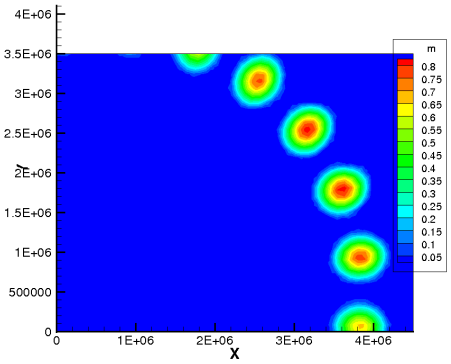

(a) $p = 1$, $q = 0$

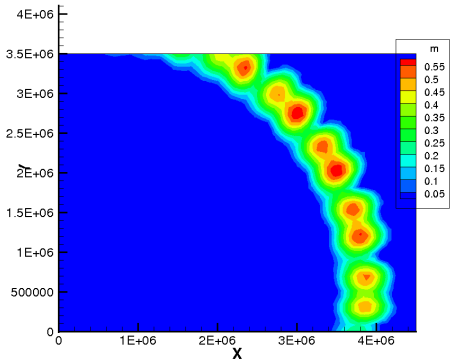

(b) $p = 1$, $q = 1$

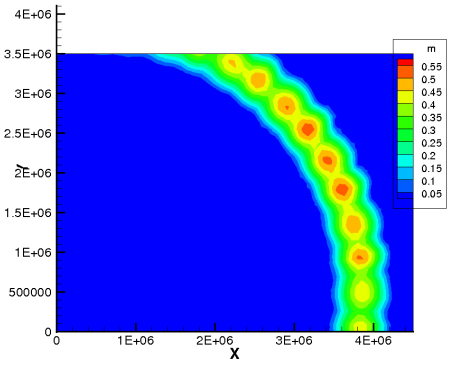

(c) $p = 1$, $q = 2$

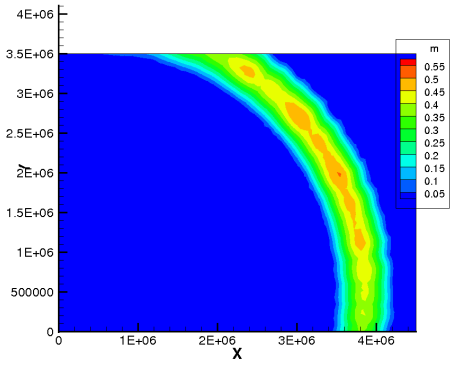

(d) $p = 1$, $q = 3$

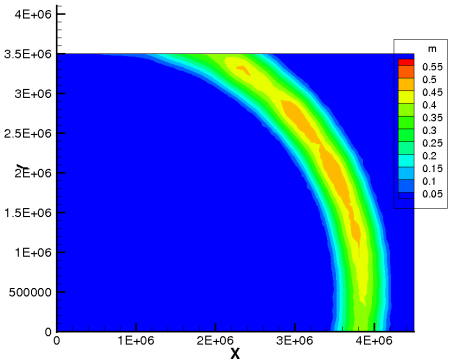

(e) $p = 1$, $q = 4$

Figure 4.14: The significant wave height for the GSE test after 5 days is shown for the DG solutions employing linears in geographic space and constants (a) through quartics (e) in spectral space.

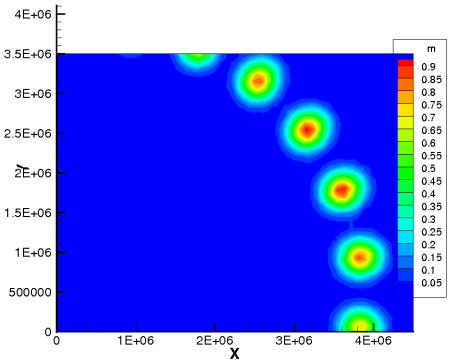

(a) $p = 2$, $q = 0$

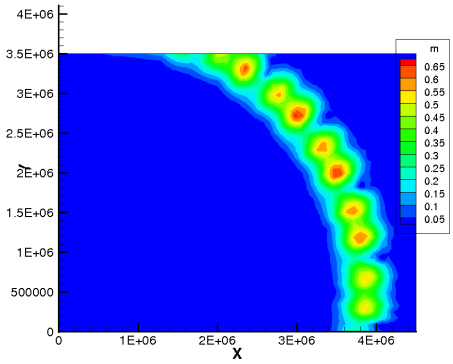

(b) $p = 2$, $q = 1$

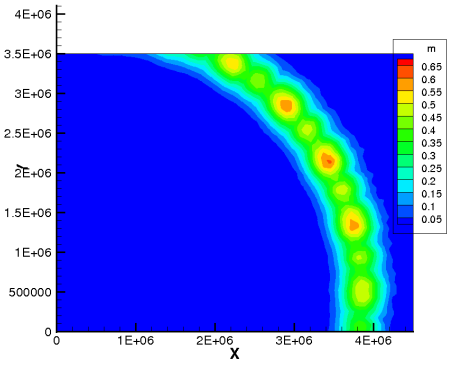

(c) $p = 2$, $q = 2$

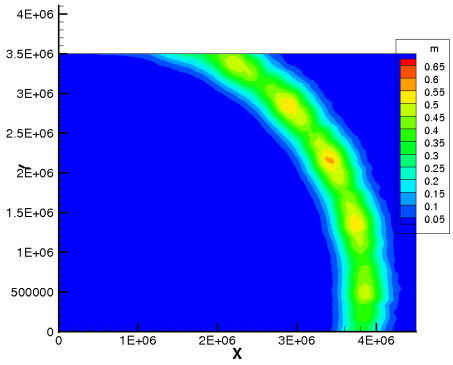

(d) $p = 2$, $q = 3$

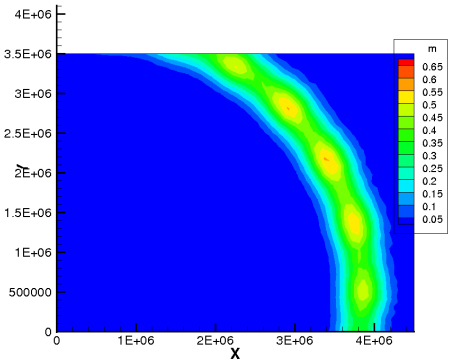

(e) $p = 2$, $q = 4$

Figure 4.15: The significant wave height for the GSE test after 5 days is shown for the DG solutions employing quadratics in geographic space and constants (a) through quartics (e) in spectral space.

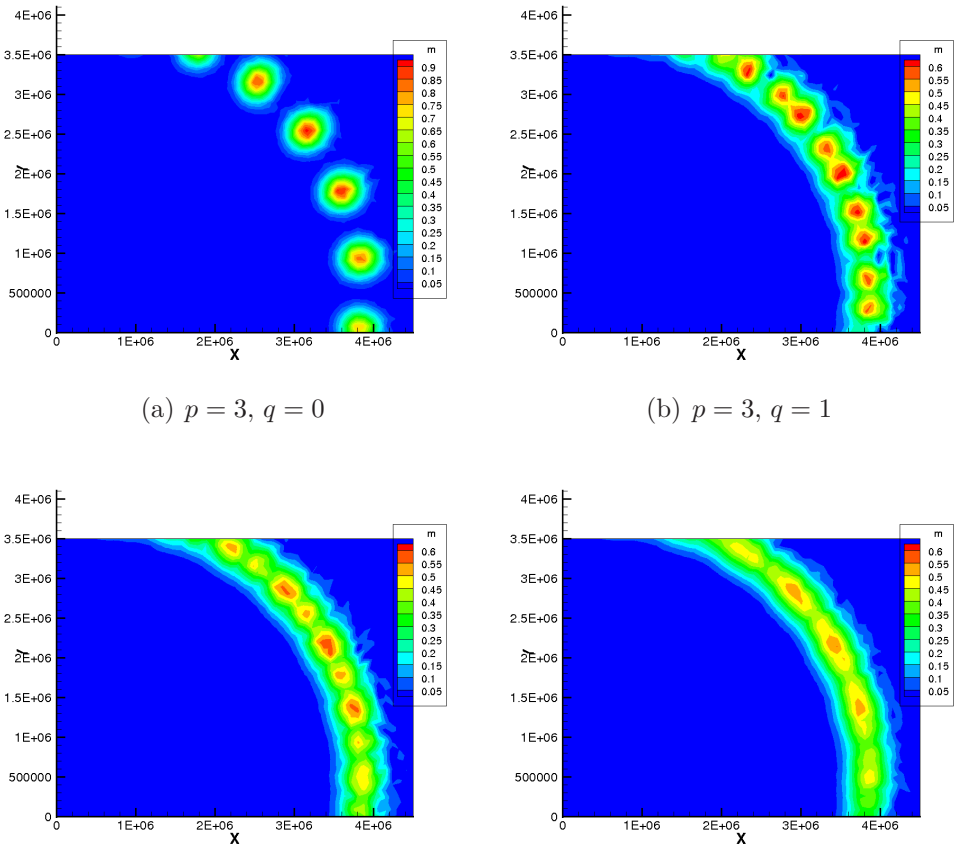

(a) $p = 3$, $q = 0$

(b) $p = 3$, $q = 1$

(c) $p = 3$, $q = 2$

(d) $p = 3$, $q = 3$

Figure 4.16: The significant wave height for the GSE test after 5 days is shown for the DG solutions employing cubics in geographic space and constants (a) through cubics (d) in spectral space.

constant approximation in geographic space is more diffusive than the higher order geographic approximations and therefore naturally alleviates some of the GSE. We also see that the constant solution is more diffusive than the linear geographic solution in the two fine scale solutions, Figures 4.12 (c) and (d), even though neither are affected by the GSE due to the increased resolution.

We also investigate the effect on the results when different unstructured geographic meshes are used. In Figure 4.17, we show four different geographic meshes all with $h = 100$ km where (a) and (b) employ structured triangles with different orientations, (c) is a 'Union Jack' mesh and (d) is a mesh generated by SMS [3] (which was used in Figures 4.13-4.16). In Figures 4.18-4.21, we show results for the different geographic meshes for selected orders of approximation. We see that employing mesh (a) which uses structured triangles alleviates the GSE more than the other unstructured meshes especially in Figure 4.18 which uses constants in both geographic and spectral space and in Figure 4.19 which uses constants in geographic space and quadratics in spectral space. In Figure 4.20 which uses linears in both geographic and spectral space and Figure 4.21 which uses linears in geographic space and quartics in spectral space, we see smaller differences in the results for the different geographic meshes and by using the higher order approximations the GSE is eased.

For comparison, we also examine how SWAN performs in the GSE test. SWAN results for the four unstructured geographic meshes are shown in Figure 4.22. SWAN also has the least GSE when using the geographic mesh (a) but cases (b)-(d) all have the GSE. To alleviate the GSE, the ideal solution is to

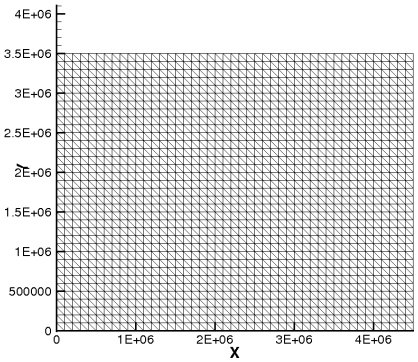

(a) Triangle Orientation 1 Mesh

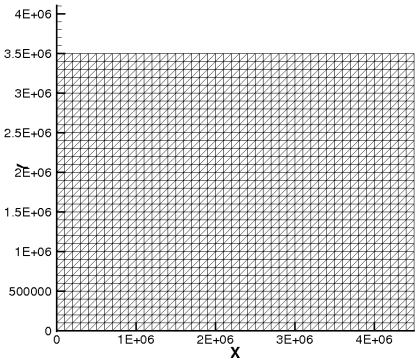

(b) Triangle Orientation 2 Mesh

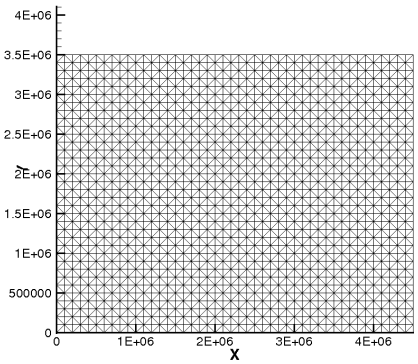

(c) Union Jack Mesh

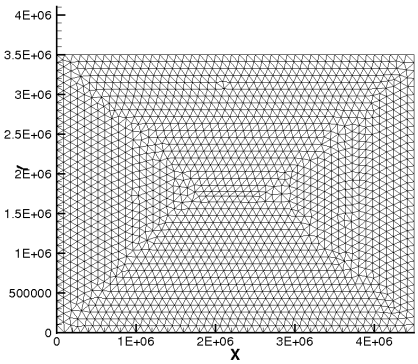

(d) SMS Mesh

Figure 4.17: Four different geographic, unstructured meshes with $h = 100$ km used for the GSE test case.

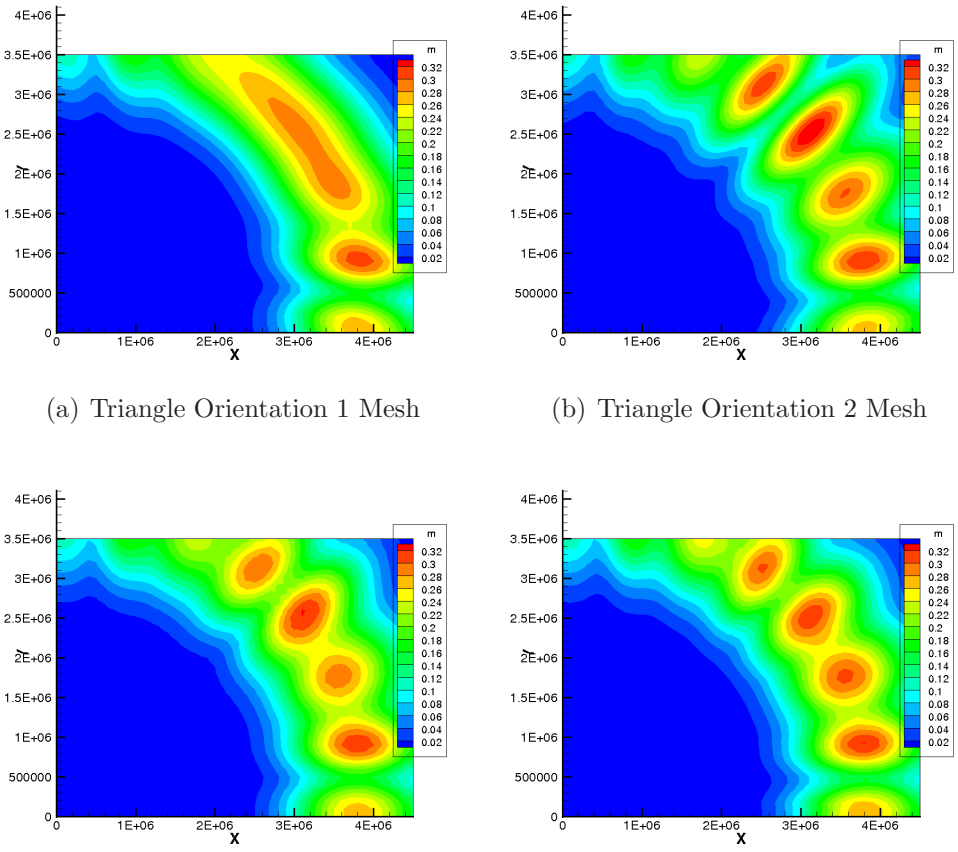

(a) Triangle Orientation 1 Mesh

(b) Triangle Orientation 2 Mesh

(c) Union Jack Mesh

(d) SMS Mesh

Figure 4.18: DG solutions of the significant wave height after 5 days for the GSE test case, which employ constants in both geographic and spectral space $(p, q = 0)$ for each the four geographic meshes in Figure 4.17, are shown.

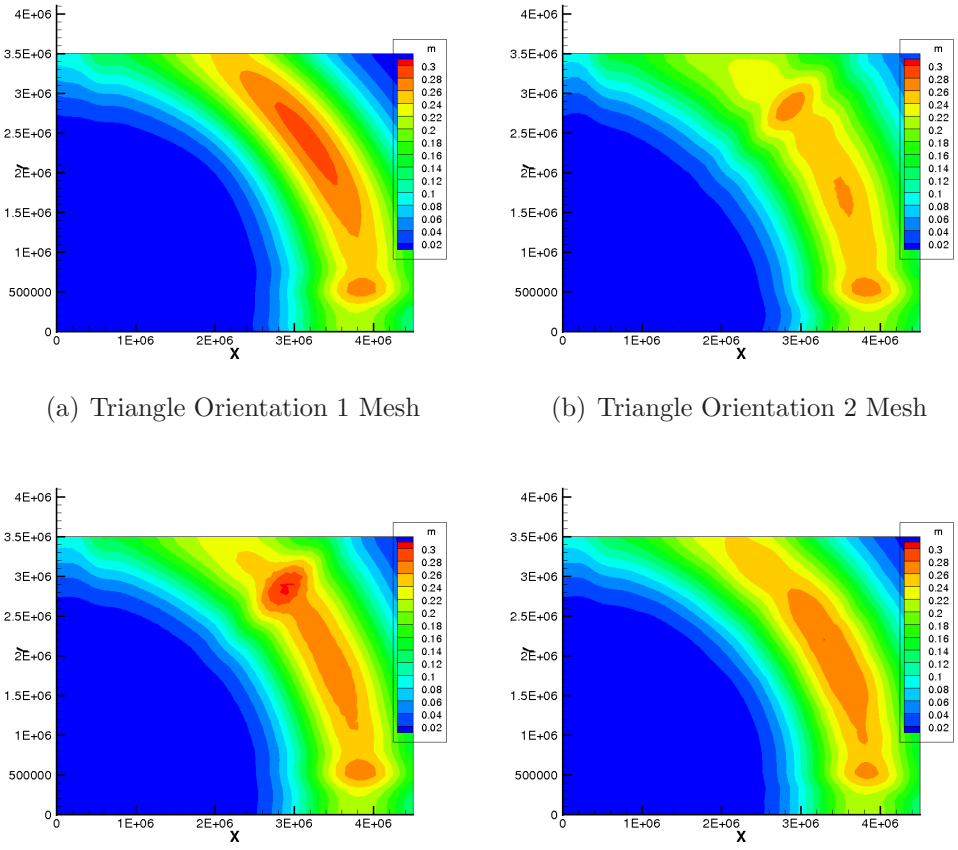

(a) Triangle Orientation 1 Mesh

(b) Triangle Orientation 2 Mesh

(c) Union Jack Mesh

(d) SMS Mesh

Figure 4.19: DG solutions of the significant wave height after 5 days for the GSE test case, which employ constants in geographic space and quadratics in spectral space ($p = 0$, $q = 2$) for each the four geographic meshes in Figure 4.17, are shown.

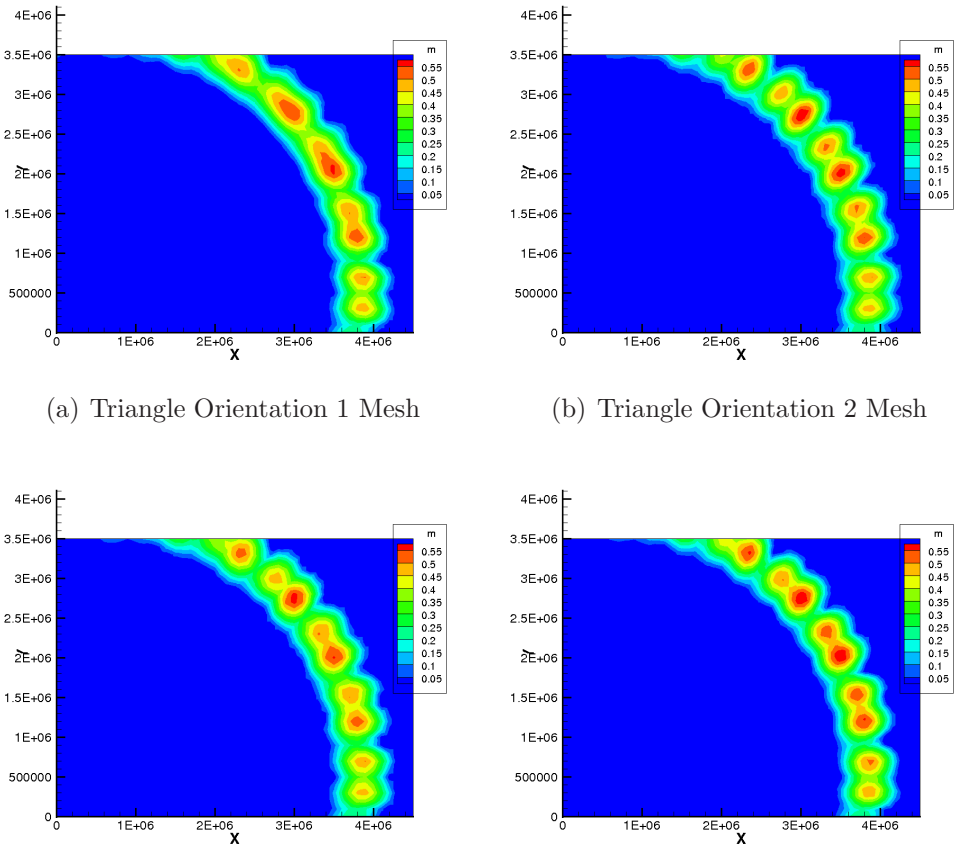

(a) Triangle Orientation 1 Mesh

(b) Triangle Orientation 2 Mesh

(c) Union Jack Mesh

(d) SMS Mesh

Figure 4.20: DG solutions of the significant wave height after 5 days for the GSE test case, which employ linears in both geographic and spectral space $(p, q = 1)$ for each the four geographic meshes in Figure 4.17, are shown.

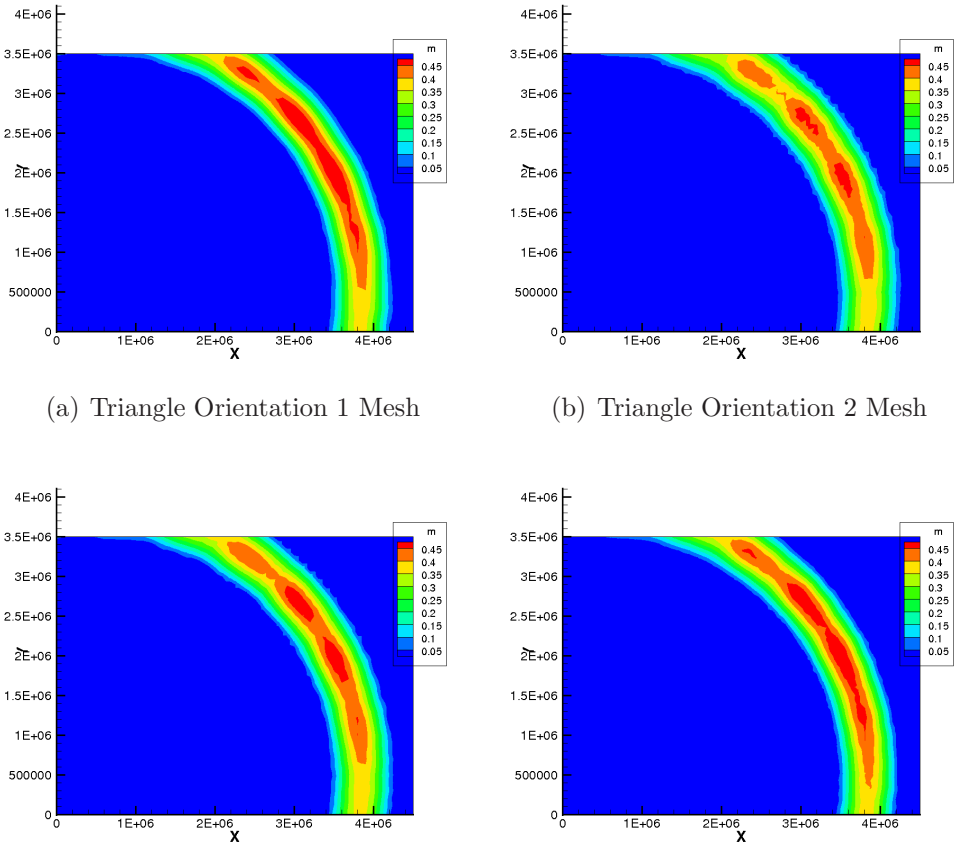

(a) Triangle Orientation 1 Mesh

(b) Triangle Orientation 2 Mesh

(c) Union Jack Mesh

(d) SMS Mesh

Figure 4.21: DG solutions of the significant wave height after 5 days for the GSE test case, which employ linears in geographic space and quartics in spectral space ($p = 1$, $q = 4$) for each the four geographic meshes in Figure 4.17, are shown.

increase resolution through mesh refinement. We have also seen by employing higher order approximations in spectral space in the DG wave model we can alleviate some of the GSE, but this is not an option for SWAN and mesh refinement to alleviate the GSE is not practical in operational settings due to the increased computational expense. Booij and Holthuijsen provide an alternative solution to the GSE in SWAN by adding diffusion terms to the propagation equation [10]. The simplified action balance equation with the GSE correction terms is

$$\frac{\partial N}{\partial t} + \frac{\partial}{\partial x}[c_x N - D_{xx}\frac{\partial N}{\partial x}] + \frac{\partial}{\partial y}[c_y N - D_{yy}\frac{\partial N}{\partial y}] - 2D_{xy}\frac{\partial^2 N}{\partial x \partial y} = 0, \tag{4.1}$$

$$D_{xx} = D_{ss}\cos^2\theta + D_{nn}\sin^2\theta, \tag{4.2}$$

$$D_{yy} = D_{ss}\sin^2\theta + D_{nn}\cos^2\theta, \tag{4.3}$$

$$D_{xy} = (D_{ss} - D_{nn})\cos\theta\sin\theta, \tag{4.4}$$

$$D_{ss} = (\Delta c_g)^2 T_s/12, \tag{4.5}$$

$$D_{nn} = (c_g \Delta\theta)^2 T_s/12, \tag{4.6}$$

where D_{ss} is the diffusion coefficient in the propagation direction of the discrete wave component and D_{nn} is the diffusion coefficient along the crest of the discrete wave component, D_{xx}, D_{yy}, and D_{xy} are the corresponding components of the diffusion tensor along the axes of the spatial grid, c_g is the group velocity, Δc_g is the discrete increment corresponding to the spectral bin, and T_s is the swell age or time elapsed since the generation of the swell [10]. The swell age, T_s is treated as a tunable coefficient. This GSE correction can only be implemented in the structured version of SWAN. Results for the structured

SWAN model are shown in Figure 4.23 with a first order upwind (BSBT) difference scheme in geographic space (a), the higher order Stelling and Leendertse (S&L) [121] scheme in geographic space (b), and the S&L scheme with the GSE correction for $T_s = 2$ days (c) and $T_s = 5$ days (d). We see that SWAN's BSBT solution is more diffusive than the higher order S&L scheme, just as the constant approximation was more diffusive than the higher order geographic solutions for the DG wave model. Higher order geographic approximations, which are less diffusive, increase the GSE, which we see in SWAN and the DG model's solutions. Using $T_s = 2$ days as the wave age, the SWAN solution has less GSE than the S&L solution but has more than the T_s=5 days solution.

By adding diffusion to the equation, SWAN alleviates the GSE in a more computationally efficient way than mesh refinement. In the DG wave model, we can alleviate the GSE by increasing the spectral order of approximation no matter what unstructured mesh is used. Increasing the order of approximation does add computation costs although we can increase the computational efficiency by using adaptivity. In addition to demonstrating the benefits of adaptivity, we also demonstrate the parallel performance of the DG spectral wave model.

The DG spectral wave model runs in parallel in MPI. The parallelization occurs by decomposing the geographic domain over the computational cores. The domain decomposition is also performed in parallel via the ParMETIS Library. We examine the parallel performance of the DG spectral wave model

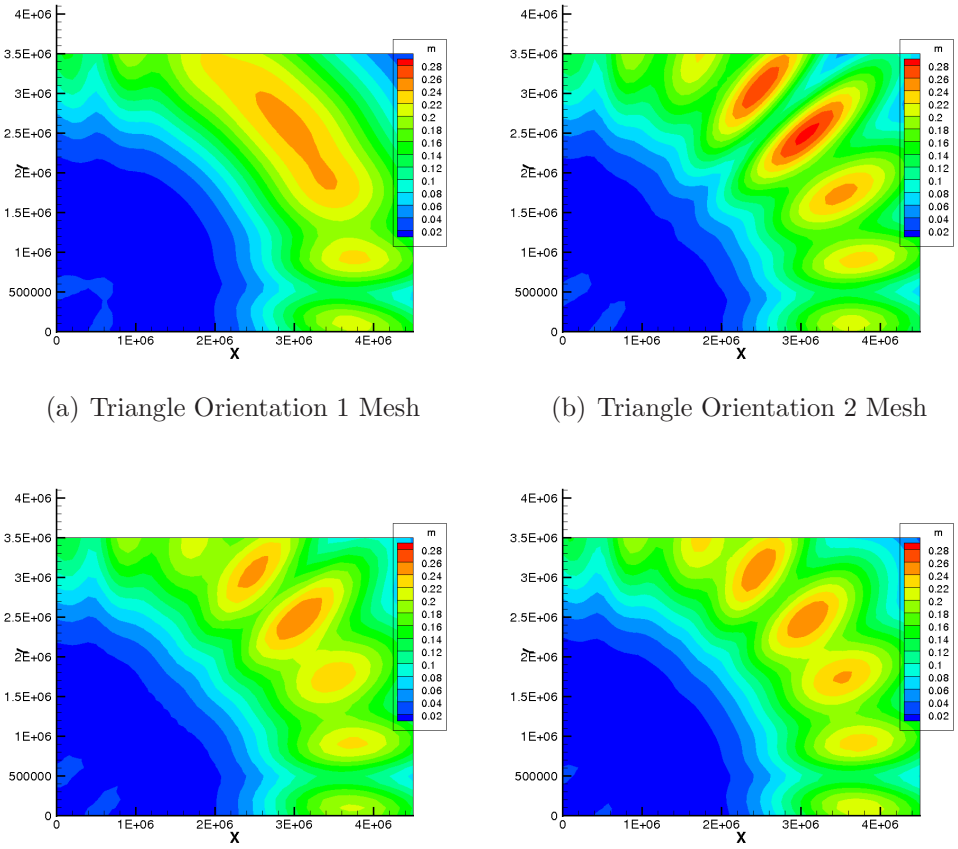

(a) Triangle Orientation 1 Mesh

(b) Triangle Orientation 2 Mesh

(c) Union Jack Mesh

(d) SMS Mesh

Figure 4.22: SWAN solutions of the significant wave height after 5 days for the GSE test case for each the four unstructured, geographic meshes in Figure 4.17 are shown.

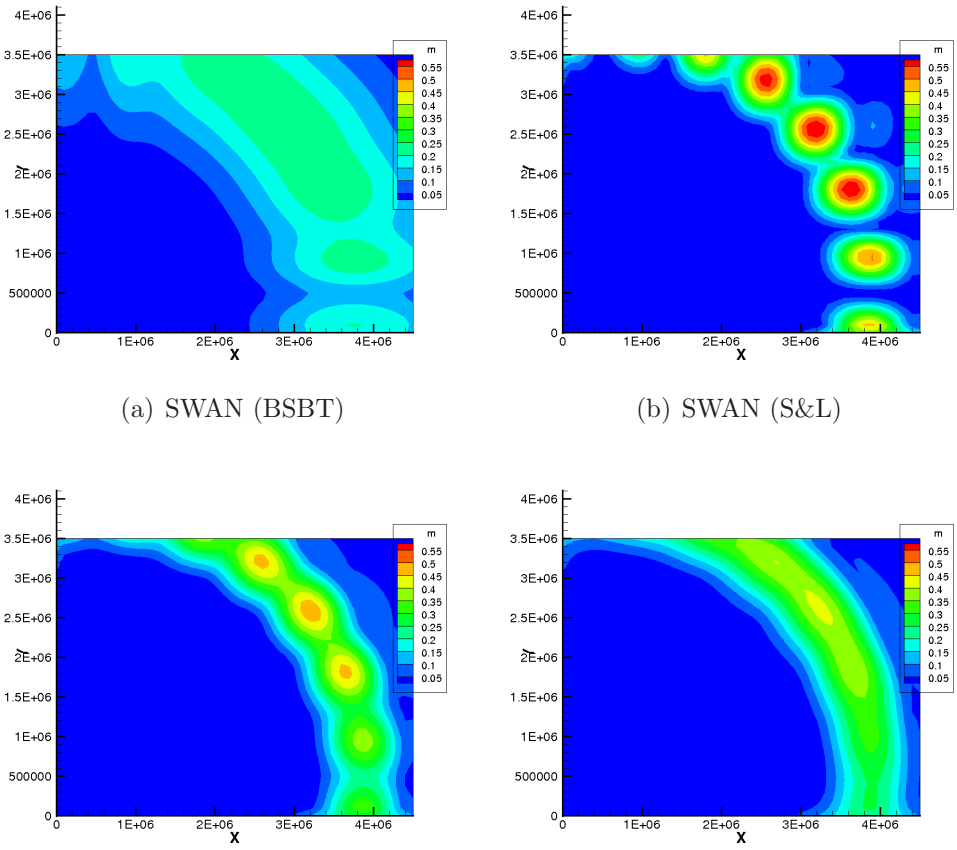

(a) SWAN (BSBT)

(b) SWAN (S&L)

(c) SWAN (GSE Correction T_s=2 days)

(d) SWAN (GSE Correction T_s=5 days)

Figure 4.23: SWAN solutions of the significant wave height for the GSE test case after 5 days using structured geographic meshes using BSBT in (a), the higher order S&L scheme (b), and the S&L scheme with the GSE correction for $T_s = 2$ days (c) and $T_s = 5$ days (d).

on Lonestar, which is a Linux Cluster at the Texas Advanced Computing Center (TACC). Lonestar is composed of 1,888 compute nodes, with two 6-Core processors per node, for a total of 22,656 cores. Lonestar has a theoretical peak performance of 302 TFLOPS, 44 TB of total memory and 276 TB of local disk space. Nodes are connected with an InfiniBand network with a 40 GB/sec bandwidth.

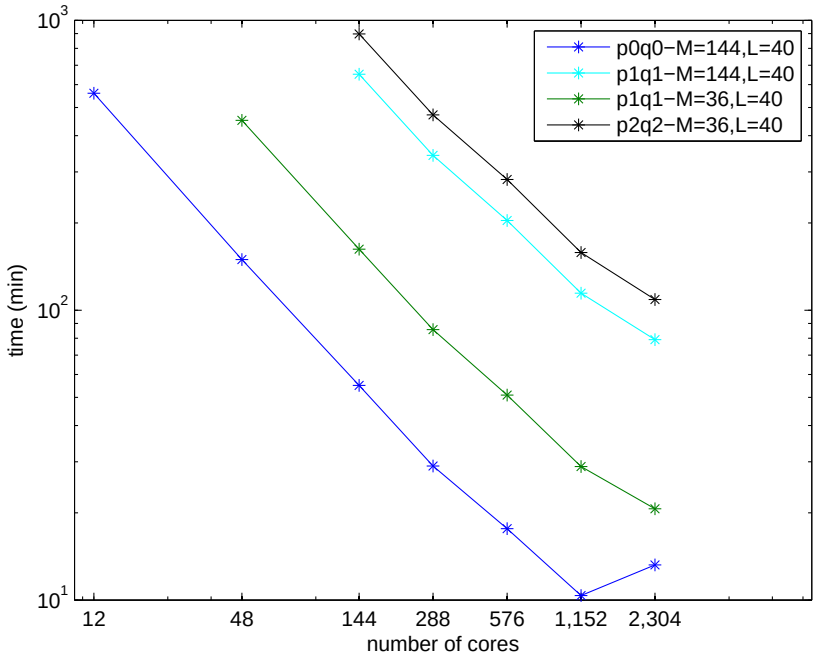

Figure 4.24: Parallel scalability results for the DG spectral wave model on Lonestar. The time shown is wall-clock time for the 5 day GSE simulation using the finescale geographic mesh.

We employ a fine-scale geographic mesh with $h = 25$ km, 58,112 elements and 29,377 verticies. We either use $M = 36$ or 144 directional elements,

corresponding to $\Delta\theta = 10^\circ$ or 2.5°, and $L = 40$ frequency elements. Timings for the 5 days of simulation, with a time step of $\Delta t = 150$s, are shown in Figure 4.24 for several different orders of approximation. We observe that for the constant approximation $(p, q = 0)$ with $M = 144$ directional elements, which has 5,760 degrees of freedom per geographic element, scales up to 1,152 cores. With 2,304 cores, which corresponds to approximately 25 geographic elements per core, the required communication increases the total computation time compared to only using 1,152 cores, which corresponds to approximately 50 geographic elements per core. When the order of approximation is increased to linear approximations in both geographic and spectral space $(p, q = 1)$, we see that the computations scale upto 2,304 cores. There are 51,840 degrees of freedom per geographic element and the increased work per core extends the scalability of the model. However, many realistic computations have larger directional spacings, so we also examine what happens when we use larger directional elements with $\Delta\theta = 10^\circ$ $(M = 36)$. The green line shows the linear approximation $(p, q = 1)$ with $M = 36$ which corresponds to 12,960 degrees of freedom per geographic element. We again see that the computations scale through 2,304 cores as it also does for the quadratic approximation $(p, q = 2)$, which corresponds to 51,840 degrees of freedom per geographic element.

4.4.1 Adaptivity

To show the potential gain in computational efficiency through p-adaptivity we employ a simple adaptive algorithm for the GSE test case. At each time

step for this adaptive scheme, we evaluate the significant wave height at the center of each geographic element. If the significant wave height is greater than or equal to our chosen value of 0.01 m, then we use p_{high} in geographic space and q_{high} for a pre-determined sector of spectral space. We choose *a priori* where the action density lies within the spectrum, and outside of that area q is always q_{low}. Once an element is refined to a higher order with p_{high} and q_{high}, it must maintain this higher order approximation for 15 time steps. Otherwise, if the significant wave height is less than the 0.01 m at the center of the geographic element, we use p_{low} in geographic space and q_{low} for the entire spectral domain.

For this case, we use the geographic mesh shown in Figure 4.17(a) with 36 directional elements and 40 frequency elements. For every geographic element we have 960 spectral elements, but because the wave is propagating towards the east-northeast, the action density will only be in 72 of those elements or 7.5%. For other cases, the action density might lie in a larger portion of the spectral domain, but rarely if ever in the entire spectral domain. In Figures 4.25 and 4.26, the significant wave height and the order of approximation p in geographic space, where blue represents $p = 0$, a constant approximation, and red represents linear approximation, $p = 1$, are shown for four different time steps: $t = 0$ (initial condition), two intermediate time steps of $t = 250$ and $t = 500$, and $t = 720$ (day 5). We see that the adaptive routine uses higher order approximation in the area of interest, where we have non-zero significant wave height, and uses a low order of approximation everywhere else. We ex-

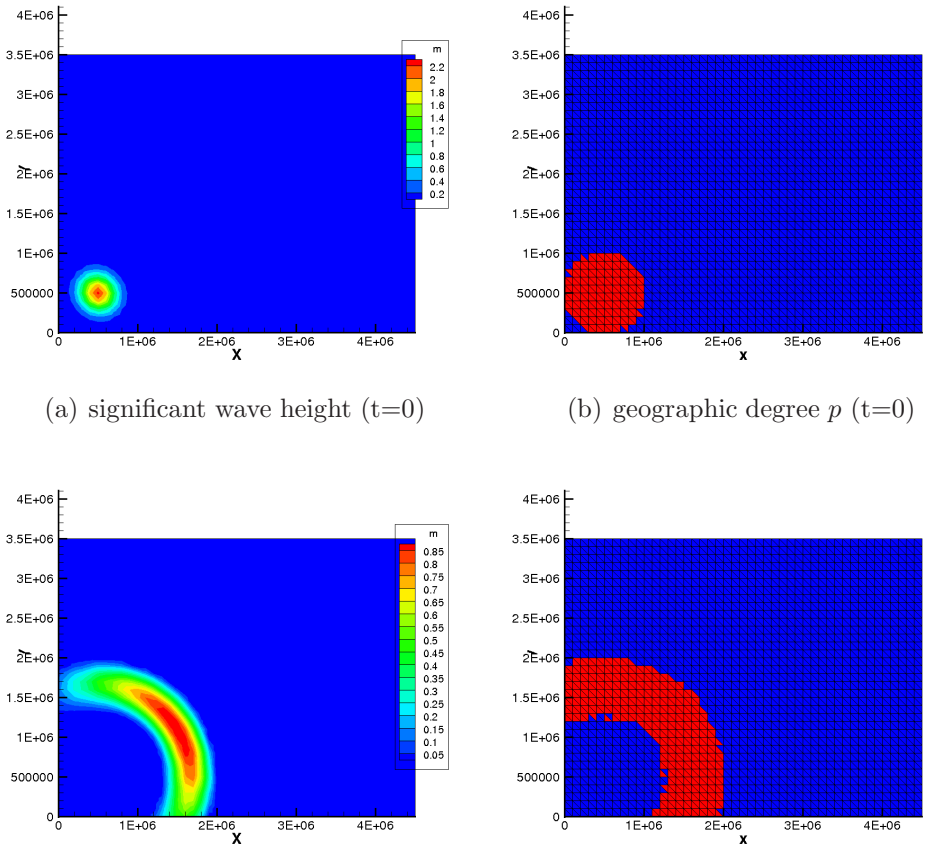

(a) significant wave height (t=0)

(b) geographic degree p (t=0)

(c) significant wave height (t=250)

(d) geographic degree p (t=250)

Figure 4.25: The significant wave height and degree of the geographic element for the initial condition ($t = 0$) and at the time step $t = 250$ for the GSE test case with adaptivity. The higher degree of linear approximation ($p = 1$), represented in red, follows the wave as it propagates through the domain. The areas with no activity have the low, constant order approximation ($p = 0$), which is represented in blue.

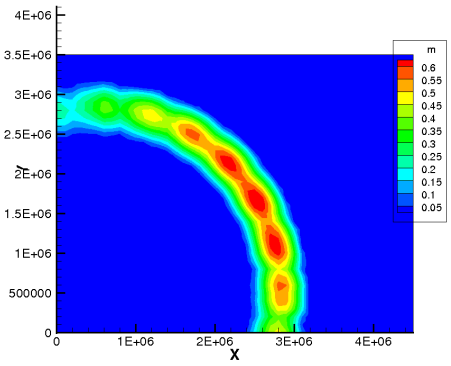

(a) significant wave height (t=500)

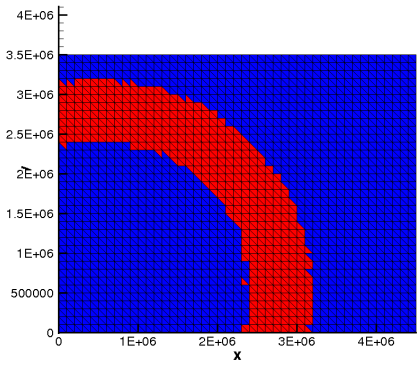

(b) geographic degree p (t=500)

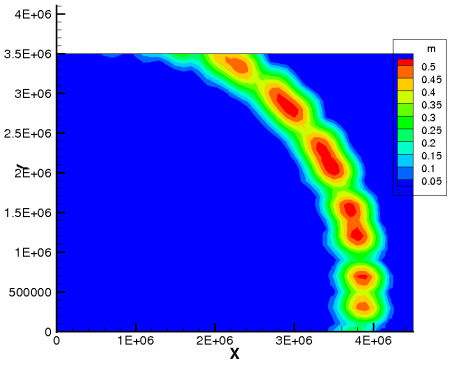

(c) significant wave height (t=720)

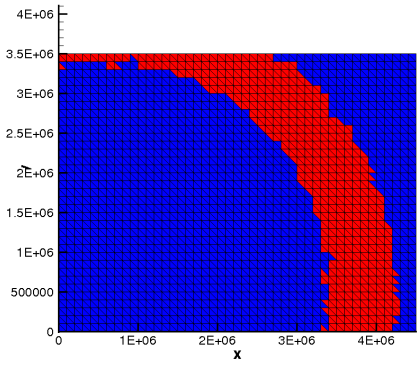

(d) geographic degree p (t=720)

Figure 4.26: The significant wave height and degree of the geographic element for the time step $t = 500$ and at the final time of 5 days ($t = 720$) for the GSE test case with adaptivity. The higher degree of linear approximation ($p = 1$), represented in red, follows the wave as it propagates through the domain. The areas with no activity have the low, constant order approximation ($p = 0$), which is represented in blue.

amine the error between using the higher order approximation everywhere and using the adaptive routine for four different cases at the final time of 5 days ($t = 720$). In Figure 4.27, we show the difference in significant wave height between the adaptive and non-adaptive solutions and in Figure 4.28, we show the percentage error in the significant wave height reference to the maximum significant wave height when using adaptivity. When using constant approximation in geographic space and only adapting in spectral space, we have very small errors up to 0.2% in a few places. When we adapt in geographic space, as well as in spectral space using either linears or quadratics for our higher order approximation, we obtain errors up to 4.5 cm or 8.5-9% error at a few locations along the interface of the lower and higher order approximations in geographic space, but otherwise obtain the same solution as when using a higher order approximation throughout the entire domain.

Table 4.4 shows the time for the 5 day simulations with and without adaptivity. By adapting in spectral space and using constant approximation in geographic space, we obtain a speed up of ≈2.8 or 5.7 if $q_{high} = 1$ or 2, respectively ($q_{low} = 0$). Compared to the time for a constant approximation everywhere, it only takes 1.1 or 1.4 times longer to obtain a higher order solution using adaptivity, versus 3.1 or 7.8 times longer if using higher order approximations everywhere for $q_{high} = 1$ or 2, respectively. When adapting and using higher order, linear approximations in geographic space ($p_{low} = 0$, $p_{high} = 1$) as well as adapting spectral space, we obtain a speed up of approximately 7.6 or 15.0 if $q_{high} = 1$ or 2, respectively ($q_{low} = 0$). Compared

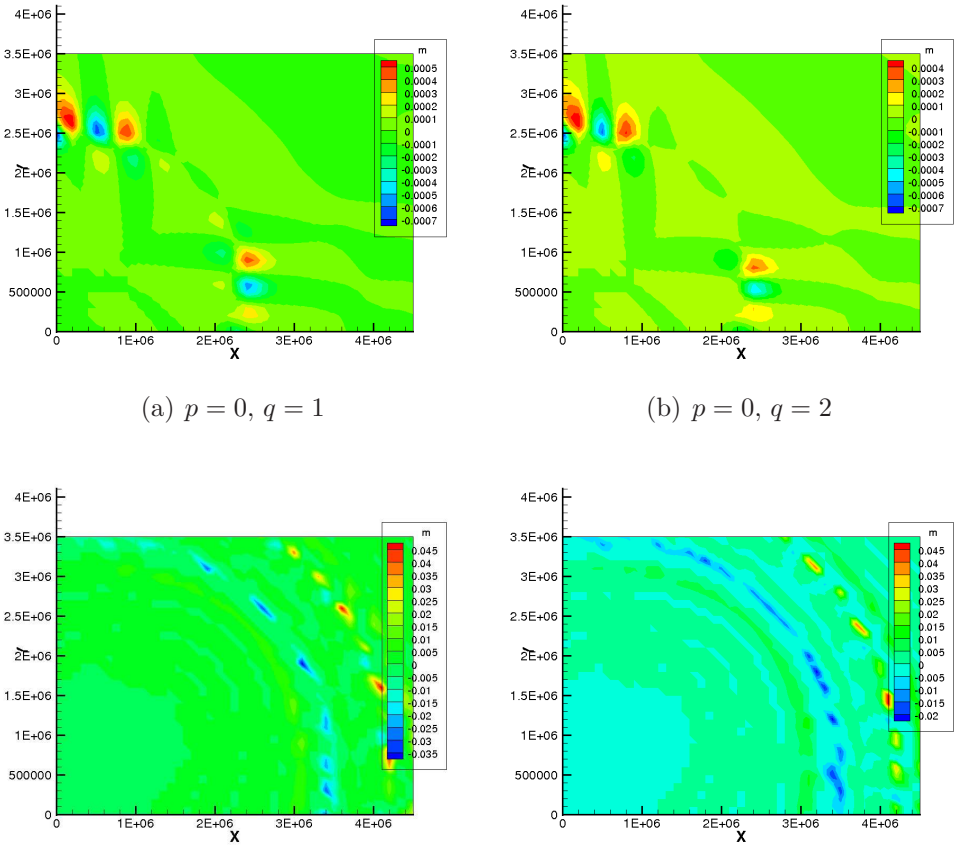

(a) $p = 0$, $q = 1$

(b) $p = 0$, $q = 2$

(c) $p = 1$, $q = 1$

(d) $p = 1$, $q = 2$

Figure 4.27: The difference in significant wave height between using a higher-order approximation (p, q) throughout the entire geographic and spectral domain and the adaptive solution ($p_{low}, q_{low} = 0$, $p_{high} = p$, $q_{high} = q$) at day 5 for the GSE test case.

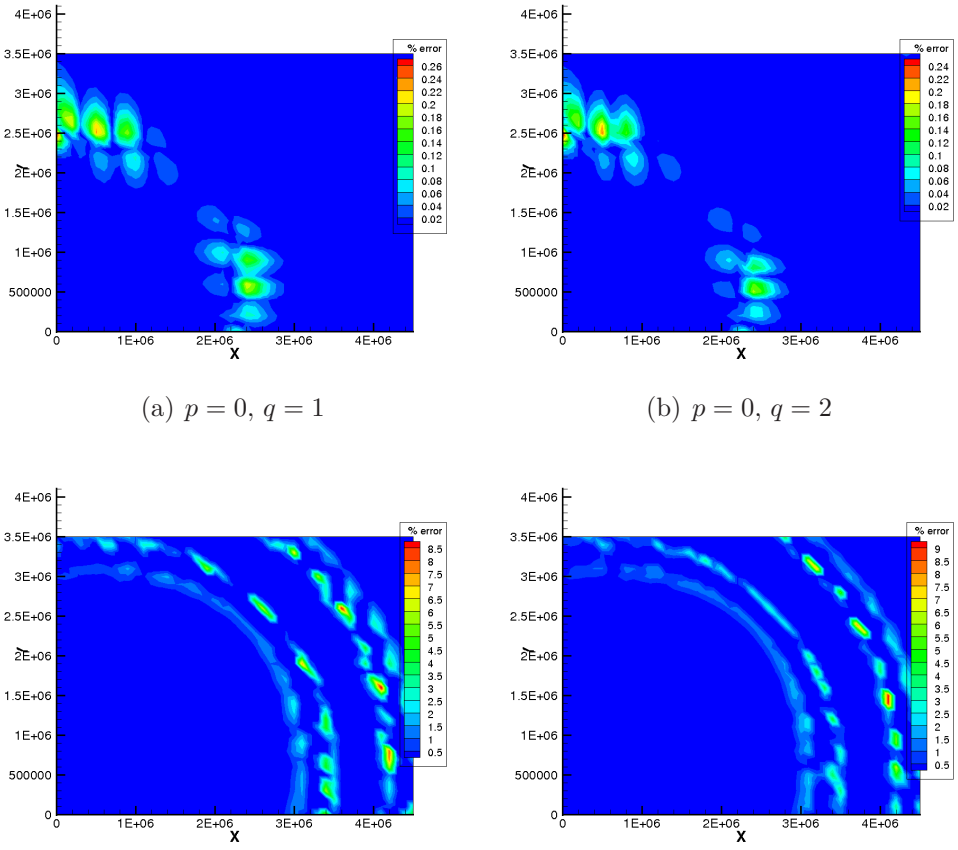

(a) $p = 0$, $q = 1$

(b) $p = 0$, $q = 2$

(c) $p = 1$, $q = 1$

(d) $p = 1$, $q = 2$

Figure 4.28: The percentage error relative to the maximum significant wave height for the adaptive solutions ($p_{low}, q_{low} = 0$, $p_{high} = p$, $q_{high} = q$) at 5 days for the GSE test case. When calculating the error, we considered the 'exact' solution to be the DG solution using the higher-order approximation (p, q) everywhere.

	time (min)
$p = 0$, $q = 0$	16.82
$p = 0$, $q = 1$	51.96
$p = 0$, $q = 2$	131.42
$p = 1$, $q = 0$	49.87
$p = 1$, $q = 1$	216.18
$p = 1$, $q = 2$	590.50
with adaptivity	time (min)
$p_{high} = 0$, $q_{high} = 1$	18.55
$p_{high} = 0$, $q_{high} = 2$	23.26
$p_{high} = 1$, $q_{high} = 1$	28.40
$p_{high} = 1$, $q_{high} = 2$	39.34
	time (min)
SWAN	4.68

Table 4.4: Timings for 5 days of the GSE test case with and without adaptivity for the DG model with different orders of approximation as well as SWAN. For the adaptive solutions, $p_{low}, q_{low} = 0$ for all cases.

to the time for a constant approximation everywhere, it only takes 1.7 or 2.3 times longer to obtain a higher order solution using adaptivity, versus 12.9 or 35.1 times longer if using higher order approximations everywhere for $q_{high} = 1$ or 2, respectively. Although this particular adaptive routine will not be applicable to every scenario, it still illustrates the incredible computational savings achieved by implementing adaptivity while still maintaining higher order accurate solutions. SWAN is still 3.6 times faster than the constant order approximation of the DG model. However, through further optimization, we believe this time gap can be significantly reduced.

4.5 Concluding Remarks

We have verified and validated the DG spectral wave model with manufactured solutions, analytic test cases, and other standard test cases. We experimentally obtained the optimal convergence rate of $p+1$ for manufactured solutions for $p = q$, and h small. For both the current- and depth-induced shoaling and refraction test cases, we used linear approximations and accurately modeled the analytic solutions of the significant wave height and the main wave direction. In addition, for the opposing current case, we showed that we obtain a more accurate solution by employing a higher-order approximation on a coarse mesh versus a low-order approximation on a fine mesh with twice the degrees of freedom. We also showed that higher order approximations in spectral space can alleviate the Garden Sprinkler effect.

A commonly cited drawback of the DG method is the increased num-

ber of degrees of freedom, which leads to increased computational costs. We showed that adaptivity can dramatically reduce the computational time while maintaining the higher-order accuracy. We also showed that the DG wave model is highly scalable, especially when using higher order approximations.

Chapter 5

Coupled Wave/Circulation Model

In this chapter, we discuss the coupling of the DG spectral wave model to the DG Shallow Water Model (DG-SWEM). We introduce the circulation model and verify and validate the DG wave/circulation model.

Waves and circulation processes interact in daily wind and tide driven flows and in more extreme events such as hurricanes. Currents and water levels affect wave propagation and the location of wave-breaking zones, while the wave forces induce setup and currents. Despite this interaction, waves and circulation processes are modeled separately using different approaches. Circulation processes are represented by the shallow water equations, which conserve mass and momentum. However, this approach for wind-generated waves is impractical for large geographic scales and therefore we take a spectral approach, which represents waves by the action balance equation, as outlined in the previous chapters. Fukashimo (2008) and Dietrich *et al.* (2010) showed that coupling wave and circulation in hindcasts of hurricanes increases water levels by 5%-20% in regions of broad shelf and up to 35% in regions of steep slope [37,52], which highlights the importance of coupling wave and circulation models.

SWAN+ADCIRC is an existing, tightly-coupled wave/circulation model, that couples the widely-used Simulating WAves Nearshore (SWAN) [11] spectral wave model with the ADvanced CIRCulation model (ADCIRC) [89], a widely-used circulation model. SWAN was recently extended to run on unstructured meshes [140] and the SWAN+ADCIRC model utilizes this new capability by employing the same unstructured mesh for each of the models. This eliminates interpolation error that can occur if two different meshes are used, and it allows representation of a variety of scales, which are required to represent the complex coastal regions. The coupled model is run as the same executable and information is passed directly through local memory. SWAN+ADCIRC has successfully been used for hindcasting recent hurricanes in the Gulf of Mexico [38, 39, 41].

ADCIRC employs a continuous-Galerkin (CG) finite-element method, which is limited to linear approximations, has difficulties handling strong advection and is not locally mass conservative [32]. Recent efforts have extended ADCIRC to use a discontinuous-Galerkin (DG) method; this DG circulation model, DG-SWEM, can employ higher-order approximations and can handle advection-dominated flows [78]. In addition, DG models are locally and globally conservative, which can be important when coupling to transport equations [31, 36]. For comparison purposes herein, DG-SWEM has been coupled tightly with SWAN, in a manner similar to [41], which allows both models to run as the same executable program, and on the same unstructured mesh. However, the finite-difference solution method in SWAN requires information

at the vertices, so high-order information from DG-SWEM is lost in the coupling.

We couple our discontinuous Galerkin spectral wave model with DG-SWEM. The resulting coupled DG wave/circulation model executes on the same unstructured mesh and higher-order information can be passed between the models. Waves and currents can be passed from the circulation model to the spectral wave model, and the wave model can pass wave radiation stress gradients to the circulation model.

This chapter is organized as follows, we first describe the circulation model DG-SWEM used in the coupled DG wave/circulation model. We then examine a test case to verify and validate the DG coupled wave/circulation model through comparisons with DG-SWEM coupled with SWAN. Because the DG-SWEM is mature, no comparisons will be made to ADCIRC(CG). Comparisons can be found in [77].

5.1 The Circulation Model

Shallow water equations are used to model flow processes such as tides, river flows, tsunami waves and storm surges. We utilize the shallow water equations to model the circulation processes in the coupled wave/circulation model. In particular, the Discontinuous Galerkin Shallow Water Equation Model (DG-SWEM) in [2], [15], [76], [77], [78] will be employed as the circulation model in the coupled discontinuous Galerkin wave/circulation model. In this section, we state the governing equations and discuss the Local Discon-

tinuous Galerkin (LDG) method used to discretize the system. Details of its implementation can be found in [75].

5.1.1 Shallow Water Equations

For the coupled model, we will employ the depth-integrated shallow water equations to model circulation. The shallow water equations consist of the primitive continuity equation, which represents the conservation of mass

$$\frac{\partial \xi}{\partial t} + \frac{\partial}{\partial x}(Hu) + \frac{\partial}{\partial y}(Hv) = 0, \tag{5.1}$$

and the equations representing conservation of momentum in conservative form

$$\begin{aligned}
&\frac{\partial}{\partial t}(uH) + \frac{\partial}{\partial x}\left(Hu^2 + \frac{1}{2}gH^2\right) + \frac{\partial}{\partial y}(Huv) - gH\frac{\partial h_b}{\partial x} - \nu\Delta(Hu) \\
&\qquad = -\tau_{bf}Hu - \rho^{-1}\left(H\frac{\partial P}{\partial x} - \tau_{wind,x} - \tau_{sx,waves}\right), \qquad (5.2)\\
&\frac{\partial}{\partial t}(vH) + \frac{\partial}{\partial x}(Huv) + \frac{\partial}{\partial y}\left(Hv^2 + \frac{1}{2}gH^2\right) - gH\frac{\partial h_b}{\partial y} - \nu\Delta(Hv) \\
&\qquad = -\tau_{bf}Hv - \rho^{-1}\left(H\frac{\partial P}{\partial y} - \tau_{wind,y} - \tau_{sy,waves}\right). \qquad (5.3)
\end{aligned}$$

Here ξ is the elevation of the free surface from the geoid, $H = \xi + h_b$ is the total height of the water column where h_b is the depth of the water below the geoid (bathymetry), (u, v) is the depth-averaged horizontal velocity, g is the gravitational acceleration, ν is the depth-averaged horizontal eddy viscosity, P is the atmospheric pressure, ρ is the density of water, τ_{bf} is the bottom friction, τ_{wind} is the wind stress at the sea surface, and τ_{waves} is the radiation stress gradients at the sea surface caused by wind-waves. The radiation stress

gradients are

$$\tau_{sx,waves} = -\frac{\partial S_{xx}}{\partial x} - \frac{\partial S_{xy}}{\partial y}, \tag{5.4}$$

$$\tau_{sy,waves} = -\frac{\partial S_{xy}}{\partial x} - \frac{\partial S_{yy}}{\partial y}, \tag{5.5}$$

where S_{xx}, S_{yy} and S_{xy} are the radiation stresses [88]:

$$S_{xx} = \rho g \int\int ((n\cos^2\theta + n - \frac{1}{2})\sigma N) d\sigma d\theta, \tag{5.6}$$

$$S_{xy} = S_{yx} = \rho g \int\int (n\sin\theta\cos\theta\sigma N) d\sigma d\theta, \tag{5.7}$$

$$S_{yy} = \rho g \int\int ((n\sin^2\theta + n - \frac{1}{2})\sigma N) d\sigma d\theta. \tag{5.8}$$

The radiation stress gradient is an input parameter provided by the DG spectral wave model in the coupled model.

For later use, we write the shallow water equations ((5.1)-(5.3)) in divergence form:

$$\frac{\partial \mathbf{c}}{\partial t} + \nabla \cdot (\mathbf{A} - D\nabla \mathbf{c}) = \mathbf{h}(\mathbf{c}) \tag{5.9}$$

where

$$\mathbf{c} = \begin{pmatrix} \xi \\ uH \\ vH \end{pmatrix},$$

$$\mathbf{A} = \begin{pmatrix} uH & vH \\ u^2H + \frac{1}{2}g(H^2 - h_b^2) & uvH \\ uvH & v^2H + \frac{1}{2}g(H^2 - h_b^2) \end{pmatrix},$$

$$D = \begin{bmatrix} \mathbf{0} & \mathbf{0} & \mathbf{0} \\ \mathbf{0} & \nu\mathbf{I} & \mathbf{0} \\ \mathbf{0} & \mathbf{0} & \nu\mathbf{I} \end{bmatrix},$$

and

$$\mathbf{h}(\mathbf{c}) = \begin{pmatrix} 0 \\ -\tau_{bf} H u - \rho^{-1} \left(H \frac{\partial P}{\partial x} - \tau_{wind,x} - \tau_{sx,waves} \right) + g\xi \frac{\partial h_b}{\partial x} \\ -\tau_{bf} H v - \rho^{-1} \left(H \frac{\partial P}{\partial y} - \tau_{wind,y} - \tau_{sy,waves} \right) + g\xi \frac{\partial h_b}{\partial y} \end{pmatrix}.$$

The matrix D has a block structure where $\mathbf{0}$ is the 2×2 zero matrix and $\mathbf{I}$ is the 2×2 identity matrix.

The shallow water equations are solved on the geographic domain Ξ with appropriate initial and boundary conditions. Two types of boundary conditions are land boundaries where:

$$\mathbf{u} \cdot \mathbf{n} = \mathbf{0},$$

and open ocean boundaries where:

$$\begin{aligned} \xi &= \xi_{tidal}, \\ \nu \nabla (uH) \cdot \mathbf{n} &= 0, \\ \nu \nabla (vH) \cdot \mathbf{n} &= 0, \end{aligned}$$

where ξ_{tidal} is a specified surface elevation and $\mathbf{n}$ is the outward normal of $\partial\Xi$, the boundary of Ξ.

5.1.2 Local Discontinuous Galerkin Method

The Local Discontinuous Galerkin method was first introduced and analyzed for convection-diffusion problems by Cockburn and Shu [27] and modified by Cockburn and Dawson in [21]. The LDG method was applied to the shallow water equations by Aizinger and Dawson in [2] and is repeated here.

We first introduce some necessary notation. We define $\{\mathcal{T}_h\}_{h>0}$ as a family of finite element partitions of Ξ such that no element Ξ_g cross the boundary of Ξ, where h is the maximum element diameter. We define the approximation space

$$V_h = \{\mathbf{v} : \text{each component of } \mathbf{v} \text{ is in } M_h\}$$

where

$$M_h = \{w \in L^2(\Xi) : w|_{\Xi_g} = \phi|_{\Xi_g} \in P^p(\Xi_g) \quad \forall \Xi_g\}.$$

We do not specify the number of components of $\mathbf{v}$ and in the definitions below and we allow the number to vary depending of the variable being approximated. We denote $\mathbf{n_g}$ to be the unit outward normal to $\partial\Xi_g$, the boundary of Ξ_g. Then for $\mathbf{x} \in \partial\Xi_g$ we define the interior

$$\mathbf{v}^{int}(\mathbf{x}) = \lim_{s \to {}^0-} \mathbf{v}(\mathbf{x} + s\mathbf{n_g})$$

and exterior

$$\mathbf{v}^{ext}(\mathbf{x}) = \lim_{s \to {}^0+} \mathbf{v}(\mathbf{x} + s\mathbf{n_g})$$

traces. Their average is defined as

$$\overline{\mathbf{v}} = (\mathbf{v}^{int} + \mathbf{v}^{ext})/2.$$

The LDG method is based on a mixed form of (5.9) with auxiliary variables $\tilde{\mathbf{z}}$ and $\mathbf{z}$, defined

$$\tilde{\mathbf{z}} = -\nabla \mathbf{c}, \tag{5.10}$$

$$\mathbf{z} = D\tilde{\mathbf{z}}. \tag{5.11}$$

We substitute $\mathbf{z}$ into (5.9), multiply by a sufficiently smooth test function $\mathbf{v}$ and integrating over an element Ξ_g and obtain

$$\left(\frac{\partial \mathbf{c}}{\partial t}, \mathbf{v}\right)_{\Xi_g} - (\mathbf{A} + \mathbf{z}, \nabla \cdot \mathbf{v})_{\Xi_g} + \langle (\mathbf{A} + \mathbf{z}) \cdot \mathbf{n}_g, \mathbf{v}^{int} \rangle_{\partial \Xi_g} = (\mathbf{h}(\mathbf{c}), \mathbf{v})_{\Xi_g}. \tag{5.12}$$

Then, we multiply (5.10) by a test function $\tilde{\mathbf{v}}$ and integrate over Ξ_g to obtain

$$(\tilde{\mathbf{z}}, \tilde{\mathbf{v}})_{\Xi_g} - (\mathbf{c}, \nabla \cdot \tilde{\mathbf{v}})_{\Xi_g} + \langle \mathbf{c}, \tilde{\mathbf{v}}^{int} \cdot \mathbf{n}_g \rangle_{\partial \Xi_g} = 0, \tag{5.13}$$

and multiply (5.11) by a test function $\mathbf{v}$ and find

$$(\mathbf{z}, \mathbf{v})_{\Xi_g} - (D\tilde{\mathbf{z}}, \mathbf{v})_{\Xi_g} = 0. \tag{5.14}$$

We approximate $\mathbf{c}$, $\tilde{\mathbf{z}}$ and $\mathbf{z}$ by $\mathbf{C}$, $\tilde{\mathbf{Z}}$ and $\mathbf{Z}$ in V_h. On the boundary Ξ_g, we approximate $\mathbf{A} \cdot \mathbf{n_g}$ by a numerical flux $\hat{\mathbf{A}}(\mathbf{C}^{int}, \mathbf{C}^{ext}; \mathbf{n_g})$ and on all other boundary terms are approximated by averaging. The discrete weak form is then

$$\begin{aligned}
&\left(\frac{\partial \mathbf{C}}{\partial t}, \mathbf{v}\right)_{\Xi_g} - (\mathbf{A}(\mathbf{C}) + \mathbf{Z}, \nabla \cdot \mathbf{v})_{\Xi_g} \\
&\quad + \langle \hat{\mathbf{A}}(\mathbf{C}^{int}, \mathbf{C}^{ext}; \mathbf{n}_g) + \overline{\mathbf{Z}}) \cdot \mathbf{n}_g, \mathbf{v}^{int} \rangle_{\partial \Xi_g} \\
&\qquad = (\mathbf{h}(\mathbf{C}), \mathbf{v})_{\Xi_g}, \mathbf{v} \in W_{h,g},
\end{aligned} \tag{5.15}$$

$$(\tilde{\mathbf{Z}}, \tilde{\mathbf{v}})_{\Xi_g} - (\mathbf{C}, \nabla \cdot \tilde{\mathbf{v}})_{\Xi_g} + \langle \overline{\mathbf{C}}, \tilde{\mathbf{v}}^{int} \cdot \mathbf{n}_g \rangle_{\partial \Xi_g} = 0, \tilde{\mathbf{v}} \in V_h, \tag{5.16}$$

$$(\mathbf{Z}, \mathbf{v})_{\Xi_g} - (D\tilde{\mathbf{Z}}, \mathbf{v})_{\Xi_g} = 0, \mathbf{v} \in V_h. \tag{5.17}$$

We note that the numerical flux $\hat{\mathbf{A}}$ can be any locally Lipschitz, conservative, consistent, entopy flux and explicit Runge-Kutta methods are used for time-

stepping. Implementation details for DG-SWEM can be found in the following [2, 15, 75–78].

5.2 Verification and Validation of the Coupled Wave/ Circulation Model

5.2.1 Near-Circular Shoal

To verify the coupled DG wave/circulation model, we examine waves refracting over a circular shoal, as seen in Figure 5.1, in the presence of a current. This test problem is similar to a test problem on structured meshes from Rogers *et. al.* [116] and Dietrich *et. al.* [40]. The source terms are neglected. At the north, south, and west boundaries, an incoming wave is prescribed by a JONSWAP (with peak enhancement factor $\gamma = 3$) spectrum with a significant wave height of 0.5 m, a peak period of 15.2 s, and a main direction of 335° with a $\cos^{14}(\theta)$ directional distribution (i.e., directional spreading is 15°). Incoming and outgoing fluxes are specified in DG-SWEM so that a current of 0.1 m/s flows from west to east. The geographic mesh with $h \approx 3,000$ m is shown in Figure 5.1. The spectral domain has a directional spacing of $\Delta\theta = 10°$ with 33 logarithmically distributed frequency elements that range from 0.05 Hz to 1.0 Hz.

The DG wave/circulation model is coupled loosely through external files. First, the circulation model is run, and it creates output files of the water levels and currents at every 600 s. These files are then used as input to the spectral wave model, which in turn outputs the radiation stresses every

600 s. These radiation stress files are then used as forcing in a new simulation of the circulation model. This process is repeated until there is no change in the output quantities.

For comparison purposes, we compare the loosely-coupled DG wave/ circulation models with a tight coupling of DG-SWEM with SWAN. This tight coupling mimics the coupling of SWAN+ADCIRC as described in [40], so that the models run as the same executable on the same unstructured mesh, and information is passed through local memory without the need for interpolation. So DG-SWEM is either coupled loosely with the DG wave model, or tightly with SWAN. For both coupling paradigms, the inter-model communication occurs every 600s. DG-SWEM uses a time step of 1 s, the DG spectral wave model uses a time step of 20 s and SWAN uses a time step of 600 s.

In Figure 5.2, we show two DG coupled model solutions, one which uses constants (a) and another that uses linears (b) in the wave model in geographic space. Both use linear approximations in spectral space. Also shown in Figure 5.2 are two SWAN+DG-SWEM solutions: the first is the solution on the original mesh (c) and the second is a fine grid "exact" solution (d). For the SWAN+DG-SWEM solution, we observe in Figure 5.2 (c) that the waves refract prematurely when the shoal is represented on the original mesh. This is similar to the behavior observed in a test case without currents on structured meshes in [40], in which the authors showed that either refinement of the mesh or a limiter is needed to prevent the early refraction of the waves. The DG coupled model does not have premature refraction; however, the

constant approximation (a) is too diffusive and linear approximations need to be used. The linear approximation (c) does qualitatively match the fine grid solution (d), again showing the benefit of higher orders in the DG method.

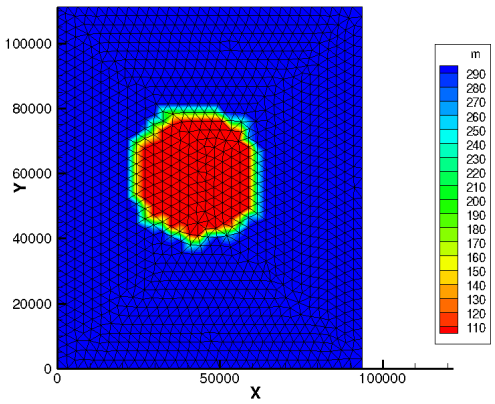

Figure 5.1: The bathymetry and geographic mesh for the circular shoal case.

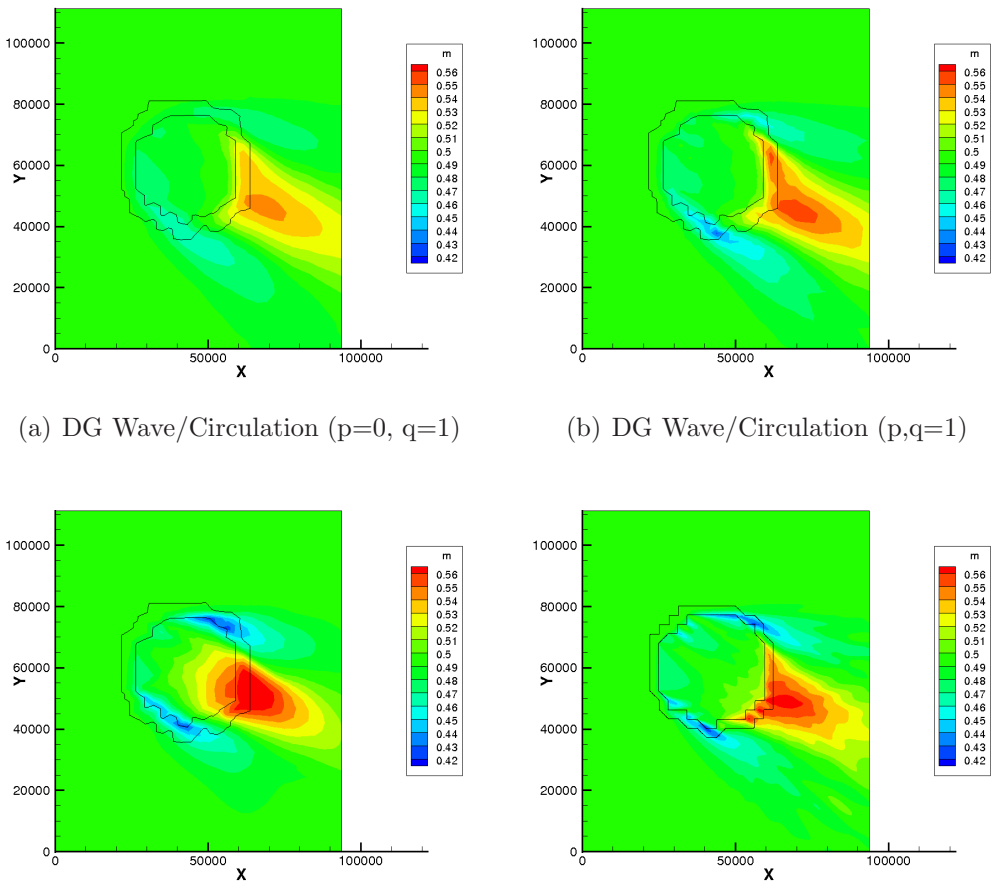

(a) DG Wave/Circulation (p=0, q=1)

(b) DG Wave/Circulation (p,q=1)

(c) SWAN+DG-SWEM

(d) SWAN+DG-SWEM fine grid

Figure 5.2: The DG wave/circulation model results for the circular shoal are shown with constant (a) or linear (b) approximations in geographic space and linear approximations in spectral space in the wave model. SWAN's results tightly-coupled to DG-SWEM are shown on the original mesh (c) and a fine mesh (d), which we consider 'truth'. The black line indicates the 110 m and 290 m contours of the bathymetry.

Chapter 6

An *a Priori* Error Estimate

We perform an *a priori* error estimate for the coupled wave/circulation model. Previously, Dawson, Proft and Aizinger analyzed discontinuous Galerkin and coupled continuous/discontinuous Galerkin methods for the shallow water equations in [1, 2, 33–35]. Mirabito, Dawson, and Aizinger analyzed the local discontinuous Galerkin method for the coupled shallow water and morphodynamic flow system [97]. Dawson and Proft proved an *a priori* error estimate for a coupled continuous/discontinuous Galerkin method for the shallow water equations [35]. For the discontinuous portion of their analysis, Dawson and Proft handled the diffusion operator by implementing the nonsymmetric Oden-Babuška-Baumann formulation [104] and the related interior penalty method (NIPG) introduced by Girault, Rivière and Wheeler in [115]. For the advection terms, they employed the upwinding technique of Lasaint and Raviart [81]. Their work is similar to the previous work of Girault, Rivière and Wheeler who applied the technique of considering the NIPG method for diffusion and Lasaint and Raviart upwinding for advection in their proofs of *a priori* error estimates for the incompressible Stokes and Navier-Stokes equations. We will extensively use the strategies and techniques utilized by Dawson in Proft in the discontinuous portions of their analysis while investigating the

coupled wave/circulation model, which has not been previously analyzed for any numerical scheme.

This chapter is organized as follows. In the following section we present the governing equations of the coupled wave/circulation model as well as some necessary notations and definitions. We continue in Section 6.2 by formulating the weak form, defining the approximation spaces, and formulating the discrete weak form of the coupled model. In Section 6.3, we form the error equations which are necessary for performing the *a priori* error estimate presented in Section 6.4.

6.1 Governing Equations

The coupled wave/circulation model consists of the shallow water equations, which describe the circulation processes, and the action balance equation, which describes waves in a statistical sense. We simplify the error analysis that follows by considering the geographic domain to be only one-dimensional; however, all arguments in the analysis are valid in two-dimensions. We consider the coupled model on the domain Ω, which is a tensor product of the geographic domain, $\Xi \in \mathbb{R}$, and the spectral domain, $\kappa = (\sigma, \theta) \in \mathbb{R}^2$ where σ, $0 < \sigma \leq \sigma_{\max}$, is the relative frequency, which is the frequency observed in a frame of reference moving with the current, and θ is the wave direction, so $\Omega = \Xi \times \kappa \in \mathbb{R} \times \mathbb{R}^2$, for time $t > 0$. We denote the boundary of the domain as $\partial\Omega$ with outward normal $\mathbf{n} = (n_x, n_\sigma, n_\theta)$ and denote the boundary of the geographic domain as $\partial\Xi$ with outward normal n_x. The one-dimensional cou-

pled wave/circulation system for which we perform the error analysis consists of the continuity equation [35]

$$\xi_t + \nabla_x \cdot (uH) = 0, \tag{6.1}$$

the non-conservative form of the momentum equation

$$u_t + u \cdot \nabla_x u + g\nabla_x \xi - \mu \Delta u = F_x, \tag{6.2}$$

and the action balance equation [11]

$$N_t + \nabla \cdot \mathbf{c}N = \frac{S}{\sigma}, \tag{6.3}$$

where $\nabla_* = \frac{\partial}{\partial *}$ and $\nabla = (\frac{\partial}{\partial x}, \frac{\partial}{\partial \sigma}, \frac{\partial}{\partial \theta})$. The unknown variables are ξ, the elevation of the free water surface from the geoid; u, the depth-integrated velocity; and N, the action density. $H = \xi + h_b$ is the total height of the water column where h_b is the depth of the water below the geoid (bathymetry); g is the gravitational acceleration; $\mu > 0$ is the eddy viscosity; and F_x is the forcing function. Here for simplicity in the analysis, the only forcing considered is due to the wave radiation stress gradient; that is

$$F_x = \frac{\tau_{sx,wave}}{\rho H}$$

where ρ is the density of the water. The radiation stress gradient is [88]

$$\tau_{sx,wave} = -\nabla_x S_{xx},$$

where

$$S_{xx} = \rho g \int \int ((n \cos^2 \theta + n - \frac{1}{2})\sigma N) d\sigma d\theta,$$

and $n = \frac{1}{2}\left(1 + \frac{2kH}{\sinh(2kH)}\right)$. The propagation velocities $\mathbf{c} = (c_x, c_\sigma, c_\theta)$ in their simplified, one geographic dimensional form are [64]

$$c_x = c_g \cos(\theta) + u, \tag{6.4}$$

$$c_\sigma = \frac{k\sigma}{\sinh(2kH)}\left(H_t + u\nabla_x H\right) - c_g k \nabla_x u \cos^2\theta, \tag{6.5}$$

$$c_\theta = \frac{\sigma}{\sinh(2kH)}\nabla_x H \sin\theta + \nabla_x u \cos\theta \sin\theta, \tag{6.6}$$

where $c_g = nc$ is the group velocity, $c = \sigma/k$ is the phase speed, and k is the wave number, which is related to the frequency via the dispersion relationship $\sigma^2 = gk\tanh(kH)$. The source term, S, accounts for wind input, S_{in}, dissipation, S_d, and nonlinear wave-wave interactions, S_{nl}. The details of the source term can be found in Section 2.3 and here we only note that the source term can be written as

$$\frac{S}{\sigma} = S_{in} + S_d + S_{nl} = (f_S(H) + g_S(N))N$$

where f_S is Lipschitz continuous and g_S, which can depend on integral values of the action density, is also Lipschitz continuous.

For the error analysis only, we will consider the deep water assumption of $H \gg 0$ and thus $\tanh(kH) \approx 1$. This deep water assumption allows for the simplification of the group velocity as $c_g = g/\sigma$, $n = 1/2$, and the dispersion relationship becomes $\sigma = \sqrt{gk}$. When the deep water assumption is valid, the group velocity no longer depends on the depth of the water. To explore this, we plot in Figure 6.1 the group velocity for a range of depths for several different frequencies. When the frequency is 0.03 Hz, the group velocity slows

its dependence on depth around $H = 800$ m. However, for the higher frequencies of 0.1 Hz and 1.0 Hz we see that the group velocity no longer depends on depth for depths larger than 155 m and 1.6 m, respectively. Therefore if lower frequencies are included in the domain then we must restrict ourselves in the analysis to water depths larger than 800 m for the deep water assumption to be valid, but we can consider shallower water if we only consider higher frequencies. We also need for the horizontal length scale to be much larger than the vertical length scale, so that the shallow water equations are valid. For the error analysis, we rewrite the propagation velocities using the continuity equation in the expression for c_σ and by approximating the derivative of the total water depth by the derivative of the bathymetry in the expression for c_θ and obtain

$$c_\sigma = \frac{k\sigma}{\sinh(2kH)}\left(-H\nabla_x u\right) - c_g k \nabla_x u \cos^2\theta, \tag{6.7}$$

$$c_\theta = \frac{\sigma}{\sinh(2kH)}\nabla_x h_b \sin\theta + \nabla_x u \cos\theta \sin\theta. \tag{6.8}$$

For the analysis, we also approximate the total water depth by the bathymetry in the forcing function so that

$$F_x = \frac{\tau_{sx,wave}}{\rho h_b}. \tag{6.9}$$

For the shallow water equations, we consider the geographic boundary to be divided into an inflow and outflow region $\partial\Xi = \partial\Xi_{in} \cup \partial\Xi_{out}$, where

$$\partial\Xi_{in} = \{x \in \partial\Xi : u \cdot n_x < 0\},$$

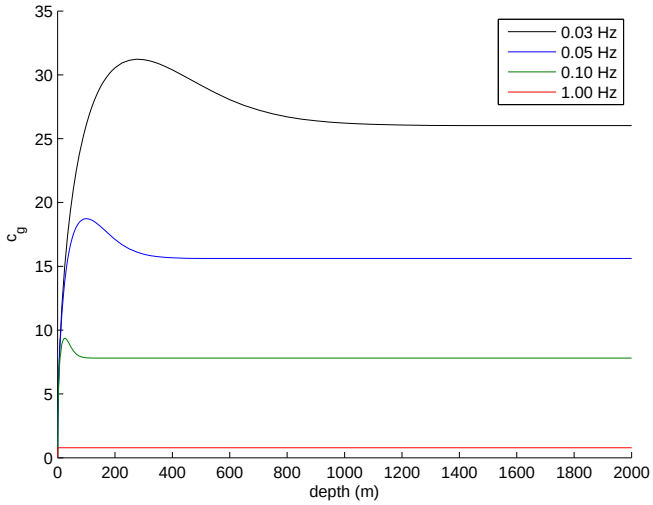

Figure 6.1: The group velocity for different depths for several frequencies

$$\partial\Xi_{out} = \{x \in \partial\Xi : u \cdot n_x \geq 0\},$$

with the following boundary conditions

$$u(x,t) = \widehat{u}(x,t), \quad \partial\Xi,$$
$$\xi(x,t) = \widehat{\xi}(x,t), \quad \partial\Xi_{in}.$$

For the action balance equation, we consider the entire boundary to be divided into an inflow and outflow region $\partial\Omega = \partial\Omega_{in} \cup \partial\Omega_{out}$, where

$$\partial\Omega_{in} = \{(x,\sigma,\theta) \in \partial\Omega : \mathbf{c} \cdot \mathbf{n} < 0\},$$
$$\partial\Omega_{out} = \{(x,\sigma,\theta) \in \partial\Omega : \mathbf{c} \cdot \mathbf{n} \geq 0\},$$

with the following boundary condition

$$N(x,\sigma,\theta,t) = \widehat{N}(x,\sigma,\theta,t), \quad \partial\Omega_{in}.$$

6.1.1 Notation and Definitions

Let $\{\mathscr{T}_h\}_{h>0}$ be a family of regular finite element partitions of Ω such that no single element $\Omega_e = \Xi_g \times \kappa_s$ crosses the boundary $\partial\Omega$ and $\mathscr{T}_h$ is locally quasi-uniform [13]. We assume each element Ω_e and Ξ_g is Lipschitz and affinely equivalent to a reference element [13]. Let h_g be the diameter of an element Ξ_g, h_e be the diameter of an element Ω_e, and h be the maximum element diameter.

For any $v \in H^1(\Xi_g)$, for each element Ξ_g, we denote the trace $v^{\pm}$ on the interior faces of Ξ_g, γ_i, by

$$v^-(x) = \lim_{s\to 0^-} v(x + sn_i), \quad v^+(x) = \lim_{s\to 0^+} v(x + sn_i),$$

where $x \in \gamma_i$ and n_i is a fixed unit vector normal to γ_i. Similarly for any $w \in H^1(\Omega_e)$, for each element Ω_e, we denote the trace $w^{\pm}$ on the interior edges of Ω_e, λ_j, by

$$w^-(\mathbf{x}) = \lim_{s\to 0^-} w(\mathbf{x} + s\mathbf{n}_j), \quad w^+(\mathbf{x}) = \lim_{s\to 0^+} w(\mathbf{x} + s\mathbf{n}_j),$$

where $\mathbf{x} = (x, \sigma, \theta) \in \lambda_j$ and $\mathbf{n}_j$ is a fixed unit vector normal to λ_j. We then define the average and jump of a function v over a geographic element face γ_i as

$$\{v\} = \frac{1}{2}(v^+ + v^-), \quad [v] = v^- - v^+,$$

and respectively, the average and jump of a function w over an element edge λ_j as

$$\{w\} = \frac{1}{2}(w^+ + w^-), \quad [w] = w^- - w^+.$$

We denote the sum over all elements in Ξ as $\sum_{\Xi_g \subset \Xi}$, the sum over all elements in the entire domain as $\sum_{\Omega_e \subset \Omega}$, the sum over all the geographic interior edges as $\sum_{\gamma_i \in \Gamma_\Xi}$, and the sum over all interior faces as $\sum_{\lambda_j \in \Gamma_\Omega}$.

We use the $L^2(R)$ inner product notation $(\cdot, \cdot)_R$ for the interior of a domain $R \in \mathbb{R}^d$, $d = 1, 2, 3$, and the notation $\langle \cdot, \cdot \rangle$ for the inner product over the edges or faces. Denote by $|| \cdot ||_R$ the L^2 norm on region R and note that for a function $f \in L^2(\Xi_g)$ or $g \in L^2(\Omega_e)$ that

$$||f||_\Xi = \sum_{\Xi_g \subset \Xi} ||f||_{\Xi_g}, \quad ||g||_\Omega = \sum_{\Omega_e \subset \Omega} ||g||_{\Omega_e}.$$

Let norms in other Sobolev spaces $W(R)$ be denoted $|| \cdot ||_{W(R)}$ and for a time dependent function $f = f(x, t)$

$$||f||_{L^\infty(0,T;W(R))} = \operatorname*{ess\,sup}_{0 \le t \le T} ||f(\cdot, t)||_{W(R)}.$$

6.2 Weak Formulations

Both the continuity equation and action balance equation will be discretized via a discontinuous Galerkin method. The momentum equation will be discretized via the nonsymmetric interior penalty Galerkin (NIPG) method with the upwinding technique of Lesaint and Raviart [81] applied to the advection term. We proceed by multiplying the continuity and momentum equations by test functions $\nu \in H^1(\Xi_g)$ and $v \in H^1(\Xi_g)$ on each geographic element $\Xi_g \subset \Xi$, integrate by parts and sum over each equation's results to obtain the weak formulations. Similarly, we multiply the action balance equation by a

test function $w \in H^1(\Omega_e)$ on each element $\Omega_e \subset \Omega$, integrate by parts and sum over the results to obtain the weak formulation. The system then contains the weak form of the continuity equation

$$\begin{aligned}(\xi_t, \nu)_\Xi - (uH, \nabla_x \nu)_\Xi + \sum_{\gamma_i \in \Gamma_\Xi} \langle Hu \cdot n_i, [\nu] \rangle_{\gamma_i} + \langle H\widehat{u} \cdot n_x, \nu \rangle_{\partial \Xi_{out}} \\ = -\langle \widehat{H}\widehat{u} \cdot n_x, \nu \rangle_{\partial \Xi_{in}}, \end{aligned} \tag{6.10}$$

where $\widehat{H} = \widehat{\xi} + h$, the momentum equation

$$\begin{aligned}(u_t, v)_\Xi + (u \cdot \nabla_x u, v)_\Xi + (g \nabla_x \xi, v)_\Xi + \mu(\nabla_x u, \nabla_x v)_\Xi \\ - \sum_{\gamma_i \in \Gamma_\Xi} \mu \langle \nabla_x u \cdot n_i, [v] \rangle_{\gamma_i} - \mu \langle \nabla_x u \cdot n_x, v \rangle_{\partial \Xi} = (F_x, v)_\Xi, \end{aligned} \tag{6.11}$$

and the action balance equation

$$\begin{aligned}(N_t, w)_\Omega - (\mathbf{c}N, \nabla w)_\Omega + \sum_{\lambda_j \in \Gamma_\Omega} \langle \mathbf{c}N \cdot \mathbf{n}_j, [w] \rangle_{\lambda_j} \\ + \langle \mathbf{c}N \cdot \mathbf{n}, w \rangle_{\partial \Omega_{out}} = \left(\frac{S}{\sigma}, w \right)_\Omega - \langle \mathbf{c}\widehat{N} \cdot \mathbf{n}, w \rangle_{\partial \Omega_{in}}. \end{aligned} \tag{6.12}$$

6.2.1 Discrete Weak Formulations

We begin by approximating the initial conditions with L^2 projections, computing $\xi_h(\cdot, 0), u_h(\cdot, 0) \in V_h(\Xi)$ and $N_h(\cdot, 0) \in W_h(\Omega)$ to satisfy

$$\begin{aligned}(\xi_0 - \xi_h(\cdot, 0), \nu) = 0, \quad \nu \in V_h(\Xi), \\ (u_0 - u_h(\cdot, 0), v) = 0, \quad v \in V_h(\Xi), \\ (N_0 - N_h(\cdot, 0), w) = 0, \quad w \in W_h(\Omega). \end{aligned}$$

We must slightly alter the definition of $\partial\Xi_{in}$ and $\partial\Xi_{out}$ to correspond with $u_h \cdot n_x < 0$ and $u_h \cdot n_x \geq 0$ and the definitions of $\partial\Omega_{in}$ and $\partial\Omega_{out}$ to correspond with $\mathbf{c}_h \cdot \mathbf{n} < 0$ and $\mathbf{c}_h \cdot \mathbf{n} \geq 0$. The free surface elevation ξ is approximated by $\xi_h \in V_h$ which satisfies the discrete weak form of the continuity equation

$$\begin{aligned}((\xi_h)_t, \nu)_\Xi - (u_h H_h, \nabla_x \nu)_\Xi + \sum_{\gamma_i \in \Gamma_\Xi} \langle H_h^\uparrow \{u_h\} \cdot n_i, [\nu] \rangle_{\gamma_i} \\ + \langle H_h u_h \cdot n_x, \nu \rangle_{\partial\Xi_{out}} = -\langle \widehat{H} u_h \cdot n_x, \nu \rangle_{\partial\Xi_{in}},\end{aligned} \tag{6.13}$$

where $H_h = \xi_h + h_b$ and the upwind value of H_h on each geographic interior edge γ_i is defined as

$$H_h^\uparrow = \begin{cases} H_h^- & \text{if } \{u_h\} \cdot n_i > 0, \\ H_h^+ & \text{if } \{u_h\} \cdot n_i \leq 0. \end{cases} \tag{6.14}$$

For the momentum equation, we add three stability terms involving $[u_h]$, $[\xi_h]$ and $[S_{xx,h}]$ which are zero for the true solutions. The depth-integrated velocity u is approximated by $u_h \in V_h$ which satisfies the discrete weak form

$$\begin{aligned}&((u_h)_t, v)_\Xi + (u_h \cdot \nabla_x u_h, v)_\Xi + \sum_g \langle |\{u_h\} \cdot n_e| (u_h^{int} - u_h^{ext}), v^{int} \rangle_{\partial\Xi_g^-} \\ &+ (g \nabla_x \xi_h, v)_\Xi - \sum_{\gamma_i \in \Gamma_\Xi} \langle g[\xi_h], \{v\} \cdot n_i \rangle_{\gamma_i} - \langle g(\xi_h - \widehat{\xi}), v \cdot n_x \rangle_{\partial\Xi_{in}} \\ &+ \mu(\nabla_x u_h, \nabla_x v)_\Xi - \sum_{\gamma_i \in \Gamma_\Xi} \mu \langle \{\nabla_x u_h\} \cdot n_i, [v] \rangle_{\gamma_i} \\ &+ \sum_{\gamma_i \in \Gamma_\Xi} \mu \langle \{\nabla_x v\} \cdot n_i, [u_h] \rangle_{\gamma_i} + \sum_{\gamma_i \in \Gamma_\Xi} \langle \alpha [u_h], [v] \rangle_{\gamma_i} \\ &- \mu \langle \nabla u_h \cdot n_x, v \rangle_{\partial\Xi} - \langle \alpha (u_h - \widehat{u}), v \rangle_{\partial\Xi} \\ &+ \mu \langle \nabla v \cdot n_x, u_h - \widehat{u} \rangle_{\partial\Xi} = (F_{x,h}, v) + \sum_{\gamma_i \in \Gamma_\Xi} \langle [S_{xx,h}], v \rangle_{\gamma_i},\end{aligned} \tag{6.15}$$

where α is a positive parameter which will be further discussed later. $\partial\Xi_g^- = \{x \in \partial\Xi_g : \{u_h\} \cdot n_x < 0\}$, v^{int} and v^{ext} are the traces of v from the interior and exterior of $\partial\Xi_g$, and when the edge of element Ξ_g belongs to the geographic boundary $\partial\Xi$, the exterior trace value $u_h^{ext} = \widehat{u}$. The action density N is approximated by $N_h \in W_h$, which fulfills the discrete weak form of the action balance equation

$$\begin{aligned}((N_h)_t, w)_\Omega - (\mathbf{c}_h N_h, \nabla w)_\Omega + \sum_{\lambda_j \in \Gamma_\Omega} \langle N_h^\uparrow \{\mathbf{c}_h\} \cdot n_j, [w] \rangle_{\lambda_j} \\ + \langle \mathbf{c}_h N_h \cdot n, w \rangle_{\partial\Omega_{out}} = \left(\frac{S_h}{\sigma}, w_h \right)_\Omega - \langle \mathbf{c}_h \widehat{N} \cdot n, w \rangle_{\partial\Omega_{in}}, \end{aligned} \tag{6.16}$$

where the upwind value of N_h on each interior edge λ_j is defined as

$$N_h^\uparrow = \begin{cases} N_h^- & \text{if } \{\mathbf{c}_h\} \cdot \mathbf{n}_j > 0, \\ N_h^+ & \text{if } \{\mathbf{c}_h\} \cdot \mathbf{n}_j \leq 0. \end{cases} \tag{6.17}$$

Note the definition of $N_h^\uparrow$ differs from the upwind value defined in (3.4) where the propagation velocities are assumed to be uniquely defined along element edges.

6.3 Error Equations

We now perform an *a priori* error analysis of the coupled system (6.1) - (6.3). To form the error equations we first must define the L^2 projections $\tilde{\xi}_h$, $\tilde{u}_h$ and $\tilde{N}_h$ into the approximation spaces for ξ_h, u_h and N_h such that for $t \geq$

$$\begin{aligned}((\tilde{\xi}_h - \xi)(\cdot, t), v) = 0 \quad v \in V_h, \\ ((\tilde{u}_h - u), \nu)(\cdot, t) = 0 \quad \nu \in V_h,\end{aligned}$$

$$((\tilde{N}_h - N), w)(\cdot, t) = 0 \quad v \in W_h.$$

Define

$$e_\xi = \xi_h - \tilde{\xi}_h, \quad \Theta_\xi = \xi - \tilde{\xi}_h,$$

with similar definitions for e_u, Θ_u, e_N and Θ_N. Let $\tilde{H}_h = \tilde{\xi}_h + h_b$ and note $e_\xi = H_h - \tilde{H}_h$.

We now perform manipulations to the weak forms to obtain the error equations, many of these arguments are repeated from Dawson and Proft [35]. We begin with the continuity equation by subtracting the weak form (6.10) from the discrete weak form (6.13) and setting $v = e_\xi$ to obtain

$$\begin{aligned}
&((e_\xi)_t, e_\xi)_\Xi - (u_h e_\xi, \nabla_x e_\xi)_\Xi + \sum_{\gamma_i \in \Gamma_\Xi} \langle e_\xi^\uparrow \{u_h\} \cdot n_i, [e_\xi] \rangle_{\gamma_i} + \langle e_\xi u_h \cdot n_x, e_\xi \rangle_{\partial \Xi_{out}} \\
&\quad = ((\Theta_\xi)_t, e_\xi)_\Xi - (uH - u_h \widetilde{H}_h, \nabla_x e_\xi)_\Xi + \sum_{\gamma_i \in \Gamma_\Xi} \langle (uH - \{u_h\} \widetilde{H}_h^\uparrow) \cdot n_i, [e_\xi] \rangle_{\gamma_i} \\
&\qquad + \langle (\widehat{u} H - u_h \widetilde{H}_h) \cdot n_x, e_\xi \rangle_{\partial \Xi_{out}} + \langle \widehat{u} \widehat{H} - u_h \widehat{H}) \cdot n_x, e_\xi \rangle_{\partial \Xi_{in}}. \qquad (6.18)
\end{aligned}$$

We then integrate by parts

$$\begin{aligned}
&- (u_h e_\xi, \nabla_x e_\xi)_\Xi + \sum_{\gamma_i \in \Gamma_\Xi} \langle e_\xi^\uparrow \{u_h\} \cdot n_i, [e_\xi] \rangle_{\gamma_i} + \langle e_\xi u_h \cdot n_x, e_\xi \rangle_{\partial \Xi_{out}} \\
&\quad = \frac{1}{2} (\nabla_x \cdot u_h, e_\xi^2)_\Xi - \frac{1}{2} \sum_{\gamma_i \in \Gamma_\Xi} \langle [u_h e_\xi^2 \cdot n_i], 1 \rangle_{\gamma_i} \\
&\qquad + \sum_{\gamma_i \in \Gamma_\Xi} \langle e_\xi^\uparrow \{u_h\} \cdot n_i, [e_\xi] \rangle_{\gamma_i} + \frac{1}{2} \langle |u_h \cdot n_x|, e_\xi^2 \rangle_{\partial \Xi_{in}} + \frac{1}{2} \langle |u_h \cdot n_x|, e_\xi^2 \rangle_{\partial \Xi_{out}}.
\end{aligned}$$

Use the fact that $[ab] = \{a\}[b] + [a]\{b\}$, $\frac{1}{2}[a^2] = [a]\{a\}$ and the definition of $e_\xi^\uparrow$ to get

$$- \frac{1}{2} \sum_{\gamma_i \in \Gamma_\Xi} \langle [u_h e_\xi^2 \cdot n_i], 1 \rangle_{\gamma_i} + \sum_{\gamma_i \in \Gamma_\Xi} \langle e_\xi^\uparrow \{u_h\} \cdot n_i, [e_\xi] \rangle_{\gamma_i}$$

$$
\begin{aligned}
&= \sum_{\gamma_i \in \Gamma_\Xi} \langle e_\xi^{\uparrow}[e_\xi]\{u_h\} \cdot n_i - \frac{1}{2}[e_\xi^2]\{u_h\} \cdot n_i - \frac{1}{2}\{e_\xi^2\}[u_h] \cdot n_i, 1\rangle_{\gamma_i} \\
&= \sum_{\gamma_i \in \Gamma_\Xi} \langle (e_\xi^{\uparrow} - \{e_\xi\})\{u_h\} \cdot n_i, [e_\xi]\rangle_{\gamma_i} - \frac{1}{2} \sum_{\gamma_i \in \Gamma_\Xi} \langle \{e_\xi^2\}, [u_h] \cdot n_i\rangle_{\gamma_i} \\
&= \frac{1}{2} \sum_{\gamma_i \in \Gamma_\Xi} \langle |\{u_h\} \cdot n_i|, [e_\xi]^2\rangle_{\gamma_i} - \frac{1}{2} \sum_{\gamma_i \in \Gamma_\Xi} \langle \{e_\xi^2\}, [u_h] \cdot n_i\rangle_{\gamma_i}.
\end{aligned}
$$

Then integrating $-(uH - u_h\widetilde{H}_h, \nabla_x e_\xi)_\Xi$ by parts we have

$$
\begin{aligned}
&- (uH - u_h\widetilde{H}_h, \nabla_x e_\xi)_\Xi + \langle (\widehat{u}\widehat{H} - u_h\widehat{H}) \cdot n_x, e_\xi\rangle_{\partial\Xi_{in}} + \langle (\widehat{u}H - u_h\widetilde{H}_h) \cdot n_x, e_\xi\rangle_{\partial\Xi_{out}} \\
&\quad = (\nabla_x \cdot (uH - u_h\widetilde{H}_h), e_\xi)_\Xi \\
&\qquad - \sum_{\gamma_i \in \Gamma_\Xi} \langle [e_\xi(uH - u_h\widetilde{H}_h) \cdot n_i], 1\rangle_{\gamma_i} + \langle (u_h\widetilde{H}_h - u_h\widehat{H}) \cdot n_x, e_\xi\rangle_{\partial\Xi_{in}}.
\end{aligned}
$$

The continuity error equation is then

$$
\begin{aligned}
&((e_\xi)_t, e_\xi)_\Xi + \frac{1}{2}(\nabla_x \cdot u_h, e_\xi^2)_\Xi + \frac{1}{2} \sum_{\gamma_i \in \Gamma_\Xi} \langle |\{u_h\} \cdot n_i|, [e_\xi]^2\rangle_{\gamma_i} \\
&\quad - \frac{1}{2} \sum_{\gamma_i \in \Gamma_\Xi} \langle \{e_\xi^2\}, [u_h] \cdot n_i\rangle_{\gamma_i} + \frac{1}{2}\langle |u_h \cdot n|, e_\xi^2\rangle_{\partial\Xi_{in}} + \frac{1}{2}\langle |u_h \cdot n|, e_\xi^2\rangle_{\partial\Xi_{out}} \\
&\quad = ((\Theta_\xi)_t, e_\xi)_\Xi + (\nabla_x \cdot (uH - u_h\widetilde{H}_h), e_\xi)_\Xi + \sum_{\gamma_i \in \Gamma_\Xi} \langle (uH - \{u_h\}\widetilde{H}_h^{\uparrow}) \cdot n_i, [e_\xi]\rangle_{\gamma_i} \\
&\qquad - \sum_{\gamma_i \in \Gamma_\Xi} \langle [e_\xi(uH - u_h\widetilde{H}_h) \cdot n_i], 1\rangle_{\gamma_i} + \langle (u_h\widetilde{H}_h - u_h\widehat{H}) \cdot n_x, e_\xi\rangle_{\partial\Xi_{in}}. \quad (6.19)
\end{aligned}
$$

We proceed with the momentum equation, subtract the weak form (6.11) from the discrete weak form (6.15) and let $v = e_u$ to obtain

$$
\begin{aligned}
&((e_u)_t, e_u)_\Xi + (g\nabla_x e_\xi, e_u)_\Xi - \sum_{\gamma_i \in \Gamma_\Xi} \langle g[e_\xi], \{e_u\} \cdot n_i\rangle_{\gamma_i} - \langle g e_\xi, e_u \cdot n_x\rangle_{\partial\Xi_{in}} \\
&\quad + \mu(\nabla_x e_u, \nabla_x e_u)_\Xi + \sum_{\gamma_i \in \Gamma_\Xi} \langle \alpha[e_u], [e_u]\rangle_{\gamma_i} + \langle \alpha e_u, e_u\rangle_{\partial\Xi}
\end{aligned}
$$

$$
\begin{aligned}
&= ((\Theta_u)_t, e_u)_\Xi + (u \cdot \nabla_x u - u_h \cdot \nabla_x u_h, e_u)_\Xi \\
&\quad - \sum_g \langle |\{u_h\} \cdot n_e| (u_h^{int} - u_h^{ext}), e_u^{int} \rangle_{\partial \Xi_g^-} + (g \nabla_x \Theta_\xi, e_u)_\Xi \\
&\quad - \sum_{\gamma_i \in \Gamma_\Xi} \langle g[\Theta_\xi], \{e_u\} \cdot n_i \rangle_{\gamma_i} - \langle g \Theta_\xi, e_u \cdot n_x \rangle_{\partial \Xi_{in}} + \mu (\nabla_x \Theta_u, \nabla_x e_u)_\Xi \\
&\quad + \sum_{\gamma_i \in \Gamma_\Xi} \langle \alpha [\Theta_u], [e_u] \rangle_{\gamma_i} - \sum_{\gamma_i \in \Gamma_\Xi} \langle \mu \{\nabla_x \Theta_u\} \cdot n_i, [e_u] \rangle_{\gamma_i} \\
&\quad + \sum_{\gamma_i \in \Gamma_\Xi} \langle \mu \{\nabla_x e_u\} \cdot n_i, [\Theta_u] \rangle_{\gamma_i} - \mu \langle \nabla_x \Theta_u \cdot n_x, e_u \rangle_{\partial \Xi} + \mu \langle \nabla_x e_u \cdot n_x, \Theta_u \rangle_{\partial \Xi} \\
&\quad + \langle \alpha \Theta_u, e_u \rangle_{\partial \Xi} + (F_{x,h} - F_x, e_u)_\Xi + \sum_{\gamma_i \in \Gamma_\Xi} \langle [S_{xx,h} - S_{xx}], \{e_u\} \rangle_{\gamma_i}. \qquad (6.20)
\end{aligned}
$$

Integrating $(g \nabla_x e_\xi, e_u)_\Xi$ by parts we get

$$
\begin{aligned}
&(g \nabla_x e_\xi, e_u)_\Xi - \sum_{\gamma_i \in \Gamma_\Xi} \langle g[e_\xi], \{e_u\} \cdot n_i \rangle_{\gamma_i} - \langle g e_\xi, e_u \cdot n_x \rangle_{\partial \Xi_{in}} \\
&\qquad = -(g e_\xi, \nabla_x \cdot e_u)_\Xi + \sum_{\gamma_i \in \Gamma_\Xi} \langle g\{e_\xi\}, [e_u] \cdot n_i \rangle_{\gamma_i} + \langle g e_\xi, e_u \cdot n_x \rangle_{\partial \Xi_{out}}.
\end{aligned}
$$

The momentum error equation then becomes

$$
\begin{aligned}
&((e_u)_t, e_u)_\Xi - (g e_\xi, \nabla_x \cdot e_u)_\Xi + \sum_{\gamma_i \in \Gamma_\Xi} \langle g\{e_\xi\}, [e_u] \cdot n_i \rangle_{\gamma_i} + \langle g e_\xi, e_u \cdot n_x \rangle_{\partial \Xi_{out}} \\
&\quad + \mu (\nabla_x e_u, \nabla_x e_u)_\Xi + \sum_{\gamma_i \in \Gamma_\Xi} \langle \alpha [e_u], [e_u] \rangle_{\gamma_i} + \langle \alpha e_u, e_u \rangle_{\partial \Xi} \\
&= ((\Theta_u)_t, e_u)_\Xi + (u \cdot \nabla_x u - u_h \cdot \nabla_x u_h, e_u)_\Xi \\
&\quad - \sum_g \langle |\{u_h\} \cdot n_e| (u_h^{int} - u_h^{ext}), e_u^{int} \rangle_{\partial \Xi_g^-} + (g \nabla_x \Theta_\xi, e_u)_\Xi \\
&\quad - \sum_{\gamma_i \in \Gamma_\Xi} \langle g[\Theta_\xi], \{e_u\} \cdot n_i \rangle_{\gamma_i} - \langle g \Theta_\xi, e_u \cdot n_x \rangle_{\partial \Xi_{in}} + \mu (\nabla_x \Theta_u, \nabla_x e_u)_\Xi \\
&\quad + \sum_{\gamma_i \in \Gamma_\Xi} \langle \alpha [\Theta_u], [e_u] \rangle_{\gamma_i} - \sum_{\gamma_i \in \Gamma_\Xi} \langle \mu \{\nabla_x \Theta_u\} \cdot n_i, [e_u] \rangle_{\gamma_i} \\
&\quad + \sum_{\gamma_i \in \Gamma_\Xi} \langle \mu \{\nabla_x e_u\} \cdot n_i, [\Theta_u] \rangle_{\gamma_i} - \mu \langle \nabla_x \Theta_u \cdot n_x, e_u \rangle_{\partial \Xi} + \mu \langle \nabla_x e_u \cdot n, \Theta_u \rangle_{\partial \Xi}
\end{aligned}
$$

$$+ \langle \alpha \Theta_u, e_u \rangle_{\partial \Xi} + (F_{x,h} - F_x, e_u)_{\Xi} + \sum_{\gamma_i \in \Gamma_{\Xi}} \langle [S_{xx,h} - S_{xx}], \{e_u\} \rangle_{\gamma_i}. \qquad (6.21)$$

Finally, we note that the action balance equation contains analogous terms to the continuity equation. Therefore, performing the same manipulations as before, we obtain action balance error equation

$$\begin{aligned}
&((e_N)_t, e_N)_{\Omega} + \frac{1}{2}\left(\nabla \cdot \mathbf{c}_h, e_N^2\right)_{\Omega} + \frac{1}{2} \sum_{\lambda_j \in \Gamma_{\Omega}} \langle |\{\mathbf{c}_h\} \cdot \mathbf{n}|, [e_N]^2 \rangle_{\lambda_j} \\
&\quad - \frac{1}{2} \sum_{\lambda_j \in \Gamma_{\Omega}} \langle \{e_N^2\}, [\mathbf{c}_h] \cdot \mathbf{n} \rangle_{\lambda_j} + \frac{1}{2} \langle |\mathbf{c}_h \cdot \mathbf{n}|, e_N^2 \rangle_{\partial \Omega_{out}} + \frac{1}{2} \langle |\mathbf{c}_h \cdot \mathbf{n}|, e_N^2 \rangle_{\partial \Omega_{in}} \\
&\quad = ((\Theta_N)_t, e_N)_{\Omega} + \left(\nabla \cdot (\mathbf{c}N - \mathbf{c}_h \widetilde{N}_h), e_N\right)_{\Omega} - \sum_{\lambda_j \in \Gamma_{\Omega}} \langle [e_N (\mathbf{c}N - \mathbf{c}_h \widetilde{N}_h) \cdot \mathbf{n}_j], 1 \rangle_{\lambda_j} \\
&\qquad + \sum_{\lambda_j \in \Gamma_{\Omega}} \langle \mathbf{c}N - \widetilde{N}_h^{\uparrow} \{\mathbf{c}_h\} \cdot \mathbf{n}, [e_N] \rangle_{\lambda_j} + \langle (\mathbf{c}_h \widetilde{N}_h - \mathbf{c}_h \widehat{N}) \cdot \mathbf{n}, e_N \rangle_{\partial \Omega_{in}} \\
&\qquad + \left(\frac{S_h - S}{\sigma}, e_N\right)_{\Omega}. \qquad (6.22)
\end{aligned}$$

Combine (6.19), (6.21) and (6.22), rearrange terms, and use the definition of the L^2 projection to obtain

$$\begin{aligned}
&((e_\xi)_t, e_\xi)_{\Xi} + ((e_u)_t, e_u)_{\Xi} + ((e_N)_t, e_N)_{\Omega} + ||\mu^{1/2} \nabla_x e_u||_{\Xi}^2 \\
&\quad + \frac{1}{2} \sum_{\gamma_i \in \Gamma_{\Xi}} \langle |\{u_h\} \cdot n_i|, [e_\xi]^2 \rangle_{\gamma_i} + \frac{1}{2} \langle |u_h \cdot n_x|, e_\xi^2 \rangle_{\partial \Xi_{in}} + \frac{1}{2} \langle |u_h \cdot n_x|, e_\xi^2 \rangle_{\partial \Xi_{out}} \\
&\quad + \sum_{\gamma_i \in \Gamma_{\Xi}} ||\alpha^{1/2} [e_u]||_{\gamma_i}^2 + ||\alpha^{1/2} e_u||_{\partial \Xi}^2 + \frac{1}{2} \sum_{\lambda_j \in \Gamma_{\Omega}} \langle |\{\mathbf{c}_h\} \cdot \mathbf{n}_j|, [e_N]^2 \rangle_{\lambda_j} \\
&\quad + \frac{1}{2} \langle |\mathbf{c}_h \cdot \mathbf{n}_j|, e_N^2 \rangle_{\partial \Omega_{out}} + \frac{1}{2} \langle |\mathbf{c}_h \cdot \mathbf{n}|, e_N^2 \rangle_{\partial \Omega_{in}} \\
&\quad = -\frac{1}{2} (\nabla_x \cdot u_h, e_\xi^2)_{\Xi} + (\nabla_x \cdot (uH - u_h \widetilde{H}_h), e_\xi)_{\Xi} + (g \nabla_x \Theta_\xi, e_u)_{\Xi} + (g e_\xi, \nabla_x \cdot e_u)_{\Xi} \\
&\qquad + \mu (\nabla_x \Theta_u, \nabla_x e_u)_{\Xi} + (u \cdot \nabla_x u - u_h \cdot \nabla_x u_h, e_u)_{\Xi} - \sum_{\gamma_i \in \Gamma_{\Xi}} \langle g [\Theta_\xi], \{e_u\} \cdot n_i \rangle_{\gamma_i}
\end{aligned}$$

$$
\begin{aligned}
&- \langle g\Theta_\xi, e_u \cdot n_x\rangle_{\partial\Xi_{in}} - \sum_{\gamma_i\in\Gamma_\Xi} \langle g\{e_\xi\}, [e_u]\cdot n_i\rangle_{\gamma_i} - \langle ge_\xi, e_u\cdot n_x\rangle_{\partial\Xi_{out}} \\
&+ \frac{1}{2}\sum_{\gamma_i\in\Gamma_\Xi} \langle\{e_\xi^2\}, [u_h]\cdot n_i\rangle_{\gamma_i} - \sum_{\gamma_i\in\Gamma_\Xi}\langle [e_\xi(uH - u_h\widetilde{H}_h)\cdot n_i], 1\rangle_{\gamma_i} \\
&+ \sum_{\gamma_i\in\Gamma_\Xi}\langle (uH - \{u_h\}\widetilde{H}_h^{\uparrow})\cdot n_i, [e_\xi]\rangle_{\gamma_i} + \langle (u_h\widetilde{H}_h - u_h\widehat{H})\cdot n_x, e_\xi\rangle_{\partial\Xi_{in}} \\
&- \sum_g \langle |\{u_h\}\cdot n_e|(u_h^{int} - u_h^{ext}), e_u^{int}\rangle_{\partial\Xi_g^-} - \sum_{\gamma_i\in\Gamma_\Xi}\langle \mu\{\nabla_x\Theta_u\}\cdot n_i, [e_u]\rangle_{\gamma_i} \\
&+ \sum_{\gamma_i\in\Gamma_\Xi}\langle \mu\{\nabla_x e_u\}\cdot n_i, [\Theta_u]\rangle_{\gamma_i} + \sum_{\gamma_i\in\Gamma_\Xi}\langle \alpha[\Theta_u], [e_u]\rangle_{\gamma_i} + \langle \alpha\Theta_u, e_u\rangle_{\partial\Xi} \\
&- \mu\langle \nabla_x\Theta_u\cdot n_x, e_u\rangle_{\partial\Xi} + \mu\langle \nabla_x e_u\cdot n_x, \Theta_u\rangle_{\partial\Xi} + (F_{x,h} - F_x, e_u)_\Xi \\
&+ \sum_{\gamma_i\in\Gamma_\Xi}\langle [S_{xx,h} - S_{xx}], \{e_u\}\rangle_{\gamma_i} - \frac{1}{2}\left(\nabla\cdot\mathbf{c}_h, e_N^2\right)_\Omega + \frac{1}{2}\sum_{\lambda_j\in\Gamma_\Omega}\langle\{e_N^2\}, [\mathbf{c}_h]\cdot\mathbf{n}_j\rangle_{\lambda_j} \\
&+ \left(\nabla\cdot(\mathbf{c}N - \mathbf{c}_h\widetilde{N}_h), e_N\right)_\Omega - \sum_{\lambda_j\in\Gamma_\Omega}\langle [e_N(\mathbf{c}N - \mathbf{c}_h\widetilde{N}_h)\cdot\mathbf{n}_j], 1\rangle_{\lambda_j} \\
&+ \sum_{\lambda_j\in\Gamma_\Omega}\langle \mathbf{c}N - \widetilde{N}_h^{\uparrow}\{\mathbf{c}_h\}\cdot\mathbf{n}_j, [e_N]\rangle_{\lambda_j} + \langle (\mathbf{c}_h\widetilde{N}_h - \mathbf{c}_h\widehat{N})\cdot\mathbf{n}, e_N\rangle_{\partial\Omega_{in}} \\
&+ \left(\frac{S_h - S}{\sigma}, e_N\right)_\Omega . \qquad (6.23)
\end{aligned}
$$

Integrate the previous equation in time and use the fact that $e_\xi(\cdot,0) = 0$, $e_u(\cdot,0) = 0$, and $e_N(\cdot,0) = 0$, and we obtain the error equation

$$
\begin{aligned}
&||e_\xi(T)||_\Xi^2 + ||e_u(T)||_\Xi^2 + ||e_N(T)||_\Omega^2 + 2\int_0^T ||\mu^{1/2}\nabla_x e_u||_\Xi^2 dt \\
&\quad + \int_0^T \sum_{\gamma_i\in\Gamma_\Xi}\langle |\{u_h\}\cdot n_i|, [e_\xi]^2\rangle_{\gamma_i} dt + \int_0^T \langle |u_h\cdot n_x|, e_\xi^2\rangle_{\partial\Xi_{in}} dt \\
&\quad + \int_0^T \langle |u_h\cdot n_x|, e_\xi^2\rangle_{\partial\Xi_{out}} dt + 2\int_0^T \sum_{\gamma_i\in\Gamma_\Xi} ||\alpha^{1/2}[e_u]||_{\gamma_i}^2 dt \\
&\quad + 2\int_0^T ||\alpha^{1/2}e_u||_{\partial\Xi}^2 dt + \int_0^T \sum_{\lambda_j\in\Gamma_\Omega}\langle |\{\mathbf{c}_h\}\cdot\mathbf{n}_j|, [e_N]^2\rangle_{\lambda_j} dt
\end{aligned}
$$

$$+\int_0^T \langle|\mathbf{c}_h\cdot\mathbf{n}|,e_N^2\rangle_{\partial\Omega_{out}}dt+\int_0^T \langle|\mathbf{c}_h\cdot\mathbf{n}|,e_N^2\rangle_{\partial\Omega_{in}}dt=2\sum_{k=1}^{30}E_k. \qquad (6.24)$$

6.4 Error Analysis

We will need the following theorems and identities to perform the error analysis. The following well known theorem [13] will frequently be used:

Theorem 6.4.1 *Suppose that region R has a Lipschitz boundary. Then, there exists a constant K_R^t such that*

$$||v||_{L^2(\partial R)}\leq K_R^t||v||_{L^2(R)}^{1/2}||v||_{H^1(R)}^{1/2}\quad \forall v\in H^1(R). \qquad (6.25)$$

Let $K_\Omega^t=\sup_h \max_{\Omega_e\in\Omega}K_{\Omega_e}^t$ and $K_\Xi^t=\sup_h \max_{\Xi_g\in\Xi}K_{\Xi_g}^t$, which can be shown to be finite for regular meshes. We define the trace constant $K^t=\max(K_\Omega^t,K_\Xi^t)$. We will need the inverse inequality in which for any functions $v\in V_h$ and $w\in W_h$

$$||v||_{H^1(\Xi_g)}\leq K_{\Xi_g}^i h_g^{-1}||v||_{\Xi_g}, \qquad (6.26)$$

and

$$||w||_{H^1(\Omega_e)}\leq K_{\Omega_e}^i h_e^{-1}||w||_{\Omega_e}, \qquad (6.27)$$

where K_R^i is independent of h_g,h_e but depends on the shape parameters of region R. Let $K^i=\max_{e,g}(K_{\Omega_e}^i,K_{\Xi_g}^i)$. When the Cauchy-Schwarz inequality is applied to the L^2 product over the domain Ω when one of the functions is

only a function of geographic space, we obtain a factor, K^k, of the size of the spectral domain such that

$$|\kappa| \leq 2\pi\sigma_{\max} \leq K^k. \tag{6.28}$$

In keeping with the deep water assumption we assume $H^* > H, H_h, \tilde{H}_h > H_* > 0$ and that there is a constant K^c such that

$$\begin{aligned}
&||h_b||_{L^\infty(0,T;W_1^\infty(\Xi))} + ||c_g||_{L^\infty(0,T;W_1^\infty(\Omega))} + ||k||_{L^\infty(0,T;W_1^\infty(\Omega))} \\
&\quad + \left|\left|\frac{\sigma}{\sinh 2kH}\right|\right|_{L^\infty(0,T;L^\infty(\Omega))} + \left|\left|\nabla_\sigma\left(\frac{\sigma kH}{\sinh 2kH}\right)\right|\right|_{L^\infty(0,T;L^\infty(\Omega))} \\
&\quad + \left|\left|\frac{\sigma}{\sinh 2kH_h}\right|\right|_{L^\infty(0,T;L^\infty(\Omega))} + \left|\left|\nabla_\sigma\left(\frac{\sigma kH_h}{\sinh 2kH_h}\right)\right|\right|_{L^\infty(0,T;L^\infty(\Omega))} \leq K^c.
\end{aligned} \tag{6.29}$$

We make the following assumption on the solutions and the projections

$$\begin{aligned}
&||H||_{L^\infty(0,T;W_1^\infty(\Xi))} + ||u||_{L^\infty(0,T;W_1^\infty(\Xi))} + ||N||_{L^\infty(0,T;W_1^\infty(\Omega))} \\
&\quad + ||\tilde{H}_h||_{L^\infty(0,T;W_1^\infty(\Xi))} + ||\tilde{u}_h||_{L^\infty(0,T;W_1^\infty(\Xi))} + ||\tilde{N}_h||_{L^\infty(0,T;W_1^\infty(\Omega))} \leq K^m.
\end{aligned} \tag{6.30}$$

We also assume that there exists a finite constant $K^M \geq 2K^m$ and independent of h such that

$$||e_\xi||_{L^\infty(0,T;L^\infty(\Xi))} + ||e_u||_{L^\infty(0,T;L^\infty(\Xi))} + ||e_N||_{L^\infty(0,T;L^\infty(\Omega))} \leq K^M. \tag{6.31}$$

For the analysis, we will need Young's inequality

$$ab \leq \frac{\epsilon}{2}a^2 + \frac{1}{2\epsilon}b^2. \tag{6.32}$$

We use the basic principles of the following generic arguments throughout the analysis. For functions f, g and ω over region R (which could be either Ω or Ξ), we have that

$$\begin{aligned}(gf - g_h f_h, \omega)_R &= (g(f - f_h) - (g - g_h)f_h, \omega)_R \\ &= (g(\theta_f - e_f) - (\theta_g - e_g)f_h, \omega)_R \\ &\leq C||g||_{L^\infty(R)}(||\theta_f||_R + ||e_f||_R + ||\omega||_R) \\ &\quad + C||f_h||_{L^\infty(R)}(||\theta_g||_R + ||e_g||_R + ||\omega||_R), \end{aligned} \tag{6.33}$$

and, similarly,

$$\begin{aligned}(\nabla_x(gf - g_h f_h), \omega)_R &= (\nabla_x(g(f - f_h) - (g - g_h)f_h), \omega)_R \\ &= (\nabla_x g(\theta_f - e_f) + g\nabla_x(\theta_f - e_f), \omega)_R \\ &\quad - (\nabla_x(\theta_g - e_g)f_h - (\theta_g - e_g)\nabla_x f_h, \omega)_R \\ &\leq ||g||_{L^\infty(R)}(||\nabla_x\theta_f||_R + ||\nabla_x e_f||_R + ||\omega||_R) \\ &\quad + C||\nabla_x g||_{L^\infty(R)}(||\theta_f||_R + ||e_f||_R + ||\omega||_R) \\ &\quad + C||f_h||_{L^\infty(R)}(||\nabla_x\theta_g||_R + ||\nabla_x e_g||_R + ||\omega||_R) \\ &\quad + C||\nabla_x f_h||_{L^\infty(R)}(||\theta_g||_R + ||e_g||_R + ||\omega||_R). \end{aligned} \tag{6.34}$$

Before we continue with arguments over boundaries, we introduce some notation. Let $\mathscr{E}_i = \{\Xi_g : \partial\Xi_g \cap \gamma_i \neq \varnothing\}$ for each edge γ_i and $\mathscr{E}_j = \{\Omega_e : \partial\Omega_e \cap \lambda_j \neq \varnothing\}$ for each face λ_j. Below, C denotes a positive generic constant, $C(K^*)$ denotes that C depends on K^*, and let ϵ_i, $i = 1, 2, 3, 4$, be a small generic constant. In the first argument, over the boundary of region R, we use Theorem

6.4.1 as well as the inverse and Young's inequalities to obtain

$$\begin{aligned}\langle f,g\rangle_{\partial R} &\leq K^t||f||_R^{1/2}||f||_{H^1(R)}^{1/2}||g||_R^{1/2}||g||_{H^1(R)}^{1/2}\\ &\leq K^tK^ih^{-1/2}||f||_R^{1/2}||f||_{H^1(R)}^{1/2}||g||_R\\ &\leq C(K^t,K^i)h^{-1}||f||_R||f||_{H^1(R)}+\epsilon||g||_R^2\\ &\leq C(K^t,K^i)(h^{-2}||f||_R^2+||f||_{H^1(R)}^2)+\epsilon||g||_R^2, \qquad (6.35)\end{aligned}$$

for $g \in V_h$ or W_h. In the second argument, we utilize the positive constant α. We assume that $\alpha_{i,*}$, α_i^* are positive parameters such that

$$\alpha_{i,*} \leq \alpha|_{\gamma_i} \leq \alpha_i^*, \quad \alpha_{i,*}, \alpha_i^* = O(h_i^{-1}), \qquad (6.36)$$

where

$$h_i = \min_{\Xi_g \subset \mathscr{E}_i} h_g.$$

Then, using α, Theorem 6.4.1, and Young's inequality we find

$$\begin{aligned}\langle f,g\rangle_{\partial R} &\leq ||\alpha^{-1/2}f||_{\partial R}||\alpha^{1/2}g||_{\partial R}\\ &\leq K^t\alpha_{R,*}^{-1/2}||f||_R^{1/2}||f||_{H^1(R)}^{1/2}||\alpha^{1/2}g||_{\partial R}\\ &\leq C(K^t)h_R||f||_R||f||_{H^1(R)}+\epsilon||\alpha^{1/2}g||_{\partial R}^2 \qquad (6.37)\\ &\leq C(K^t,K^i)||f||_R^2+\epsilon||\alpha^{1/2}g||_{\partial R}^2, \qquad (6.38)\end{aligned}$$

where one can stop at (6.37) or apply the inverse inequality if $f \in V_h$ or W_h and obtain (6.38).

We now continue by estimating the terms on the right hand side of (6.24), which repeats many arguments from Dawson and Proft [35]. Some of

the same arguments are used in the analysis of the action balance equation. By assumptions (6.30) and (6.31) we find

$$\begin{aligned} E_1 &= -\frac{1}{2}\int_0^T (\nabla_x \cdot u_h, e_\xi^2)_\Xi dt \\ &= -\frac{1}{2}\int_0^T (\nabla_x \cdot (e_u - \Theta_u + u), e_\xi^2)_\Xi dt \\ &\leq \epsilon_1 \int_0^T ||\nabla_x e_u||_\Xi^2 dt + C(K^M)\int_0^T ||\nabla_x \Theta_u||_\Xi^2 dt + C(K^m, K^M)\int_0^T ||e_\xi||_\Xi^2 dt. \end{aligned} \tag{6.39}$$

Again by assumptions (6.30) and (6.31) and following the arguments in (6.34), we have

$$\begin{aligned} E_2 &= \int_0^T (\nabla_x \cdot (uH - u_h\widetilde{H}_h), e_\xi)_\Xi dt \\ &\leq C(K^m, K^M)\int_0^T ||\Theta_u||_{H^1(\Xi)}^2 dt + C(K^m, K^M)\int_0^T ||\Theta_\xi||_{H^1(\Xi)}^2 dt \\ &\quad + \epsilon_1 \int_0^T ||\nabla_x e_u||_\Xi^2 dt + C(K^m, K^M)\int_0^T ||e_\xi||_\Xi^2 dt. \end{aligned} \tag{6.40}$$

Using Young's inequality, we find

$$\begin{aligned} E_3 + E_4 + E_5 &= \int_0^T (g\nabla_x \Theta_\xi, e_u)_\Xi dt + \int_0^T (g e_\xi, \nabla_x \cdot e_u)_\Xi dt \\ &\quad + \int_0^T \mu(\nabla_x \Theta_u, \nabla_x e_u)_\Xi dt \\ &\leq C\int_0^T ||\nabla_x \Theta_\xi||_\Xi^2 dt + C\int_0^T ||e_u||_\Xi^2 dt + C\int_0^T ||e_\xi||_\Xi^2 dt \\ &\quad + \epsilon_1 \int_0^T ||\nabla_x e_u||_\Xi^2 dt + C\int_0^T ||\nabla_x \Theta_u||_\Xi^2 dt. \end{aligned} \tag{6.41}$$

Following the argument in (6.34), we get

$$E_6 = \int_0^T (u \cdot \nabla_x u - u_h \cdot \nabla_x u_h, e_u)_\Xi dt$$

$$\leq C(K^m)\int_0^T ||\Theta_u||^2_\Xi dt + C(K^m,K^M)\int_0^T (||e_u||^2_\Xi + ||\nabla_x\Theta_u||^2_\Xi)dt$$
$$+\epsilon_1\int_0^T ||\nabla_x e_u||^2_\Xi dt. \tag{6.42}$$

For E_7, apply the argument in (6.35) to obtain

$$E_7 = \int_0^T \sum_{\gamma_i\in\Gamma_\Xi}\langle g[\Theta_\xi],\{e_u\}\cdot n_i\rangle_{\gamma_i}dt$$
$$\leq C(K^t,K^i)\int_0^T\sum_{\Xi_g\subset\Xi}[h_g^{-2}||\Theta_\xi||^2_{\Xi_g} + ||\Theta_\xi||^2_{H^1(\Xi_g)}]dt + C\int_0^T ||e_u||^2_\Xi dt, \tag{6.43}$$

with a similar bound for E_8. Employing the argument in (6.38) we have

$$E_9 = -\int_0^T\sum_{\gamma_i\in\Gamma_\Xi}\langle g\{e_\xi\},[e_u]\cdot n_i\rangle_{\gamma_i}dt$$
$$\leq C(K^t,K^i)\int_0^T||e_\xi||^2_\Xi dt + \epsilon_2\int_0^T\sum_{\gamma_i\in\Gamma_\Xi}||\alpha^{1/2}[e_u]||^2_{\gamma_i}dt, \tag{6.44}$$

and an analogous bound for E_{10}. Following the strategies in (6.35) and (6.38) coupled with the fact that $[u]=0$ on γ_i, we have

$$E_{11} = -\frac{1}{2}\int_0^T\sum_{\gamma_i\in\Gamma_\Xi}\langle\{e_\xi^2\},[u_h]\cdot n_i\rangle_{\gamma_i}dt$$
$$= \frac{1}{2}\int_0^T\sum_{\gamma_i\in\Gamma_{int}}\langle\{e_\xi^2\},([e_u]-[\Theta_u])\cdot n_i\rangle_{\gamma_i}dt$$
$$\leq \epsilon_2\int_0^T\sum_{\gamma_i\in\Gamma_\Xi}||\alpha^{1/2}[e_u]||^2_{\gamma_i}dt + C(K^t)\int_0^T\sum_{\Xi_g\subset\Xi}(h_g^{-2}||\Theta_u||^2_{\Xi_g} + ||\Theta_u||^2_{H^1(\Xi_g)})dt$$
$$+C(K^M,K^t,K^i)\int_0^T||e_\xi||^2_\Xi dt. \tag{6.45}$$

Use $\{ab\}=\{a\}\{b\}+\frac{1}{4}[a][b]$ and $[ab]=\{a\}[b]+[a]\{b\}$ to obtain

$$E_{12}+E_{13} = -\int_0^T\sum_{\gamma_i\in\Gamma_\Xi}\langle[e_\xi(uH-u_h\widetilde{H}_h)\cdot n_i],1\rangle_{\gamma_i}dt$$

$$
\begin{aligned}
&+\int_0^T \sum_{\gamma_i\in\Gamma_\Xi} \langle (uH - \{u_h\}\widetilde{H}_h^{\uparrow})\cdot n_i, [e_\xi]\rangle_{\gamma_i} dt \\
&= \int_0^T \sum_{\gamma_i\in\Gamma_\Xi} \langle \left(\Theta_\xi^{\uparrow} - \{\Theta_\xi\}\right)\{u_h\}\cdot n_i - \frac{1}{4}[\Theta_\xi][u_h]\cdot n_i, [e_\xi]\rangle_{\gamma_i} dt \\
&+\int_0^T \sum_{\gamma_i\in\Gamma_\Xi} \langle \{\widetilde{H}_h\}\left([e_u] - [\Theta_u]\right)\cdot n_i - [\Theta_\xi]\{u_h\}\cdot n_i, \{e_\xi\}\rangle_{\gamma_i} dt.
\end{aligned}
$$

We then use (6.35) to obtain

$$
\begin{aligned}
&\int_0^T \sum_{\gamma_i\in\Gamma_\Xi} \langle \left(\Theta_\xi^{\uparrow} - \{\Theta_\xi\}\right)\{u_h\}\cdot n_i, [e_\xi]\rangle_{\gamma_i} dt \\
&\leq C(K^m, K^M, K^t)\int_0^T \sum_{\Xi_g\subset\Xi} (h_g^{-2}||\Theta_\xi||_\Xi^2 + ||\Theta_\xi||_{H^1(\Xi)}^2) dt \\
&\quad + C(K^m, K^M, K^t, K^i)\int_0^T ||e_\xi||_\Xi^2 dt, \qquad (6.46)
\end{aligned}
$$

with similar bounds for the two terms with $[\Theta_\xi]$ and a nearly identical bound to E_{11} for the remaining term $\int_0^T \sum_{\gamma_i\in\Gamma_\Xi}\langle\{\widetilde{H}_h\}\left([e_u] - [\Theta_u]\right)\cdot n_i, \{e_\xi\}\rangle_{\gamma_i} dt$. Applying the Theorem 6.4.1 and (6.32) we have

$$
\begin{aligned}
E_{14} &= \int_0^T \langle (u_h\widetilde{H}_h - u_h\widehat{H})\cdot n_x, e_\xi\rangle_{\partial\Xi_{in}} dt \\
&\leq C(K^m, K^M)\int_0^T ||\Theta_\xi||_{\partial\Xi_{in}}^2 dt + \epsilon_3\int_0^T \langle |u_h\cdot n_x|, e_\xi^2\rangle_{\partial\Xi_{in}} dt \\
&\leq C(K^m, K^M, K^t)\int_0^T (||\Theta_\xi||_\Xi^2 + ||\Theta_\xi||_{H^1(\Xi)}^2) dt + \epsilon_3\int_0^T \langle |u_h\cdot n_x|, e_\xi^2\rangle_{\partial\Xi_{in}} dt. \qquad (6.47)
\end{aligned}
$$

For E_{15}, use arguments (6.35) and (6.38) so that

$$
E_{15} = -\int_0^T \sum_g \langle |\{u_h\}\cdot n_g|(u_h^{int} - u_h^{ext}), e_u^{int}\rangle_{\partial\Xi_g^-} dt
$$

$$
\begin{aligned}
&\leq \int_0^T \sum_g \langle |(\{e_u\} + \{\widetilde{u}_h\}) \cdot n_g| |[\Theta_u] - [e_u]|, |e_u^{int}| \rangle_{\partial \Xi_g^-} dt \\
&\leq C(K^m, K^M, K^t, K^i) \int_0^T ||e_u||_\Xi^2 dt + \epsilon_2 \int_0^T \sum_{\gamma_i \in \Gamma_\Xi} ||\alpha^{1/2}[e_u]||_{\gamma_i}^2 dt \\
&\quad + C(K^t) \int_0^T \sum_{\Xi_g \in \Xi} (h_g^{-2} ||\Theta_u||_\Xi^2 + ||\Theta_u||_{H^1(\Xi)}^2) dt + \epsilon_4 \int_0^T ||\alpha^{1/2} e_u||_{\partial \Xi}^2 dt,
\end{aligned}
\tag{6.48}
$$

and use (6.37) to find

$$
\begin{aligned}
E_{16} &= -\int_0^T \sum_{\gamma_i \in \Gamma_\Xi} \langle \mu \{\nabla_x \Theta_u\} \cdot n_i, [e_u] \rangle_{\gamma_i} dt \\
&\leq C(K^t) \int_0^T \sum_{\Xi_g \subset \Xi} h_g ||\nabla_x \Theta_u||_{\Xi_g} ||\nabla_x \Theta_u||_{H^1(\Xi_g)} dt + \epsilon_2 \int_0^T \sum_{\gamma_i \in \Gamma_\Xi} ||\alpha^{1/2}[e_u]||_{\gamma_i}^2 dt.
\end{aligned}
\tag{6.49}
$$

Similarly, (6.35) gives us that

$$
\begin{aligned}
E_{17} &= \int_0^T \sum_{\gamma_i \in \Gamma_\Xi} \langle \mu \{\nabla_x e_u\} \cdot n_i, [\Theta_u] \rangle_{\gamma_i} dt \\
&\leq \epsilon_1 \int_0^T ||\nabla_x e_u||_{\Xi_g}^2 dt + C(K^t, K^i) \int_0^T \sum_{\Xi_g \subset \Xi} (h_g^{-2} ||\Theta_u||_{\Xi_g}^2 + ||\Theta_u||_{H^1(\Xi_g)}^2) dt.
\end{aligned}
\tag{6.50}
$$

Simply using Theorem 6.4.1, (6.26), and (6.36) we get

$$
\begin{aligned}
E_{18} + E_{19} &= \int_0^T \sum_{\gamma_i \in \Gamma_\Xi} \langle \alpha[\Theta_u], [e_u] \rangle_{\gamma_i} dt + \int_0^T \langle \alpha \Theta_u, e_u \rangle_{\partial \Xi} dt \\
&\leq C \int_0^T \Big(\sum_{\gamma_i \in \Gamma_\Xi} ||\alpha^{1/2}[\Theta_u]||_{\gamma_i}^2 + ||\alpha^{1/2}[\Theta_u]||_{\partial \Xi}^2 \Big) dt \\
&\quad + \epsilon_2 \int_0^T \sum_{\gamma_i \in \Gamma_\Xi} ||\alpha^{1/2}[e_u]||_{\gamma_i}^2 dt + \epsilon_4 \int_0^T ||\alpha^{1/2} e_u||_{\partial \Xi}^2 dt
\end{aligned}
$$

$$\leq C(K^t)\int_0^T \sum_{\Xi_g\subset\Xi}(h_g^{-2}||\Theta_u||^2_{\Xi_g}+||\Theta_u||^2_{H^1(\Xi_g)})dt$$
$$+\epsilon_2\int_0^T\sum_{\gamma_i\in\Gamma_\Xi}||\alpha^{1/2}[e_u]||^2_{\gamma_i}dt+\epsilon_4\int_0^T||\alpha^{1/2}e_u||^2_{\partial\Xi}dt, \qquad (6.51)$$

and using (6.35) and (6.38) we have

$$E_{20}+E_{21}=-\int_0^T\langle\mu\nabla_x\Theta_u\cdot n,e_u\rangle_{\partial\Xi}dt+\int_0^T\langle\mu\nabla_x e_u\cdot n,\Theta_u\rangle_{\partial\Xi}dt$$
$$\leq\epsilon_1\int_0^T||\nabla_x e_u||^2_{\Xi_g}dt+\epsilon_4\int_0^T||\alpha^{1/2}e_u||^2_{\partial\Xi}dt$$
$$+C(K^t)\int_0^T\sum_{\Xi_g\subset\Xi}h_g||\nabla_x\Theta_u||_{\Xi_g}||\nabla_x\Theta_u||_{H^1(\Xi_g)}dt$$
$$+C(K^t,K^i)\int_0^T\sum_{\Xi_g\subset\Xi}(h_g^{-2}||\Theta_u||^2_{\Xi_g}+||\Theta_u||^2_{H^1(\Xi_g)})dt. \qquad (6.52)$$

Integrating E_{22} by parts, using the definition of F_x, and applying the argument in (6.38) on the boundary terms we obtain

$$E_{22}+E_{23}=\int_0^T(F_{x,h}-F_x,e_u)_\Xi dt+\sum_{\gamma_i\in\Gamma_\Xi}\langle[S_{xx,h}-S_{xx}],\{e_u\}\cdot n_i\rangle_{\gamma_i}$$
$$=\int_0^T\left(\int_{\theta_{\min}}^{\theta_{\max}}\int_{\sigma_{\min}}^{\sigma_{\max}}\left(\frac{1}{2}\cos^2\theta\sigma(N_h-N)\right)d\sigma d\theta,\nabla_x\left(\frac{g}{h_b}e_u\right)\right)_\Xi dt$$
$$-\sum_{\gamma_i\in\Gamma_\Xi}\int_0^T\langle\int_{\theta_{\min}}^{\theta_{\max}}\int_{\sigma_{\min}}^{\sigma_{\max}}\left(\frac{1}{2}\cos^2\theta\sigma\{N_h-N\}\right)d\sigma d\theta,\frac{g}{h_b}[e_u]\cdot n_i\rangle_{\gamma_i}dt$$
$$-\int_0^T\langle\int_{\theta_{\min}}^{\theta_{\max}}\int_{\sigma_{\min}}^{\sigma_{\max}}\left(\frac{1}{2}\cos^2\theta\sigma(N_h-N)\right)d\sigma d\theta,\frac{g}{h_b}e_u\cdot n_x\rangle_{\partial\Xi}dt$$
$$\leq C(K^c)\int_0^T||e_u||^2_\Xi dt+\epsilon_1\int_0^T||\nabla_x e_u||^2_\Xi dt$$
$$+C(K^t,K^i,K^c,K^k)\int_0^T(||e_N||^2_\Omega+||\Theta_N||^2_\Omega)dt$$
$$+\epsilon_2\int_0^T\sum_{\gamma_i\in\Gamma_\Xi}||\alpha^{1/2}[e_u]||_{\gamma_i}dt+\epsilon_4\int_0^T||\alpha^{1/2}e_u||_{\partial\Xi}dt. \qquad (6.53)$$

Expanding terms and defining $B(H) = \nabla_\sigma \frac{k\sigma H}{\sinh(2kH)}$ which is a Lipschitz continuous function, we have

$$
\begin{aligned}
E_{24} &= -\frac{1}{2}\int_0^T \left(\nabla \cdot \mathbf{c}_h, e_N^2\right)_\Omega dt \\
&= -\frac{1}{2}\int_0^T \left(\cos\theta \nabla_x c_g, e_N^2\right)_\Omega dt - \frac{1}{2}\int_0^T \left((1+\frac{1}{2}\cos^2\theta + \cos 2\theta)\nabla_x u_h, e_N^2\right)_\Omega dt \\
&\quad + \frac{1}{2}\int_0^T \left(\nabla_x u_h B(H_h), e_N^2\right)_\Omega dt - \frac{1}{2}\int_0^T \left(\frac{\sigma}{\sinh(2kH_h)}\nabla_x h_b \cos\theta, e_N^2\right)_\Omega dt \\
&= -\frac{1}{2}\int_0^T \left(\cos\theta \nabla_x c_g, e_N^2\right)_\Omega dt \\
&\quad - \frac{1}{2}\int_0^T \left((1+\frac{1}{2}\cos^2\theta + \cos 2\theta)\nabla_x (e_u - \Theta_u + u), e_N^2\right)_\Omega dt \\
&\quad + \frac{1}{2}\int_0^T \left(\nabla_x (e_u - \Theta_u + u) B(e_\xi - \Theta_\xi + H), e_N^2\right)_\Omega dt \\
&\quad - \frac{1}{2}\int_0^T \left(\frac{\sigma}{\sinh(2kH_h)}\nabla_x h_b \cos\theta, e_N^2\right)_\Omega dt \\
&\leq C(K^M, K^k)\int_0^T ||\nabla_x \Theta_u||_\Xi^2 dt + C(K^m, K^M, K^c, K^k)\int_0^T ||e_N||_\Omega^2 dt \\
&\quad + \epsilon_1 \int_0^T ||\nabla_x e_u||_\Xi^2 dt + C(K^m, K^M, K^k)\int_0^T (||e_\xi||_\Xi^2 + ||\Theta_\xi||_\Xi^2 + ||\nabla_x \Theta_u||_\Xi^2) dt.
\end{aligned} \tag{6.54}
$$

Since $[(c_g \cos\theta, c_{\sigma,h}, c_{\theta,h})] = 0$ on λ_j, we follow E_{11} to get

$$
\begin{aligned}
E_{25} &= \frac{1}{2}\sum_{\lambda_j \in \Gamma_\Omega} \langle \{e_N^2\}, [\mathbf{c}_h] \cdot \mathbf{n} \rangle_{\lambda_j} = \frac{1}{2}\sum_{\gamma_i \in \Gamma_\Xi} \langle \{e_N^2\}, [u_h] \cdot n_i \rangle_{\gamma_i \times \kappa} \\
&\leq \epsilon_2 \int_0^T \sum_{\gamma_i \in \Gamma_\Xi} ||\alpha^{1/2}[e_u]||_{\gamma_i}^2 dt + C(K^t)\int_0^T \sum_{\Xi_g \subset \Xi} [h_g^{-2}||\Theta_u||_{\Xi_g}^2 + ||\Theta_u||_{H^1(\Xi_g)}^2] dt \\
&\quad + C(K^M, K^t, K^i, K^k)\int_0^T ||e_N||_\Omega^2 dt.
\end{aligned} \tag{6.55}
$$

Define $g(H) = -\frac{k\sigma}{\sinh(2kH)}H - \cos^2\theta c_g k$, which is a Lipschitz continuous function, and expand to obtain

$$\begin{aligned}
E_{26} &= \left(\nabla\cdot(\mathbf{c}N - \mathbf{c}_h\widetilde{N}_h), e_N\right)_\Omega \\
&= \int_0^T \left(\cos\theta c_g \nabla_x(N-\widetilde{N}_h), e_N\right)_\Omega dt + \int_0^T \left(\nabla_x(uN - u_h\widetilde{N}_h), e_N\right)_\Omega dt \\
&\quad + \int_0^T \left(\nabla_\sigma\left(g(H)\nabla_x uN - g(H_h)\nabla_x u_h\widetilde{N}_h\right), e_N\right)_\Omega dt \\
&\quad + \int_0^T \left(\nabla_\theta\left(\frac{\sigma}{\sinh(2kH)}\nabla_x h_b \sin\theta N - \frac{\sigma}{\sinh(2kH_h)}\nabla_x h_b\sin\theta\widetilde{N}_h\right), e_N\right)_\Omega dt \\
&\quad + \int_0^T \left(\nabla_\theta(\nabla_x u\cos\theta\sin\theta N - \nabla_x u_h\cos\theta\sin\theta\widetilde{N}_h), e_N\right)_\Omega dt \\
&= \sum_{i=1}^5 E_{26,i}, \qquad (6.56)
\end{aligned}$$

where

$$E_{26,1} = \int_0^T (\cos\theta c_g\nabla_x\Theta_N, e_N)_\Omega dt \le C(K^c)\int_0^T (||\nabla_x\Theta_N||_\Omega^2 + ||e_N||_\Omega^2)dt. \qquad (6.57)$$

Following E_2, we use (6.34) and have

$$\begin{aligned}
E_{26,2} &= \int_0^T (\nabla_x\cdot(uN - u_h\widetilde{N}_h), e_N)_\Omega dt \\
&\le C(K^m, K^M, K^k)\int_0^T (||\Theta_u||_{H^1(\Xi)}^2 + ||\Theta_N||_{H^1(\Omega)}^2 + ||e_N||_\Omega^2)dt \\
&\quad + \epsilon_1\int_0^T ||\nabla_x e_u||_\Xi^2 dt. \qquad (6.58)
\end{aligned}$$

For the following term, we first note that since the group velocity, c_g, and wave number, k, depend on the relative frequency, σ, that $g(H)$ also depends on the relative frequency σ as well as the total water depth H. Then following a similar argument in (6.34) with more terms, we expand terms and use

assumptions (6.28) - (6.31) to obtain

$$\begin{aligned}
E_{26,3} &= \int_0^T \left(\nabla_\sigma \left(g(H)\nabla_x u N - g(H_h)\nabla_x u_h \widetilde{N}_h \right), e_N \right)_\Omega dt \\
&= \int_0^T (\nabla_x u N \nabla_\sigma (g(H) - g(H_h)) + \nabla_x u (g(H) - g(H_h)) \nabla_\sigma N, e_N)_\Omega \, dt \\
&\quad + \int_0^T \left(\nabla_x (\Theta_u - e_u) \widetilde{N}_h \nabla_\sigma g(H_h) + \nabla_x (\Theta_u - e_u) g(H_h) \nabla_\sigma \widetilde{N}_h, e_N \right)_\Omega dt \\
&\quad + \int_0^T (\nabla_x u \nabla_\sigma (g(H)) \Theta_N + \nabla_x u g(H) \nabla_\sigma \Theta_N, e_N)_\Omega \, dt \\
&\leq C(K^m, K^k) \int_0^T \left(||e_\xi||_\Xi^2 + ||\Theta_\xi||_\Xi^2 \right) dt + \epsilon_1 \int_0^T ||\nabla_x e_u||_\Omega^2 dt \\
&\quad + C(K^m, K^M, K^c) \int_0^T ||\nabla_x \Theta_u||_\Xi^2 dt + C(K^m, K^c, K^k) \int_0^T ||\Theta_N||_\Omega^2 dt \\
&\quad + C(K^m, K^M, K^c, K^k) \int_0^T \left(||\nabla_\sigma \Theta_N||_\Omega^2 + ||e_N||_\Omega^2 \right) dt. \qquad (6.59)
\end{aligned}$$

Again, expanding terms, using assumptions (6.28) - (6.31) and the argument in (6.34), we find

$$\begin{aligned}
E_{26,4} &= \int_0^T \left(\nabla_\theta \left(\frac{\sigma}{\sinh(2kH)} \nabla_x h_b \sin\theta N - \frac{\sigma}{\sinh(2kH_h)} \nabla_x h_b \sin\theta \widetilde{N}_h \right), e_N \right)_\Omega dt \\
&\leq C(K^c, K^k) \int_0^T ||\Theta_N||_\Omega^2 dt + C(K^m, K^M, K^c, K^k) \int_0^T (||e_\xi||_\Xi^2 + ||\Theta_\xi||_\Xi^2) dt \\
&\quad + C(K^m, K^c, K^k) \int_0^T ||e_N||_\Omega^2 dt + C(K^M, K^c, K^k) \int_0^T ||\nabla_\theta \Theta_N||_\Omega^2 dt, \qquad (6.60)
\end{aligned}$$

and

$$\begin{aligned}
E_{26,5} &= \int_0^T \left(\nabla_\theta (\nabla_x u \cos\theta \sin\theta N - \nabla_x u_h \cos\theta \sin\theta \widetilde{N}_h), e_N \right)_\Omega dt \\
&\leq C(K^m) \int_0^T (||\Theta_N||_\Omega^2 + ||e_N||_\Omega^2) dt + \epsilon_1 \int_0^T ||\nabla_x e_u||_\Xi^2
\end{aligned}$$

$$+ C(K^m, K^M) \int_0^T (||\nabla_x \Theta_u||_\Xi^2 + ||\nabla_\theta \Theta_N||_\Omega^2) dt. \tag{6.61}$$

Like E_{12} and E_{13}, we use $\{ab\} = \{a\}\{b\} + \frac{1}{4}[a][b]$ and $[ab] = \{a\}[b] + [a]\{b\}$ to obtain

$$\begin{aligned} E_{27} + E_{28} &= -\sum_{\lambda_j \in \Gamma_\Omega} \langle [e_N(\mathbf{c}N - \mathbf{c}_h \widetilde{N}_h) \cdot \mathbf{n}], 1 \rangle_{\lambda_j} + \sum_{\lambda_j \in \Gamma_\Omega} \langle \mathbf{c}N - \widetilde{N}_h^\uparrow \{\mathbf{c}_h\} \cdot \mathbf{n}, [e_N] \rangle_{\lambda_j} \\ &= \sum_{\lambda_j \in \Gamma_\Omega} \langle (\Theta_N^\uparrow - \{\Theta_N\}) \{\mathbf{c}_h\} \cdot \mathbf{n} + \frac{1}{4} [\Theta_N][\mathbf{c}_h] \cdot \mathbf{n}, [e_N] \rangle_{\lambda_j} \\ &\quad + \sum_{\lambda_j \in \Gamma_\Omega} \langle \{\widetilde{N}_h\} [\mathbf{c_h}] \cdot \mathbf{n} + [\Theta_N] \{\mathbf{c}_h\} \cdot \mathbf{n}, \{e_N\} \rangle_{\lambda_j}. \end{aligned} \tag{6.62}$$

Writing $\{\mathbf{c}_h\} = \{\mathbf{c}_h - \mathbf{c}\} + \{\mathbf{c}\}$ and following (6.35), we find

$$\begin{aligned} &\sum_{\lambda_j \in \Gamma_\Omega} \langle (\Theta_N^\uparrow - \{\Theta_N\}) \{\mathbf{c}_h\} \cdot \mathbf{n}, [e_N] \rangle_{\lambda_j} \\ &\quad \leq C(K^m, K^M, K^t, K^c) \int_0^T \sum_{\Omega_e \subset \Omega} (h_e^{-2} ||\Theta_N||_\Omega^2 + ||\Theta_N||_{H^1(\Omega)}^2) dt \\ &\qquad + \epsilon_1 \int_0^T ||\nabla_x e_u||_\Xi^2 dt + C(K^M, K^t, K^i, K^c) \int_0^T ||\nabla_x \Theta_u||_\Xi^2 dt \\ &\qquad + C(K^m, K^M, K^t, K^i, K^c) \int_0^T ||e_N||_\Omega^2 dt, \end{aligned} \tag{6.63}$$

with a similar bound for the other term in (6.62) with $\{\mathbf{c}_h\}$. As with E_{25}, we have that

$$\begin{aligned} &\sum_{\lambda_j \in \Gamma_\Omega} \langle \frac{1}{4} [\Theta_N][\mathbf{c}_h] \cdot \mathbf{n}, [e_N] \rangle_{\lambda_j} + \sum_{\lambda_j \in \Gamma_\Omega} \langle \{\widetilde{N}_h\} [\mathbf{c_h}] \cdot \mathbf{n}, \{e_N\} \rangle_{\lambda_j} \\ &\quad = \sum_{\gamma_i \in \Gamma_\Xi} \langle \frac{1}{4} [\Theta_N][u_h - u] \cdot n_i, [e_N] \rangle_{\gamma_i \times \kappa} + \sum_{\gamma_i \in \Gamma_\Xi} \langle \{\widetilde{N}_h\} [u_h - u] \cdot n_i, \{e_N\} \rangle_{\gamma_i \times \kappa} \\ &\quad \leq \epsilon_2 \int_0^T \sum_{\gamma_i \in \Gamma_\Xi} ||\alpha^{1/2} [e_u]||_{\gamma_i}^2 dt + C(K^t) \int_0^T \sum_{\Xi_g \subset \Xi} [h_g^{-2} ||\Theta_u||_{\Xi_g}^2 + ||\Theta_u||_{H^1(\Xi_g)}^2] dt \end{aligned}$$

$$+ C(K^m, K^M, K^t, K^i, K^k) \int_0^T ||\Theta_N||^2_\Omega dt. \tag{6.64}$$

In the same way,

$$\begin{aligned} E_{29} &= \langle (\mathbf{c}_h \widetilde{N}_h - \mathbf{c}_h \widehat{N}) \cdot \mathbf{n}, e_N \rangle_{\partial\Omega_{in}} \\ &\leq C(K^m, K^M, K^t, K^c) \int_0^T \sum_{\Omega_e \subset \Omega} (h_e^{-2} ||\Theta_N||^2_\Omega + ||\Theta_N||^2_{H^1(\Omega)}) dt \\ &\quad + \epsilon_1 \int_0^T ||\nabla_x e_u||^2_\Xi dt + C(K^M, K^t, K^i, K^c) \int_0^T ||\nabla_x \Theta_u||^2_\Xi dt \\ &\quad + C(K^m, K^M, K^t, K^i, K^c) \int_0^T ||e_N||^2_\Omega dt. \end{aligned} \tag{6.65}$$

For E_{30}, we use the definition of S and apply the argument in (6.33) for both f_S and g_S to find

$$\begin{aligned} E_{30} &= \left(\frac{S_h - S}{\sigma}, e_N \right)_\Omega = (f_S(H_h)N_h - f_S(H)N + g_S(N_h)N_h - g_S(N)N, e_N)_\Omega \\ &\leq C(K^m, K^M, K^k) \int_0^T (||e_\xi||^2_\Xi + ||\Theta_\xi||^2_\Omega) dt \\ &+ C(K^m, K^M) \int_0^T (||\Theta_N||^2_\Omega + ||e_N||^2_\Omega) dt. \end{aligned} \tag{6.66}$$

Combining (6.39)-(6.66) with (6.24), choosing ϵ_i, $i = 1, 4$ sufficiently small, we obtain

$$\begin{aligned} &||e_\xi(T)||^2_\Xi + ||e_u(T)||^2_\Xi + ||e_N(T)||^2_\Omega + 2 \int_0^T ||\mu^{1/2} \nabla_x e_u||^2_\Xi dt \\ &\quad + \int_0^T \sum_{\gamma_i \in \Gamma_\Xi} \langle |\{u_h\} \cdot n_i|, [e_\xi]^2 \rangle_{\gamma_i} dt + \int_0^T \langle |u_h \cdot n_x|, e_\xi^2 \rangle_{\partial\Xi_{in}} dt \\ &\quad + \int_0^T \langle |u_h \cdot n_x|, e_\xi^2 \rangle_{\partial\Xi_{out}} dt + 2 \int_0^T \sum_{\gamma_i \in \Gamma_\Xi} ||\alpha^{1/2} [e_u]||^2_{\gamma_i} dt \end{aligned}$$

$$
\begin{aligned}
&+ 2\int_0^T ||\alpha^{1/2} e_u||^2_{\partial\Xi} dt + \int_0^T \sum_{\lambda_j \in \Gamma_\Omega} \langle |\{\mathbf{c}_h\} \cdot \mathbf{n}_j|, [e_N]^2 \rangle_{\lambda_j} dt \\
&+ \int_0^T \langle |\mathbf{c}_h \cdot \mathbf{n}|, e_N^2 \rangle_{\partial\Omega_{out}} dt + \int_0^T \langle |\mathbf{c}_h \cdot \mathbf{n}|, e_N^2 \rangle_{\partial\Omega_{in}} dt \\
&\leq C\int_0^T ||e_\xi||^2_\Xi dt + C\int_0^T ||e_u||^2_\Xi dt + C\int_0^T ||e_N||^2_\Omega dt \\
&\quad + C^*\int_0^T \sum_{\Xi_g \subset \Xi} (h_g^{-2} ||\Theta_\xi||^2_{\Xi_g} + ||\Theta_\xi||^2_{H^1(\Xi_g)}) dt \\
&\quad + C^*\int_0^T \sum_{\Xi_g \subset \Xi} (h_g^{-2} ||\Theta_u||^2_{\Xi_g} + ||\Theta_u||^2_{H^1(\Xi_g)}) dt \\
&\quad + C^*\int_0^T \sum_{\Omega_e \subset \Omega} (h_e^{-2} ||\Theta_N||^2_{\Omega_e} + ||\Theta_N||^2_{H^1(\Omega_e)}) dt \\
&\quad + C^*\int_0^T \sum_{\Xi_g \subset \Xi} h_g ||\nabla_x \Theta_u||_{\Xi_g} ||\nabla_x \Theta_u||_{H^1(\Xi_g)} dt
\end{aligned} \tag{6.67}
$$

where $C^* = C(K^m, K^M, K^t, K^i, K^c, K^k)$. Using standard approximation theory results, we find

$$
\begin{aligned}
&\int_0^T \sum_{\Xi_g \subset \Xi} (h_g^{-2} ||\Theta_\xi||^2_{\Xi_g} + ||\Theta_\xi||^2_{H^1(\Xi_g)}) dt + \int_0^T \sum_{\Xi_g \subset \Xi} (h_g^{-2} ||\Theta_u||^2_{\Xi_g} + ||\Theta_u||^2_{H^1(\Xi_g)}) dt \\
&\quad + \int_0^T \sum_{\Xi_g \subset \Xi} h_g ||\nabla_x \Theta_u||_{\Xi_g} ||\nabla_x \Theta_u||_{H^1(\Xi_g)} dt \\
&\quad \leq Ch^{2p} \int_0^T (||\xi||^2_{H^{p+1}(\Xi)} + ||u||^2_{H^{p+1}(\Xi)}) dt = C(K^r) h^{2p},
\end{aligned} \tag{6.68}
$$

and

$$
\begin{aligned}
&\int_0^T \sum_{\Omega_e \subset \Omega} (h_e^{-2} ||\Theta_N||^2_{\Omega_e} + ||\Theta_N||^2_{H^1(\Omega_e)}) dt \\
&\quad \leq Ch^{2\min\{p,q\}} \int_0^T ||N||^2_{H^{\min\{p,q\}+1}(\Omega)} dt = C(K^r) h^{2\min\{p,q\}}.
\end{aligned} \tag{6.69}
$$

We assume the initial data is sufficiently smooth so that

$$\begin{aligned}
&||\Theta_\xi(\cdot,0)||^2_{H^1(\Xi)} + ||\Theta_u(\cdot,0)||^2_{H^1(\Xi)} + ||\Theta_N(\cdot,0)||^2_{H^1(\Omega)} \\
&\quad \leq Ch^{\min\{p,q\}}(||\xi_0||^2_{H^{p+1}(\Xi)} + ||u_0||^2_{H^{p+1}(\Xi))} + ||N_0||^2_{H^{\min\{p,q\}+1}(\Omega)}) \\
&\quad \leq C(K^{r,0})h^{2\min\{p,q\}}. \qquad (6.70)
\end{aligned}$$

Now applying Gronwall's inequality to (6.67) followed by the triangle inequality we obtain the following *a priori* error estimate:

Theorem 6.4.2 *Assume, ξ, u, N, and initial data are sufficiently smooth so* (6.68) *to* (6.70) *hold. Then there exists a constant*

$$\hat{C} = C(K^m, K^M, K^t, K^i, K^c, K^k, K^r, K^{r,0}, T),$$

such that

$$\begin{aligned}
&||\xi - \xi_h||_{L^\infty(0,T;L^2(\Xi))} + ||u - u_h||_{L^\infty(0,T;L^2(\Xi))} + ||u - u_h||_{L^\infty(0,T;H^1(\Xi))} \\
&\quad + ||N - N_h||_{L^\infty(0,T;L^2(\Omega))} \leq \hat{C}h^{\min\{p,q\}}. \qquad (6.71)
\end{aligned}$$

Lastly, we show that we can remove the dependence of $\hat{C}$ on K^M. To do this we first recall another inverse inequality

$$||v(\cdot,t)||_{L^\infty(R)} \leq Kh^{-d/2}||v(\cdot,t)||_R,$$

where d is the dimension of region R. Assuming $p, q > 2$ and h sufficiently small, we have

$$||e_\xi||_{L^\infty(0,T;L^\infty(\Xi))} \leq K\hat{C}h^{p-1} \ll K^M,$$

with a similar bound for e_u and

$$||e_N||_{L^\infty(0,T;L^\infty(\Omega))} \leq K\hat{C}h^{\min(p,q)-3/2} \ll K^M,$$

and therefore we can remove the dependence of $\hat{C}$ on K^M [50]. We simplified the analysis by only considering one geographic dimension which in turn simplified the propagation velocities, $\mathbf{c}$; however, all of the previous arguments stand for the two-geographic dimension problem.

6.5 Concluding Remarks

An *a priori* error estimate was performed for the formulated DG coupled wave/circulation model. Although this DG formulation of the shallow water equations had been analyzed in [35], no coupled wave/circulation model had previously been analyzed for any numerical scheme. The convergence rate of the model was found to be the minimum of p and q, the polynomial orders of approximation for geographic and spectral space respectively. However, examining the spectral wave model separately with manufactured solutions in Section 4.1, we obtained experimentally the convergence rate of $p+1$ for $p = q$ and h small.

Chapter 7

Conclusion

The purpose of this dissertation was to use discontinuous Galerkin methods to coupled spectral wave and circulation models to model wave-current interactions. To achieve this goal, we first developed and implemented a discontinuous Galerkin (DG) spectral wave model. This numerical method allows for the use of unstructured geographic meshes and adaptive, higher-order approximations in both geographic and spectral spaces. The DG wave model is highly scalable in parallel; especially when using higher order approximations. Verification and validation of the DG spectral wave model was conducted through the method of manufactured solutions, analytic test cases, and comparing to SWAN. For the ambient current test cases and the depth induced shoaling and refraction test cases, we used linear approximations and accurately modeled the analytic solution of the significant wave height and the main wave direction. In addition, for the opposing current case, we showed that a more accurate solution is obtained by using higher-order approximations on a coarse mesh as opposed to a lower-order approximation on a refined mesh with similar numbers of degrees of freedom. We also demonstrated that employing higher order approximations in spectral space can alleviate the "Garden Sprinkler" effect. A commonly cited drawback of the DG method is

the increased number of degrees of freedom, which leads to increased computational costs. We implemented a simple p-adaptivity routine to prove that adaptivity is a viable way to dramatically increase the computational efficiency through decreasing the total number of degrees of freedom while maintaining higher-order accuracy.

Additionally, the DG spectral wave model has been coupled to the DG Shallow Water Equation Model (DG-SWEM). Both models employ the same unstructured geographic mesh, which eliminates interpolation error, and can share higher-order information. The resulting DG coupled wave/circulation model has been verified and validated through comparisons to SWAN coupled with DG-SWEM. In the near-circular shoal test case, we observed that a linear approximation in spectral space is needed to properly resolve the significant wave height, because the constant approximation was too diffusive. In general, we found that to obtain reliable results for both the wave model individually and the coupled model, linear approximations are needed in spectral space; however, if larger spectral elements are used, higher approximations may be necessary to maintain accuracy.

An *a priori* error estimate was performed for the formulated DG coupled wave/circulation model. Although this DG formulation of the shallow water equations had been analyzed in [35], no coupled wave/circulation model had previously been analyzed for any numerical scheme. The convergence rate of the model was found to be the minimum of p and q, the polynomial orders of approximation for geographic and spectral space respectively. However, ex-

amining the spectral wave model separately with manufactured solutions in Section 4.1, we obtained experimentally the optimal convergence rate of $p+1$ for $p = q$ and h small.

In future work, we will optimize the DG spectral wave model for efficiency in addition to exploring p-adaptivity in more depth and the use of other solvers to obtain further efficiency. We will expand the capabilities to the DG spectral wave model, such as allowing for spherical coordinates and tightly coupling the wave model to DG-SWEM. Future work will also involve validating the model on realistic simulations. With the combination of further optimization and improvement to the DG wave/circulation model and the continuing advancements of high performance computing, the DG wave/circulation model has the properties and potential to provide a more accurate and efficient model for wave/current interactions.

Appendix

Appendix A

Derivation of Action Balance Equation

The action balance equation can be derived from first principles through use of variational principles and Lagrangians. These derivations can be found in, for example, [66]. However, we alternatively present an abbreviated version of the derivation of the action balance equation that follows [64]. For this derivation, we take an Eulerian approach and consider the energy balance in one cell of the domain with size Δx in the x-direction, Δy in the y-direction, $\Delta\sigma$ in the σ-direction, $\Delta\theta$ in the θ-direction. The energy balance of the energy density spectrum $E = E(\sigma, \theta; x, y, t)$ for this cell can be stated as

$$\begin{aligned} \textit{change of energy in cell} = &\textit{net import of energy} \\ &+ \textit{local generation of energy.} \end{aligned} \tag{A.1}$$

The change of energy in a cell over the time interval Δt is the energy in the cell at the end of the time interval Δt minus the energy in the cell at the start of the time interval:

$$\begin{aligned} \textit{change of energy in cell} = &\left(E + \frac{\partial E}{\partial t}\Delta t\right)\Delta x\Delta y\Delta\sigma\Delta\theta \\ &- E\Delta x\Delta y\Delta\sigma\Delta\theta \\ = &\frac{\partial E}{\partial t}\Delta x\Delta y\Delta\sigma\Delta\theta\Delta t. \end{aligned} \tag{A.2}$$

The first term on the right-hand side of the energy balance (A.1) must account for the total import of energy into the cell during the time interval Δt. For the x-direction this import of energy is equal to the energy import through the left-hand side of the cell, with propagation speed c_x, minus the energy export through the right hand side of the cell (see Figure A.1):

$$\begin{aligned} \textit{net import of energy in the x-direction} =& c_x E \Delta y \Delta\sigma \Delta\theta \Delta t \\ & - \left(c_x E + \frac{\partial c_x E}{\partial x} \Delta x \right) \Delta y \Delta\sigma \Delta\theta \Delta t \\ =& - \frac{\partial c_x E}{\partial x} \Delta x \Delta y \Delta\sigma \Delta\theta \Delta t. \end{aligned} \tag{A.3}$$

Similarly, in the y-direction we have that

$$\textit{net import of energy in the y-direction} = - \frac{\partial c_y E}{\partial y} \Delta x \Delta y \Delta\sigma \Delta\theta \Delta t. \tag{A.4}$$

We also need to account for the net transport in spectral space. The directional turning of the waves is represented as energy moving from one directional cell to the next as follows. The net import of energy into a directional cell during a time interval Δt is equal to the energy import through the left-hand side of

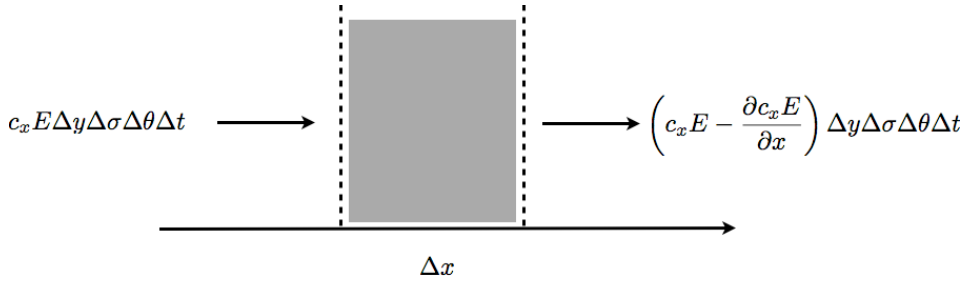

Figure A.1: Propagation of wave energy in the x-direction.

the cell minus the energy export through the right-hand side of the cell during that interval:

$$\begin{aligned} \textit{net import of energy in the } \theta\textit{-direction} =& c_\theta E \Delta x \Delta y \Delta \sigma \Delta t \\ & - \left(c_\theta E + \frac{\partial c_\theta E}{\partial \theta} \Delta \theta \right) \Delta x \Delta y \Delta \sigma \Delta t \\ =& - \frac{\partial c_\theta E}{\partial \theta} \Delta x \Delta y \Delta \sigma \Delta \theta \Delta t. \end{aligned} \tag{A.5}$$

Similarly for frequency shifting, energy is moved from one frequency cell to the next, and we have the following:

$$\textit{net import of energy in the } \sigma\textit{-direction} = - \frac{\partial c_\sigma E}{\partial \sigma} \Delta x \Delta y \Delta \sigma \Delta \theta \Delta t. \tag{A.6}$$

Lastly, we have that the locally generated energy during the time interval Δt is

$$\textit{local generation of energy} = S \Delta x \Delta y \Delta \sigma \Delta \theta \Delta t, \tag{A.7}$$

where S is the source term described in Section 2.3. By substituting (A.2)-(A.7) into (A.1) we find the energy balance for the cell $\Delta x \Delta y \Delta \sigma \Delta \theta$ over a time interval Δt to be

$$\begin{aligned} \frac{\partial E}{\partial t} \Delta x \Delta y \Delta \sigma \Delta \theta \Delta t =& - \frac{\partial c_x E}{\partial x} \Delta x \Delta y \Delta \sigma \Delta \theta \Delta t \\ & - \frac{\partial c_y E}{\partial y} \Delta x \Delta y \Delta \sigma \Delta \theta \Delta t \\ & - \frac{\partial c_\sigma E}{\partial \sigma} \Delta x \Delta y \Delta \sigma \Delta \theta \Delta t \\ & - \frac{\partial c_\theta E}{\partial \theta} \Delta x \Delta y \Delta \sigma \Delta \theta \Delta t \\ & + S \Delta x \Delta y \Delta \sigma \Delta \theta \Delta t, \end{aligned} \tag{A.8}$$

where again c_x and c_y are the propagation of wave energy through geographic space and c_σ and c_θ are the propagation speeds in spectral space. Then, by dividing all terms by $\Delta x \Delta y \Delta \sigma \Delta \theta \Delta t$ and rearranging terms, we have the Eulerian spectral energy balance

$$\frac{\partial E}{\partial t} + \frac{\partial c_x E}{\partial x} + \frac{\partial c_y E}{\partial y} + \frac{\partial c_\theta E}{\partial \theta} + \frac{\partial c_\sigma E}{\partial \sigma} = S. \tag{A.9}$$

If a current is present, as in our case, the energy density spectrum is not conserved [87]. However, action density $N = E/\sigma$ is conserved, so we instead model waves with the action balance equation which is obtained by dividing (A.9) by the relative frequency σ:

$$\frac{\partial N}{\partial t} + \frac{\partial c_x N}{\partial x} + \frac{\partial c_y N}{\partial y} + \frac{\partial c_\theta N}{\partial \theta} + \frac{\partial c_\sigma N}{\partial \sigma} = \frac{S}{\sigma}. \tag{A.10}$$

From linear wave theory, we know that wave energy propagates at the speed of the group velocity. In the presence of a current, linear wave theory is only valid for a frame of reference moving with the current. So with currents present, wave energy travels at the absolute group velocity, which is the group velocity in a fixed frame of reference and is the combination of the relative group velocity and the current

$$\mathbf{c}_{g,absolute} = \mathbf{c}_{g,relative} + \mathbf{U}.$$

(Note that throughout this dissertation $\mathbf{c}_g = \mathbf{c}_{g,relative}$.) Therefore, the propagation velocities in geographic space are

$$c_x = c_{g,x} + u,$$

$$c_y = c_{g,y} + v.$$

If a wave approaches a coast at an angle, the wave will slowly turn towards the shallower water. This is due to the depth variations along the wave crest. The phase speed

$$c = \sqrt{\frac{g}{k} \tanh kH},$$

also varies with depth and, therefore the wave crest will move faster in deeper water than it does in shallow water. The time rate of change because of this depth-induced refraction is

$$-\frac{1}{k}\frac{\partial \sigma}{\partial H}\frac{\partial H}{\partial m}$$

where m is the coordinate perpendicular to the wave direction θ. Changes in wave direction also occur due to variations in the current. This current-induced refraction is represented as

$$\frac{\mathbf{k}}{k} \cdot \frac{\partial \mathbf{U}}{\partial m}.$$

The total rate of change of the wave direction due to both depth- and current-induced refraction is then

$$c_\theta = -\frac{1}{k}\left(\frac{\partial \sigma}{\partial H}\frac{\partial H}{\partial m} + \frac{1}{k} \cdot \frac{\partial \mathbf{U}}{\partial m}\right).$$

The frequency of a wave in a fixed frame of reference ω is related to the frequency by

$$\omega = \sigma + \mathbf{k} \cdot \mathbf{U},$$

where $\mathbf{k} \cdot \mathbf{U}$ can be seen as the Doppler shift. In the frame of reference moving with the energy or action of the wave, the relative frequency shifts due to variations in the depth and current. This time rate of change of the relative frequency is

$$c_\sigma = \frac{\partial \sigma}{\partial H} \left(\frac{\partial H}{\partial t} + \mathbf{U} \cdot \nabla_{\mathbf{x}} H \right) - c_g \mathbf{k} \cdot \frac{\partial \mathbf{U}}{\partial s},$$

where s is the coordinate normal to the wave direction θ. The first term in the parenthesis represents the effect of the variation of depth in time and the second term in the parenthesis represents the effect of the current moving the wave over a horizontally varying depth. The second term in the expression represents the wave moving with a horizontally varying current. Again, more in-depth and detailed information on this derivation can be found in [64].

Bibliography

[1] V. Aizinger. *A discontinuous Galerkin method for two-and three-dimensional shallow-water equations.* PhD thesis, The University of Texas at Austin, 2005.

[2] V. Aizinger and C. Dawson. A discontinuous Galerkin method for two-dimensional flow and transport in shallow water. *Adv. in Water Resour.*, 25(1):67–84, 2002.

[3] Aquaveo. Surface water modeling system. `http://www.aquaveo.com/sms`.

[4] D.N. Arnold. An interior penalty finite element method with discontinuous elements. *SIAM J. on Numer. Anal.*, pages 742–760, 1982.

[5] D.N. Arnold, F. Brezzi, B. Cockburn, and L.D. Marini. Unified analysis of discontinuous Galerkin methods for elliptic problems. *SIAM J. on Numer. Anal.*, pages 1749–1779, 2002.

[6] J.P. Aubin. Approximation des problemes aux limites non homogenes pour des opérateurs non linéaires. *J. of Math. Anal. and Appl.*, 30(3):510–521, 1970.

[7] I. Babuska. The finite element method with penalty. *Math. Comp.*, 27(122):221–228, 1973.

[8] I. Babuska and M. Zlamal. Nonconforming elements in the finite element method with penalty. *SIAM J. on Numer. Anal.*, pages 863–875, 1973.

[9] J.A. Battjes and J. Janssen. Energy loss and set-up due to breaking of random waves. In *Proc. 16th Int. Conf. Coastal Eng.*, volume 1, pages 649–660, 1978.

[10] N. Booij and L.H. Holthuijsen. Propagation of ocean waves in discrete spectral wave models. *J. of Comput. Phys.*, 68(2):307–326, 1987.

[11] N. Booij, R.C. Ris, and L.H. Holthuijsen. A third-generation wave model for coastal regions. I- Model description and validation. *J. of Geophys. Res.*, 104(C4):7649–7666, 1999.

[12] E. Bouws and G.J. Komen. On the balance between growth and dissipation in an extreme depth-limited wind-sea in the southern North Sea. *J. of Phys. Oceanog.*, 13(9):1653–1658, 1983.

[13] S.C. Brenner and R. Scott. *The mathematical theory of finite element methods*, volume 15 of *Texts in Applied Mathematics*. Springer, 2007.

[14] S. Bunya, J.C. Dietrich, J.J. Westerink, B.A. Ebersole, J.M. Smith, J.H. Atkinson, R. Jensen, D.T. Resio, R.A. Luettich, C. Dawson, et al. A high-resolution coupled riverine flow, tide, wind, wind wave, and storm surge model for southern Louisiana and Mississippi. Part I: Model development and validation. *Mon. Weather Rev.*, 138(2):345–377, 2010.

[15] S. Bunya, E.J. Kubatko, J.J. Westerink, and C. Dawson. A wetting and drying treatment for the Runge-Kutta discontinuous Galerkin solution to the shallow water equations. *Comput. Methods in Appl. Mech. and Eng.*, 198(17-20):1548–1562, 2009.

[16] D.E. Cartwright and P. Melchior. *Tides: A scientific history.* Cambridge Univ Press, 1999.

[17] P. Castillo, B. Cockburn, D. Schotzau, and C. Schwab. Optimal a priori error estimates for the hp-version of the local discontinuous Galerkin method for convection-diffusion problems. *Math. of Comput.*, 71(238):455–478, 2002.

[18] L. Cavaleri and P.M. Rizzoli. Wind wave prediction in shallow water: Theory and applications. *J. of Geophys. Res.*, 86(C11):10961–10, 1981.

[19] J.G. Charney, R. Fjörtoft, and J.V. Neumann. Numerical integration of the barotropic vorticity equation. *Tellus*, 2(4):237–254, 1950.

[20] Q. Chen, L. Wang, and R. Tawes. Hydrodynamic response of northeastern Gulf of Mexico to hurricanes. *Estuaries and Coasts*, 31(6):1098–1116, 2008.

[21] B. Cockburn and C. Dawson. Some extensions of the local discontinuous Galerkin method for convection-diffusion equations in multidimensions. *ICES Report 99-27*, 1999.

[22] B. Cockburn, S. Hou, and C.W. Shu. The Runge-Kutta local projection discontinuous Galerkin finite element method for conservation laws. IV: The multidimensional case. *Math. of Comput.*, 54(190):545–581, 1990.

[23] B. Cockburn, G.E. Karniadakis, and C.W. Shu. The development of discontinuous Galerkin methods. In B. Cockburn, G.E. Karniadakis, and C.W. Shu, editors, *Discontinuous Galerkin Methods*, volume 11 of *Lecture Notes in Computational Science and Engineering*, pages 3–50. Springer Berlin Heidelberg, 2000.

[24] B. Cockburn, S.Y. Lin, and C.W. Shu. TVB Runge-Kutta local projection discontinuous Galerkin finite element method for conservation laws III: One-dimensional systems. *J. of Comput. Physics*, 84(1):90–113, 1989.

[25] B. Cockburn and C.W. Shu. TVB Runge-Kutta local projection discontinuous Galerkin finite element method for conservation laws II: General framework. *Math. of Comput.*, 52(186):411–435, 1989.

[26] B. Cockburn and C.W. Shu. The Runge-Kutta local projection P1-discontinuous Galerkin finite element method for scalar conservation laws. *RAIRO Modél. Math. Anal. Numér*, 25(3):337–361, 1991.

[27] B. Cockburn and C.W. Shu. The local discontinuous Galerkin method for time-dependent convection-diffusion systems. *SIAM J. on Numer. Anal.*, pages 2440–2463, 1998.

[28] B. Cockburn and C.W. Shu. The Runge–Kutta discontinuous Galerkin method for conservation laws V: Multidimensional systems. *J. of Comput. Phys.*, 141(2):199–224, 1998.

[29] N. Collins, G. Theurich, C. Deluca, M. Suarez, A. Trayanov, V. Balaji, P. Li, W. Yang, C. Hill, and A. Da Silva. Design and implementation of components in the earth system modeling framework. *Int. J. of High Perform. Comput. Appl.*, 19(3):341–350, 2005.

[30] R.A. Dalrymple and C.J. Lozano. Wave-current interaction models for rip currents. *J. of Geophys. Res.*, 83(C12):6063, 1978.

[31] C. Dawson. Conservative, shock-capturing transport methods with nonconservative velocity approximations. *Comput. Geosci.*, 3(3):205–227, 1999.

[32] C. Dawson, E.J. Kubatko, J.J. Westerink, C. Trahan, C. Mirabito, C. Michoski, and N. Panda. Discontinuous Galerkin methods for modeling hurricane storm surge. *Adv. in Water Resour.*, 34(9):1165–1176, 2011.

[33] C. Dawson and J. Proft. Discontinuous and coupled continuous/discontinuous Galerkin methods for the shallow water equations. *Comput. Methods in Appl. Mech. and Eng.*, 191(41):4721–4746, 2002.

[34] C. Dawson and J. Proft. Discontinuous/continuous Galerkin methods for coupling the primitive and wave continuity equations of shallow wa-

ter. *Comput. Methods in Appl. Mech. and Eng.*, 192(47):5123–5145, 2003.

[35] C. Dawson and J. Proft. Coupled discontinuous and continuous Galerkin finite element methods for the depth-integrated shallow water equations. *Comput. Methods in Appl. Mech. and Eng.*, 193(3):289–318, 2004.

[36] C. Dawson, S. Sun, and M.F. Wheeler. Compatible algorithms for coupled flow and transport. *Comput. Methods in Appl. Mech. and Eng.*, 193(23):2565–2580, 2004.

[37] J.C. Dietrich, S. Bunya, J.J. Westerink, B.A. Ebersole, J.M. Smith, J.H. Atkinson, R. Jensen, D.T. Resio, R.A. Luettich, C. Dawson, et al. A high-resolution coupled riverine flow, tide, wind, wind wave, and storm surge model for southern Louisiana and Mississippi. Part II: Synoptic description and analysis of hurricanes Katrina and Rita. *Mon. Weather Rev.*, 138(2):378–404, 2010.

[38] J.C. Dietrich, S. Tanaka, J.J. Westerink, C.N. Dawson, Jr. Luettich, R.A., M. Zijlema, L.H. Holthuijsen, J.M. Smith, L.G. Westerink, and H.J. Westerink. Performance of the unstructured-mesh, SWAN+ADCIRC model in computing hurricane waves and surge. *J. of Sci. Comput.*, 52:468–497, 2012.

[39] J.C. Dietrich, C.J. Trahan, M.T. Howard, J.G. Fleming, R.J. Weaver, S. Tanaka, L. Yu, R.A. Luettich Jr., C.N. Dawson, J.J. Westerink,

G. Wells, A. Lu, K. Vega, A. Kubach, K.M. Dresback, R.L. Kolar, C. Kaiser, and R.R. Twilley. Surface trajectories of oil transport along the northern coastline of the Gulf of Mexico. *Cont. Shelf Res.*, 41(0):17 – 47, 2012.

[40] J.C. Dietrich, M. Zijlema, P.-E. Allier, L.H. Holthuijsen, N. Booij, J.D. Meixner, J.K. Proft, C. Dawson, C.J. Bender, A. Naimaster, J.M. Smith, and J.J. Westerink. Limiters for spectral propagation velocities in SWAN. *Ocean Model.*, (0), 2012.

[41] J.C. Dietrich, M. Zijlema, J.J. Westerink, L.H. Holthuijsen, C. Dawson, R.A. Luettich Jr, R.E. Jensen, J.M. Smith, G.S. Stelling, and G.W. Stone. Modeling hurricane waves and storm surge using integrally-coupled, scalable computations. *Coast. Eng.*, 58(1):45–65, 2011.

[42] L.F. Dolata and W. Rosenthal. Wave setup and wave-induced currents in coastal zones. *J. of Geophys. Res.*, 89(C2):1973–1982, 1984.

[43] J. Douglas and T. Dupont. Interior penalty procedures for elliptic and parabolic Galerkin methods. *Comput. Methods in Appl. Sci.*, pages 207–216, 1976.

[44] M. Dubiner. Spectral methods on triangles and other domains. *J. of Sci. Comput.*, 6(4):345–390, 1991.

[45] D.A. Dunavant. High degree efficient symmetrical Gaussian quadrature

rules for the triangle. *Int. J. for Numer. Methods in Eng.*, 21(6):1129–1148, 1985.

[46] Y. Eldeberky. *Nonlinear transformation of wave spectra in the nearshore zone*. PhD thesis, Delft University of Technology, Department of Civil Engineering, The Netherlands, 1996.

[47] Y. Eldeberky and J.A. Battjes. Parameterization of triad interactions in wave energy models. *Proc. Coast. Dyn. Conf.*, pages 140–148, 1995.

[48] Y. Eldeberky and J.A. Battjes. Spectral modeling of wave breaking: Application to Boussinesq equations. *J. Geophys. Res*, 101(C1):1253–1264, 1996.

[49] L. Euler. Principes généraux du mouvement des fluides. *Mém. Acad. Sci. Berlin*, 11:274–315, 1757.

[50] R.E. Ewing and M.F. Wheeler. Galerkin methods for miscible displacement problems in porous media. *SIAM J. on Numer. Anal.*, 17(3):351–365, 1980.

[51] S. Fagherazzi, P. Rasetarinera, M.Y. Hussaini, and D.J. Furbish. Numerical solution of the dam-break problem with a discontinuous Galerkin method. *J. of Hydraul. Eng.*, 130:532–539, 2004.

[52] Y. Funakoshi, S.C. Hagen, and P. Bacopoulos. Coupling of hydrodynamic and wave models: Case study for hurricane Floyd (1999) hindcast. *ASCE J. of Waterway, Port, Coast., and Ocean Eng.*, 134:321–335, 2008.

[53] R. Gelci, H. Cazalé, and J. Vassal. Prévision de la houle.La méthode des densités spectroangulaires. *Bulletin d'information du Comité d'Océanographie et d'Etude des Côtes*, 9:416–435, 1957.

[54] J.B. Gregersen, P.J.A. Gijsbers, S.J.P. Westen, M. Blind, et al. OpenMI: The essential concepts and their implications for legacy software. *Adv. in Geosci.*, 4:37–44, 2005.

[55] H. Günther, S. Hasselmann, and P.A.E.M. Janssen. The WAM model cycle 4 (revised version). Technical report, Deutsch. Klim. Rechenzentrum, Techn. Rep. No. 4, Hamburg, Germany, 1992.

[56] W. Hansen. Theorie zur errechnung des wasserstandes und der strömungen in randmeeren nebst anwendungen. *Tellus*, 8:187–300, 1956.

[57] K. Hasselmann. Grundgleichungen der seegangsvorhersage. *Schiffstechnik*, 7:l91–195, 1960.

[58] K. Hasselmann. On the non-linear energy transfer in a gravity-wave spectrum. *J. of Fluid Mech.*, 12(481-500):15, 1962.

[59] K. Hasselmann. On the spectral dissipation of ocean waves due to white capping. *Bound.-Layer Meteorol.*, 6(1):107–127, 1974.

[60] K. Hasselmann, T.P. Barnett, E. Bouws, H. Carlson, D.E. Cartwright, K. Enke, J.A. Ewing, H. Gienapp, D.E. Hasselmann, P. Kruseman, et al. Measurements of wind-wave growth and swell decay during the Joint

North Sea Wave project (JONSWAP). *Ergnzungsheft zur Deutschen Hydrographischen Zeitschrift Reihe*, 8(12), 1973.

[61] S. Hasselmann, K. Hasselmann, J.H. Allender, and T.P. Barnett. Computations and parameterizations of the nonlinear energy transfer in a gravity-wave specturm. Part II: Parameterizations of the nonlinear energy transfer for application in wave models. *J. of Phys. Oceanog.*, 15(11):1378–1391, 1985.

[62] T.S. Hedges. Combinations of waves and currents: An introduction. In *Proc. Inst. Civ. Eng.*, volume 82, pages 567–585, 1987.

[63] C. Hill, C. DeLuca, M. Suarez, A. Da Silva, et al. The architecture of the earth system modeling framework. *Comput. in Sci. & Eng.*, 6(1):18–28, 2004.

[64] L.H. Holthuijsen. *Waves in Oceanic and Coastal Waters*. Cambridge Univ. Pr., 2007.

[65] T.W. Hsu, S.H. Ou, and J.M. Liau. Hindcasting nearshore wind waves using a FEM code for SWAN. *Coast. Eng.*, 52(2):177–195, 2005.

[66] P. Janssen. The wave model. `http://www.ecmwf.int/newsevents/training/rcourse_notes/pdf_files/Wave_model.pdf`, May 1995.

[67] P.A.E.M. Janssen. Quasi-linear theory of wind-wave generation applied to wave forecasting. *J. of Phys. Oceanog.*, 21(11):1631–1642, 1991.

[68] P.A.E.M. Janssen. Progress in ocean wave forecasting. *J. of Comput. Phys.*, 227(7):3572–3594, 2008.

[69] I.G. Jonsson. Wave current interactions. *The Sea, Ocean Eng. Sci. Ser.*, 9(A):65–70, 1993.

[70] L.C. Wellford Jr. and J.T. Oden. Discontinuous finite-element approximations for the analysis of shock waves in nonlinearly elastic materials. *J. of Comput. Phys.*, 19(2):179 – 210, 1975.

[71] S.Y. Kim, Yasuda T., and Mase H. Numerical analysis of effects of tidal variations on storm surges and waves. *Appl. Ocean Res.*, 30(4):311 – 322, 2008.

[72] I.P.E. Kinnmark and W.G. Gray. An implicit wave equation model for the shallow water equations. *Adv. in Water Resour.*, 7(4):168–171, 1984.

[73] R.L. Kolar and J.J. Westerink. A look back at 20 years of GWC-based shallow water models. In *Proceedings of the XIII International Conference on Computational Methods in Water Resources, Calgary, Alberta, Canada*, pages 899–906, 2000.

[74] G.J. Komen, S. Hasselmann, and K. Hasselmann. On the existence of a fully developed wind-sea spectrum. *J. of Phys. Oceanog.*, 14(8):1271–1285, 1984.

[75] E.J. Kubatko. *Development, implementation, and verification of hp discontinuous Galerkin models for shallow water hydrodynamics and transport*. PhD thesis, University of Notre Dame, 2005.

[76] E.J. Kubatko, S. Bunya, C. Dawson, and J.J. Westerink. Dynamic p-adaptive Runge-Kutta discontinuous Galerkin methods for the shallow water equations. *Comput. Methods in Appl. Mech. and Eng.*, 198(21-26):1766–1774, 2009.

[77] E.J. Kubatko, S. Bunya, C. Dawson, J.J. Westerink, and C. Mirabito. A performance comparison of continuous and discontinuous finite element shallow water models. *J. of Sci. Comput.*, 40(1):315–339, 2009.

[78] E.J. Kubatko, J.J. Westerink, and C. Dawson. *hp* discontinuous Galerkin methods for advection dominated problems in shallow water flow. *Comput. Methods in Appl. Mech. and Eng.*, 196(1):437–451, 2006.

[79] G.Ph. Van Vledder Kuik, A.J. and L.H. Holthuijsen. A method for the routine analysis of pitch-and-roll buoy wave data. *J. of Phys. Oceanog.*, 18(7):1020–1034, 1988.

[80] P.S. Laplace. Recherches sur plusieurs points du système du monde. *Mem. Acad. R. Sci. Paris*, 88:75–182, 1775.

[81] P. Lasaint and P.A. Raviart. *Mathematical Aspects Finite Elments in Partial Differential Equations*, chapter On a Finite Element Method for Solving the Neutron Transport Equation. Academic Press, 1974.

[82] J.J. Leendertse. *Aspects of a computational model for long-period water-wave propagation.* Memorandum RM-5294-PR, The Rand Corp., Santa Monica, California, May 1967, 1967.

[83] H. Li and R.X. Liu. The discontinuous Galerkin finite element method for the 2D shallow water equations. *Math. and Comput. in Simul.*, 56(3):223–233, 2001.

[84] J.-L. Lions. Problemes aux limites non homogenes a donees irregulieres: Une methode d'approximation. *Numer. Anal. of Partial Differ. Equ. (C.I.M.E. 2 Ciclo,Ispra,1967)*, pages 183–292, 1968.

[85] M.S. Longuet-Higgins and R.W. Stewart. Changes in the form of short gravity waves on long waves and tidal currents. *J. of Fluid Mech.*, 8(04):565–583, 1960.

[86] M.S. Longuet-Higgins and R.W. Stewart. The changes in amplitude of short gravity waves on steady non-uniform currents. *J. of Fluid Mech.*, 10(4):529–549, 1961.

[87] M.S. Longuet-Higgins and R.W. Stewart. Radiation stress and mass transport in gravity waves, with application to surf beats. *J. of Fluid Mech.*, 13(04):481–504, 1962.

[88] M.S. Longuet-Higgins and R.W. Stewart. Radiation stresses in water waves; a physical discussion, with applications. *Deep Sea Res. and Ocean. Abst.*, 11(4):529 – 562, 1964.

[89] R.A. Luettich Jr., J.J. Westerink, and N.W. Scheffner. ADCIRC: An advanced three-dimensional circulation model for shelves, coasts, and estuaries. Report 1. Theory and methodology of ADCIRC-2DDI and ADCIRC-3DL. Technical report, DTIC Document, 1992.

[90] D.R. Lynch and W.G. Gray. A wave equation model for finite element tidal computations. *Comput. & fluids*, 7(3):207–228, 1979.

[91] P.A. Madsen and O.R. Sørensen. Bound waves and triad interactions in shallow water. *Ocean Eng.*, 20(4):359–388, 1993.

[92] J.C. McWilliams and J.M. Restrepo. The wave-driven ocean circulation. *J. of Phys. Oceanog.*, 29(10):2523–2540, 1999.

[93] J.C. McWilliams, J.M. Restrepo, and E.M. Lane. An asymptotic theory for the interaction of waves and currents in coastal waters. *J. of Fluid Mech.*, 511:135–178, 2004.

[94] C.C. Mei. *The applied of ocean surface waves.* John Wiely & Sons, New York, 1989.

[95] J.W. Miles. On the generation of surface waves by shear flows. *J. of Fluid Mech.*, 3(02):185–204, 1957.

[96] C. Mirabito. *Analysis, Implementation, and Verification of a Discontinuous Galerkin Method for Prediction of Storm Surges and Coastal Deformation.* PhD thesis, The University of Texas at Austin, 2011.

[97] C. Mirabito, C. Dawson, and V. Aizinger. An *a priori* error estimate for the local discontinuous Galerkin method applied to two-dimensional shallow water and morphodynamic flow. *Math. of Comput.*, submitted.

[98] H. Mitsuyasu. On the growth of the spectrum of wind-generated waves. 1. *Rep. Res. Inst. Appl. Mech., Kyushu University*, 16:459–465, 1968.

[99] H. Mitsuyasu. On the growth of the spectrum of wind-generated waves. 2. *Rep. Res. Inst. Appl. Mech., Kyushu University*, 17:235–243, 1969.

[100] R.V. Moore and C.I. Tindall. An overview of the open modelling interface and environment (the OpenMI). *Environ. Sci. & Policy*, 8(3):279–286, 2005.

[101] C.L. Navier. Mémoire sur les lois du mouvement des fluides. *Mémoires de lAcadémie Royale des Sciences de lInstitut de France*, 6:389–440, 1823.

[102] I.M. Navon. FEUDX: A two-stage, high-accuracy, finite-element FORTRAN program for solving shallow-water equations. *Comput. & Geosci.*, 13(3):255–285, 1987.

[103] J. Nitsche. Über ein variationsprinzip zur lösung von dirichlet-problemen bei verwendung von teilräumen, die keinen randbedingungen unterworfen sind. In *Abhandlungen aus dem Mathematischen Seminar der Universität Hamburg*, volume 36, pages 9–15. Springer, 1971.

[104] J.T. Oden, I. Babuŝka, and C.E. Baumann. A discontinuous hp finite element method for diffusion problems. *J. of Comput. Phys.*, 146(2):491–519, 1998.

[105] W.W. Pandoe and B.L. Edge. Cohesive sediment transport in the 3D-hydrodynamic-baroclinic circulation model: Study case for idealized tidal inlet. *Ocean Eng.*, 31(17-18):2227–2252, 2004.

[106] P.W. Partridge and C.A. Brebbia. Quadratic finite elements in shallow water problems. *J. of the Hydraul. Div.*, 102(9):1299–1313, 1976.

[107] O.M. Phillips. On the generation of waves by turbulent wind. *J. of Fluid Mech.*, 2(5):417–445, 1957.

[108] O.M. Phillips. The dynamics of the upper ocean, 1977.

[109] W.J. Pierson Jr. and L. Moskowitz. A proposed spectral form for fully developed wind seas based on the similarity theory of SA Kitaigorodskii. *J. of Geophys. Res.*, 69(24):5181–5190, 1964.

[110] G.W. Platzman. The lattice structure of the finite-difference primitive and vorticity equations. *Mon. Weather Rev.*, 86(8):285–292, 1958.

[111] J. Qi, C. Chen, R.C. Beardsley, W. Perrie, G.W. Cowles, and Z. Lai. An unstructured-grid finite-volume surface wave model (FVCOM-SWAVE): Implementation, validations and applications. *Ocean Model.*, 28(1-3):153–166, 2009.

[112] W.H. Reed and T.R. Hill. Triangular mesh methods for the neutron transport equation. *Los Alamos Report LA-UR-73-479*, 1973.

[113] O. Reynolds. An experimental investigation of the circumstances which determine whether the motion of water shall be direct or sinuous, and of the law of resistance in parallel channels. *Proc. of the R. Soc. of Lond.*, 35(224-226):84–99, 1883.

[114] R. Ris, L.H. Holthuijsen, J.M. Smith, N. Booij, and A. van Dongeren. The ONR test bed for coastal and oceanic wave models. In J.M. Smith, editor, *Proc. 28th Int. Conf. Coast. Eng.*, pages 380–392. ASCE, World Scientific Publishing, 2003.

[115] B. Rivière, M.F. Wheeler, and V. Girault. Improved energy estimates for interior penalty, constrained and discontinuous Galerkin methods for elliptic problems. Part I. *Comput. Geosci.*, 3(3):337–360, 1999.

[116] W.E. Rogers, J.M. Kaihatu, L. Hsu, R.E. Jensen, J.D. Dykes, and K.T. Holland. Forecasting and hindcasting waves with the SWAN model in the Southern California Bight. *Coast. Eng.*, 54(1):1–15, 2007.

[117] A. Roland, U. Zanke, T.W. Hsu, S.H. Ou, J.M. Liau, and S.K. Wang. Verification of a 3rd generation FEM spectral wave model for shallow and deep water applications. *ASME Conf. Proc.*, 2006(47470):487–499, 2006.

[118] D. Schwanenberg, R. Kiem, and J. Kongeter. *Discontinuous Galerkin Methods*, chapter Discontinuous Galerkin method for the shallow water equations, pages 289–309. Springer, Heidelber, 200.

[119] R.L. Snyder and J. Elliott. Array measurements of atmospheric pressure fluctuations above surface gravity waves. *J. of Fluid Mech.*, 102:1–59, 1981.

[120] O.R. Sørensen, H. Kofoed-Hansen, M. Rugbjerg, and L.S. Sørensen. A third-generation spectral wave model using an unstructured finite volume technique. In *Coastal Engineering Conference*, volume 29, page 894. American Society of Civil Engineers, 2004.

[121] G.S. Stelling and J.J Leendertse. Approximation of convective processes by cyclic AOI methods. In *Estuarine and Coastal Modeling*, pages 771–782. ASCE, 1992.

[122] J. Steppeler. FE2DY: A finite element FORTRAN program for the solution of the shallow-water equations with energy conservation. *Comput. & Geosci.*, 16(5):645–667, 1990.

[123] G.G. Stokes. On the theories of the internal friction of fluids in motion, and of the equilibrium and motion of elastic solids. *Trans. Cambridge Philos. Soc.*, 8:287–320, 1849.

[124] SWAMP Group and Sea Wave Modeling Project. *Ocean wave modeling*. Plenum Pub Corp, 1985.

[125] C. Taylor and P. Hood. A numerical solution of the Navier-Stokes equations using the finite element technique. *Comput. & Fluids*, 1(1):73–100, 1973.

[126] The SWAN team. *SWAN Cycle III version 40.85*. Delft University of Technology, 2011.

[127] H.L. Tolman. A third-generation model for wind waves on slowly varying, unsteady, and inhomogeneous depths and currents. *J. of Phys. Oceanog.*, 21(6):782–797, 1991.

[128] H.L. Tolman. Effects of numerics on the physics in a third-generation wind-wave model. *J. of Phys. Oceanog.*, 22:1095–1095, 1992.

[129] H.L. Tolman. Alleviating the Garden Sprinkler Effect in wind wave models. *Ocean Model.*, 4(3):269–289, 2002.

[130] H.L. Tolman, B. Balasubramaniyan, L.D Burroughs, D.V. Chalikov, Y.Y Chao, H.S. Chen, and V.M. Gerald. Development and implementation of wind-generated ocean surface wave models at NCEP. *Weather and Forecast.*, 17(2):311–333, 2002.

[131] C.B. Vreugdenhil. *Numerical methods for shallow-water flow*, volume 13. Springer, 1994.

[132] WAMDI Group, S. Hasselmann, K. Hasselmann, E. Bauer, P. Janssen, G.J. Komen, L. Bertotti, P. Lionello, A. Guillaume, V.C. Cardone, J.A.

Greenwood, et al. The WAM Model-a third generation ocean wave prediction model. *J. of Phys. Oceanog.*, 18:1775–1810, 1988.

[133] J.D. Wang and J.J. Connor. Mathematical modeling of near coastal circulation. Technical Report Report No MITSG 75-13, Massachusetts Institute of Technology, Cambridge, MA, April 1975.

[134] J.C. Warner, N. Perlin, and E.D. Skyllingstad. Using the Model Coupling Toolkit to couple earth system models. *Environ. Model. & Softw.*, 23(10):1240–1249, 2008.

[135] R.J. Weaver and D.N. Slinn. Effect of wave forcing on storm surge. In *Proceedings of Coastal Engineering '04*, pages 1532–1538, Lisbon, Portugal, 2004.

[136] J.J. Westerink, R.A. Luettich, J.C. Feyen, J.H. Atkinson, C. Dawson, H.J. Roberts, M.D. Powell, J.P. Dunion, E.J. Kubatko, and H. Pourtaheri. A basin- to channel-scale unstructured grid hurricane storm surge model applied to southern Louisiana. *Mon. Weather Rev.*, 136(3):833–864, 2008.

[137] M.F. Wheeler. An elliptic collocation-finite element method with interior penalties. *SIAM J. on Numer. Anal.*, pages 152–161, 1978.

[138] J. Wu et al. Wind-stress coefficients over sea surface from breeze to hurricane. *J. of Geophys. Res.*, 87(C12):9704–9706, 1982.

[139] B. Yildirim and G.E. Karniadakis. A hybrid spectral/DG method for solving the phase-averaged ocean wave equation: Algorithm and validation. *J. of Comput. Phys.*, 2012.

[140] M. Zijlema. Computation of wind-wave spectra in coastal waters with SWAN on unstructured grids. *Coast. Eng.*, 57(3):267–277, 2010.